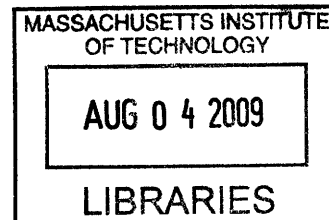# THERMODYNAMIC PROPERTIES OF METAL HYDRIDE NANOSTRUCTURES

by

Vincent Bérubé

Submitted to the Department of Physics
in partial fulfillment of the requirements for the degree of
Doctor of Philosophy
at the
MASSACHUSETTS INSTITUTE OF TECHNOLOGY
September 2008 [FEBRUARY 2009]

ARCHIVES

Author:

Vincent Bérubé
Department of Physics
September 25, 2008

Certified by

Mildred S. Dresselhaus
Institute Professor
Thesis Supervisor

Certified by

Gang Chen
Professor of Mechanical Engineering
Thesis Co-Supervisor

Accepted by

Thomas J. Greytak
Associate Department Head for Education

MASSACHUSETTS INSTITUTE OF TECHNOLOGY

This thesis was presented

by

Vincent Bérubé

It was defended on

September 25th 2008

and approved by

Millie S Dresselhaus, Institute Professor, MIT Department of Physics and Electrical

Engineering

Gang Chen, Professor, MIT Department of Mechanical Engineering

J David Litster, Professor, MIT Department of Physics

Marin Soljacic, Assistant Professor, MIT Department of Physics

THERMODYNAMIC PROPERTIES OF METAL HYDRIDE NANOSTRUCTURES

Vincent Bérubé, PhD
Massachusetts Institute of Technology, 2008

ABSTRACT

Hydrogen is considered a good energy carrier candidate for future automotive applications because of its high abundance and its potential role in a carbon-free cycle. The high gravimetric and volumetric storage capacities of metal hydrides make them ideal hydrogen carriers if the limitations associated with their slow hydrogen release kinetics, their high hydrogen release temperatures, and their poor thermal properties can be resolved. In this thesis, the thermodynamic and kinetic improvements on the hydrogen release properties of nanostructured metal hydrides are investigated both theoretically and experimentally. Four main results are presented in this work. The excess volume present in deformed regions is identified as the key factor in explaining the reduction in the enthalpy of formation observed experimentally in nanostructured materials. The impact of excess volume on the enthalpy of formation at 0K is quantified using three equations of state, and it is found to be as important as the combined impact of surfaces, grain boundaries and the presence of metastable crystalline phases. Then, the findings on the properties of excess volume are generalized to high temperatures. It is demonstrated that the impact of temperature will be more favorable to a reduction of the enthalpy of formation if a large fraction of the metal hydride is in a state of small excess volume compared to a small fraction of the hydride in a state of high excess volume. The impact of a temperature increase on the enthalpy of formation of metal hydrides is found to offset the effect of the excess volume as calculated at 0K. The stability of the regions containing excess volume over multiple hydriding/dehydriding cycles is also calculated. At high temperatures and large excess volumes, the free energy barrier created by the excess entropy reduces the recrystallization rate of the deformed regions by several orders of magnitude. A regime where the benefits of the excess volume on the enthalpy of formation can be maintained is thus identified. Finally, an experiment to study the cycling properties of metal hydrides was designed using Raman spectroscopy. It is demonstrated that the release temperature of hydrogen could be accurately measured using Raman spectroscopy.

TABLE OF CONTENTS

8

LIST OF TABLES

LIST OF FIGURES

15

ACKNOWLEDGEMENT

First and foremost I would like to acknowledge the Massachusetts Institute of Technology and the professors, students and staff that make it the great institution that it is. I came to MIT five years ago with a love for science and a desire to develop myself as a physicist and push my personal limits. Through the ups and downs, successes and failures, and the friendship and mentorship experiences characteristic of a grad student life, I reached those objectives, but more importantly; I redefined or strengthened my values and ideals, I discovered new passions, and I clarified my goals in life.

My journey at MIT was a fascinating one aimed at a young mind's ideal. A journey punctuated with changes in destination and marked by eye opening experiences. There are no clear paths that one has to take to succeed at MIT, and there are no clear indications as to whether or not you lived up to the opportunity that was given to you. For this reason, MIT can be a difficult place and many good people get lost along the way. But it is what one learns through his or her journey at MIT much more than reaching the final destination that is the true gift that one receives from MIT. In many ways, MIT takes you apart and builds you into someone stronger and more capable, even if curiously, it often seems to make you very good at something different then what you intended upon your arrival.

Even if I am departing MIT with a feeling that I am leaving behind what has defined me for many years, I truly want to thank the Institute for opening doors that I did not know about or that I never thought I could open. I also want to thank MIT and its people for making me a better professional as well as a more effective, capable, and driven individual.

The most influential people who helped me successfully navigate through my PhD have been my advisers: Prof. Gang Chen and Prof. Millie Dresselhaus. They both presented me with amazing opportunities and entrusted me with responsibilities that allowed me to develop myself as a scientist, as a leader, and as a team player. Despite their demanding schedule, Gang and Millie have been the most available people that I have had a chance to meet at MIT. They both exemplify work ethics, passion for their work, and dedication to their students, and I will always be grateful for their teaching and for making the second half of my MIT life extremely enjoyable and satisfying.

The numerous lab mates and colleagues that I met at MIT have also been a great source of inspiration and motivation both in my academic and personal life. It is the capacity to attract brilliant and creative minds around projects of considerable impact that makes MIT such a stimulating environment. Many of my lab mates have become some of the best friends that I ever had and they helped make my time at MIT so enjoyable. For all the inspiring conversations, for being role models in your own ways, for the good times and your support through harsher times, thank you: Aaron, Andy, Anurag, Arvind, Ase, Carlos G., Carlos P., Chris, Cliff, Dr. X,

19

DEDICATION

To my wife Emilie, my parents, and my brother.

NOMENCLATURE

A =activity coefficient (atm)

a =scaling parameter (dimentionless)

b =radius of the van der Waals bridge (m)

$\bar{b}$ =Burgers vector

B =bulk modulus (Pa)

Bi =Biot number ($=hL/k$), dimensionless

B_o =bulk modulus at the reference state (Pa)

B' =bulk modulus first pressure derivative

c_P =specific heat (kJ/kg-K)

C_a =constant in the reaction rate equation (s^{-1})

C_P =molar heat capacity at constant pressure (J/mol-K)

C_V =molar heat capacity at constant volume (J/mol-K)

d =maximum stable grain boundary/particle size (m)

d_p =average particle size (μm)

D =diffusion constant (m^2/s)

E =internal energy (J)

E_a =activation energy (kJ/mol-H_2)

E_b =binding energy (J)

22

E_{bar} = energy barrier (J)

F = inhomogeneous term for the transient heat transfer equation (K/s)

G = molar Gibbs free energy (J/mol)

ΔG = molar Gibbs free energy of formation (J/mol)

ΔG_a = total molar activation energy of recrystallization (J/mol)

$\overline{\Delta G}$ = molar nucleation critical free energy (J/mol)

ΔG_a^o = molar activation free energy of grain boundary diffusion (J/mol)

ΔG_a^{ex} = entropy-generated molar free energy barrier (J/mol)

ΔG_o = standard molar Gibbs free energy of formation (J/mol)

G_s = shear modulus (Pa)

h = heat transfer coefficient (W/m^2-K)

$\bar{h}$ = hardness of the material

H = molar enthalpy (J/mol)

ΔH = molar enthalpy of formation or reaction (J/mol or kJ/mol)

ΔH^0 = heat of absorption $\left(=\left|\Delta H\right|/M\right)$ (kJ/kg)

ΔH_o = standard molar enthalpy of formation (J/mol)

$\delta \Delta H$ = change in the molar enthalpy of formation (J/mol)

I = rate of growth of critical nucleus (s^{-1})

k = thermal conductivity (W/m-K)

k_B = Boltzmann constant (1.3806503$\times$10^{-23} J/K)

K = hydraulic permeability (m^2)

K_D = macroscale hydraulic permeability (m^2)

K_L = rate constant for the Langmuir isotherm (atm^{-1})

Kn	=gas phase (hydrogen) dimensionless Knudsen number $\left(= \Lambda_g / \sqrt{K_D}\right)$
K_N	=nucleation rate constant (s^{-1})
K_r	=rate constant for the reaction rate (reaction dependent)
l	=length of the cylinder or slab (m)
$\bar{l}$	=characteristic length scale (m)
L	=distance between heat and mass transfer surfaces or overall length scale for the hydrogen reactor (cm)
L^h	=molar latent heat (J/mol)
$\bar{m}$	=absorption reaction rate (kg/m^3-s)
M	=molecular mass of hydrogen (kg/mol-H$_2$)
M_b	=boundary mobility (m/J-s)
n	=number of moles (mol)
n_o	=atoms per unit volume (m^{-3})
N_A	=Avogadro number
N_{eq}	=nucleus of critical size at equilibrium
P	=pressure (atm or Pa)
$\bar{P}$	=dimensionless universal pressure
Q	=total heat supplied to the system (J)
r	=pore or particle radius (m)
$\bar{r}$	=rate of atom transfer (s^{-1})
R	=universal gas constant (8.3144 J/mol-K)
s	=number of atoms at the nucleus interface
S	=molar entropy (J/K)

ΔS =molar entropy of formation (J/mol-K or kJ/mol-K)

ΔS_o =standard molar entropy of formation (J/mol-K)

t =time (s)

Δt =absorption time according to the DOE 2010 goal (s)

T =temperature (K)

T_o =reference temperature (K)

ΔT $= T - T_o$ (K)

u =grain growth rate (m/s)

$\mathbf{u}$ =gas phase velocity vector (m/s)

$\bar{V}$ =dimensionless ratio of the molar volume to the standard molar volume $(T_o, P = 0)$

V_{ex} =dimensionless excess volume

V_R =dimensionless relative volume

V_T =dimensionless thermal expansion ratio

x =position (m)

Greek letters

α =coefficient of thermal expansion (K^{-1})

$\bar{\alpha}_{eff}$ =thermal diffusivity (m^2/s)

β =temperature coefficient in the transient heat transfer equation (s^{-1})

γ_a = dimensionless energy accommodation coefficient for the hydride particle surface

γ =surface energy (J/ m^2)

γ_G =Grüneisen parameter

Γ =surface concentration (m^{-2})

$\Delta_{M \to MH_2}$ =surface energy term (J/ m^2)

ε =dimensionless porosity

$\bar{\varepsilon}$ =bulk modulus derivative function

ε_b =binding energy in the Langmuir isotherm (J)

ζ =constant (m^2)

η =destabilization constant at room temperature (m^{3}Pa/mol)

η_h =dimensionless parameter arising in the solution of the transient heat transfer equation

η_{PV} =destabilization constant for the PV contribution (m^{3}Pa/mol)

η_{Cv} =destabilization constant for the heat capacity contribution (m^{3}Pa/mol)

η_S =destabilization constant for the entropy contribution (m^{3}Pa/mol)

η_V =destabilization constant for the thermal expansion contribution (m^{3}Pa/mol)

Θ_D.   =Debye temperature (K)

θ =coverage ratio (dimensionless)

ι =distance between the crystalline core and the deformed region (m)

λ =eigenvalue (s^{-1})

λ_{inc} =incident wavelength (cm)

λ_{sc} =scattered wavelength (cm)

Λ =mean free path (m)

μ =viscosity (kg/m-s)

μ_g	=chemical potential of the gas phase (J/mol)
μ_l	=chemical potential of the gas phase (J/mol)
ν_o	=rate at which an atom attempts a phase transition to the crystalline state (s^{-1})
ν_P	=Poisson ratio
ξ	=dimensionless parameter arising in the solution of the steady heat transfer equation
ρ	=density (kg/m^3)
υ	=molar volume (m^3/mol)
υ_o	=molar volume at standard pressure and temperature (m^3/mol)
ϕ	=dimensionless parameter in the effective thermal conductivity model
Φ	=dimensionless eigenfunction

Subscripts

ads	=adsorption
b	=binding
bar	=barrier
C	=condensed phase
C_V	=heat capacity contribution
dec	=decomposition
e	=electron
eff	=effective quantity
eq	=equilibrium

ex	=excess
flat	=flat interface
f	=fusion
g	=gas phase
h	=heat transfer
H_2	=molecular hydrogen
l	=liquid phase
m	=mass transfer
max	=maximum
M	=magnesium or metal phase
MH	=magnesium hydride or hydride phase
o	=reference state
opt	=optimal
p	=phonon
pore	=pore or nanopore
PV	=*PV* contribution
s	=sublimation
s	=solid phase, steady state
s,s	=solid phase at saturation
sim	=simulation
S	=entropy contribution
t	=transient

V_T =thermal expansion contribution

0 =initial condition

1 =boundary value

Superscripts

ads   =adsorption

des   =desorption

eq   =equilibrium

$'$, $''$ =reduced quantity due to destabilization

Other symbols

$\bar{f}$ =average value of quantity f

f' =the derivative of a function f with respect to x

SUMMARY

The potential impacts of nanostructuring metal hydrides on their hydrogen storage properties (storage capacity, kinetics, and thermodynamic properties) were investigated. First, a simplified heat and mass transfer scale analysis was performed to predict practical system-level length scales that provide an adequate absorption rate to meet the DOE 2010 rate goals for hydrogen storage in metal hydrides. Modeling assumptions were compared to a one-dimensional hydrogen reactor simulation with good agreement.

Several potential mechanisms for the reduction of the enthalpy of formation observed in ball milled metal hydrides were identified. It was shown that the increased surface and grain boundary energy as well as the presence of metastable crystalline phase in milled hydrides could play a role in reducing the enthalpy of formation, but that the predicted magnitude is too small to account for experimental observations. Excess volume was identified as the key parameter to explain the reduction in the enthalpy of formation of nanostructured metal hydrides observed experimentally. Using three equations of state, the excess enthalpy present in the deformed regions characterized by an excess volume was calculated. The theory was applied to the Mg/MgH_2 system and the results suggest that the excess volume provides a plausible explanation for the experimentally observed change in thermodynamic properties.

Then, the temperature dependence of the excess enthalpy present in regions characterized by an excess volume was calculated for metals and metal hydrides. At high temperatures, the

30

different contributions from the pressure-volume, heat capacity, entropy and work associated with the thermal expansion were studied separately and their magnitudes and signs were compared. It was found that the pressure-volume contribution opposes and dominates the other three contributions at both high temperature and excess volume, and that this contribution becomes the leading temperature dependent contribution to the enthalpy of a material. The conditions under which a temperature change will reduce the enthalpy of formation of metal hydrides were also given and the Mg/MgH_2 system was studied as an example. It was also demonstrated that the impact of temperature will be more favorable to a reduction of the enthalpy of formation if a large fraction of the metal hydride is in a state of small excess volume compared to a small fraction of the hydride in a state of high excess volume.

The excess entropy present in deformed regions of metals and metal hydrides characterized by an excess volume was also quantified using the equations of state. At high temperatures and high excess volumes, the excess entropy leads to a stabilization of the deformed regions with respect to multiple hydriding/dehydriding cycles. The impact of the energy barrier created by the excess entropy on the recrystallization rate of the deformed regions was quantified using a homogeneous nucleation and crystal growth model. At high temperatures and high excess volumes, due to the entropy generated energy barrier, metal hydride systems can have a recrystallization rate that is several orders of magnitude smaller than the recrystallization rates of regions containing low excess volume. This entropy stabilization can creates a regime where the reduced enthalpy of formation of the metal hydride could be maintained over multiple cycles because of the increased stability of the nanostructures responsible for the reduction in the enthalpy of formation.

Finally, an experiment to study the cycling properties of metal hydrides was designed using Raman spectroscopy and a transmission electron microscope (TEM). It was demonstrated that the release temperature of hydrogen could be accurately measured using the Raman spectroscopy and that the hydrogenation reaction could be observed as well. The possibility to study the impact of size distribution and milling method on the release properties of the hydride was also demonstrated using MgH_2 samples that were subject to different ball milling conditions. The size distributions of the nanoparticle samples were determined using the TEM and their composition was obtained from energy dispersive X-ray spectroscopy.

1 Introduction to the Hydrogen Economy and the Use of Metal Hydrides as Hydrogen Carriers

This chapter introduces the basic concepts and challenges related to the implementation of a hydrogen economy and the use of metal hydrides as potential hydrogen carriers.

1.1 Motivation for the Hydrogen Economy

Along with food and water, energy availability for the masses is without a doubt a major challenge for the 21st century. Driven by increasing world populations (see Fig. 1-1), an even faster increase in the per capita energy demand in developing countries (see Fig. 1-2), a decreasing availability of traditional sources of energy through fossil fuels, and the increasing concern about the need to curb the increase of CO_2 into the atmosphere before a tipping point is reached (Fig. 1-3), the need for a transformation to a sustainable energy supply from renewable sources has emerged as a dominant challenge of this century. Energy security is also a major

challenge faced by the United States and other nations worldwide. As a result, the hydrogen

initiative was subsequently launched by the US Government Funding Agencies in 2003.
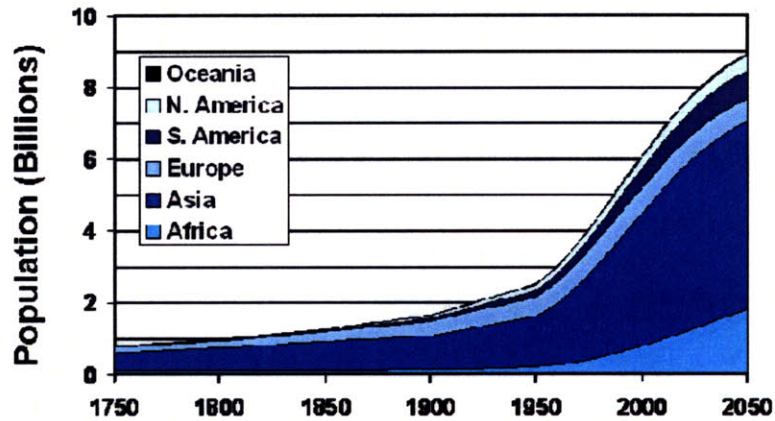
Figure 1-1. Predicted increase in the world's population, based on data until 2000 [2].
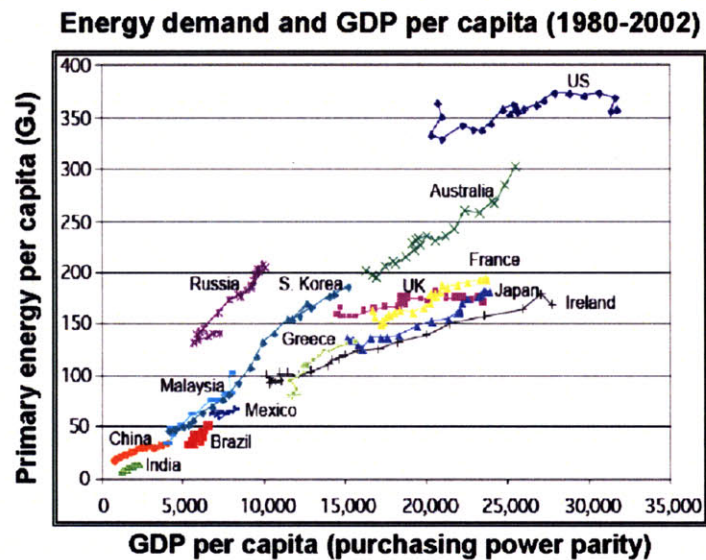
Figure 1-2. Energy demand and gross domestic product (GDP) per capita for various countries (1980-2002) [2].
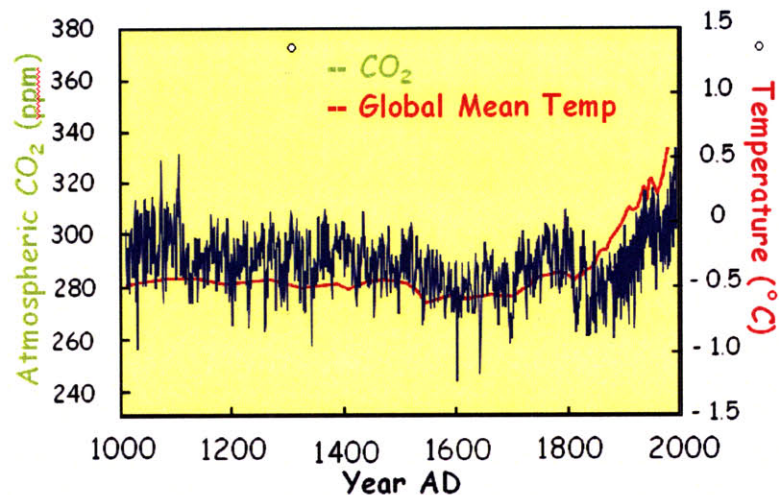
Figure 1-3. Change in the atmospheric CO$_2$ concentration and global mean temperature [2].

As a first step, a workshop was held in the spring of 2003, followed by a committee study which resulted in a report [1] which emphasized, firstly the appeal of hydrogen as an energy carrier whose release of energy produces only water as a by product without other pollutants or greenhouse gases, and takes advantage of the high efficiency enabled by hydrogen fuel cells. The report also stressed the challenges for the implementation of the hydrogen economy in terms of the enormous technical challenges to be overcome for its implementation, emphasizing that fundamental breakthroughs would be needed in understanding the physical processes involved in the production, storage and use of hydrogen. Infrastructures to provide for the transportation and distribution of hydrogen would also need to be developed to support a hydrogen economy. Understanding the atomic and molecular processes that occur at the interfaces of materials with hydrogen was identified as crucial to producing the new materials that would be needed for these fundamental breakthroughs to occur. The discovery of these new materials, new chemical

processes and new synthesis techniques that would be required could only be achieved by initiating a major basic research program with these objectives.

Such a research program was subsequently launched by the Basic Energy Sciences Office of the US Department of Energy (DOE) following the recommendations of the report, working in close collaboration with the DOE Office of Energy Efficiency and Renewable Energy and also the Office of Basic Energy Sciences that sponsored the report, thereby uniting the basic and applied science thrusts through a highly interdisciplinary effort involving chemistry, physics, biology and engineering, all working together to solve the multitude of challenges and opportunities identified in the report [1]. From these efforts, major research advances have occurred over a short period of time in the areas of hydrogen production, storage, and fuel cell performance, amplified by the corresponding efforts occurring worldwide. The enthusiastic response of the research community and the great interest of students in joining this effort have been noteworthy, leading to a series of other workshops (10 as of 09/2008), studies and initiatives in other areas of energy research and development. These efforts have also led to significant scientific and technological advances. Concurrently, industry has launched major initiatives so that the playing field is rapidly changing as breakthroughs are occurring throughout the energy science and technology landscape. Developments in biofuels, solar energy, battery technology, hybrid technology and clean coal, to name but a few are rapidly changing the energy outlook into the future. Even if a combination of technologies is likely to be necessary to address our future energy needs, present trends show that those technologies which offer immediate market value are most likely to attract additional investments and to get developed even faster.

1.1.1 Strategic Issues

Based on the DOE hydrogen requirements for the years 2010 and 2015 (see Table 1-1), the technology gaps for hydrogen as an energy carrier were identified and research directions for bridging these technology gaps were suggested in the Basic Research Needs Report [1]. In the meantime, the auto industry worldwide has taken a hydrogen-based vehicle seriously and has moved rapidly in getting hydrogen fuel cell automobiles on the highways to gain experience with this new technology, using presently available methods for hydrogen production and storage. Industry has focused mainly on accelerating hydrogen fuel cell development and the infrastructure needed for carrying out a hydrogen vehicle test program. While methods for hydrogen production from natural gas are presently adequate for automotive needs, the use of a fossil fuel natural gas precursor defeats the long term goal of using a sustainable, renewable energy source to provide the large increase in hydrogen production (20-fold by the estimate in Fig. 1-4) that would be required for transportation use. The development of a renewable route for large scale hydrogen production by methods, such as splitting water in a closed cycle water-hydrogen process or by a biologically-inspired process, remains a long term challenge where there are presently large opportunities for the research community.
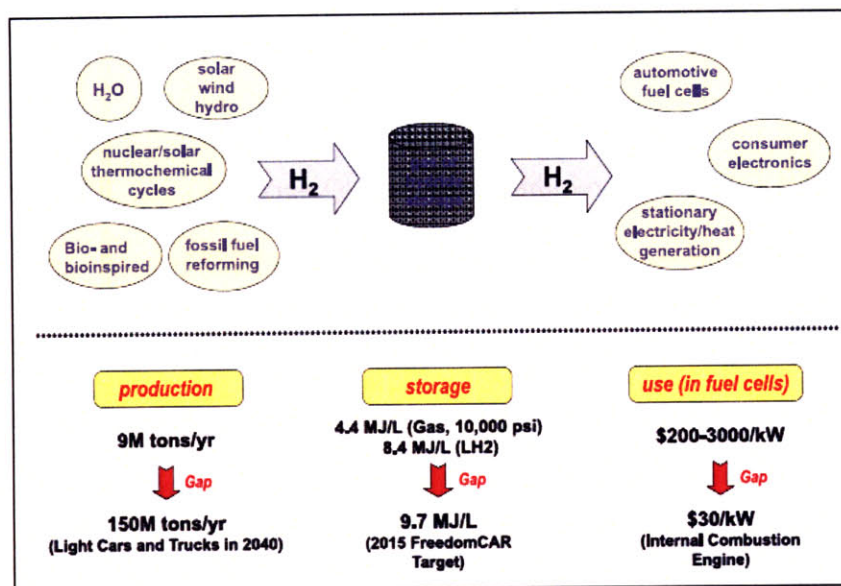
Figure 1-4. The technology gaps in hydrogen production, storage, and end use in a hydrogen economy [6].

The on-board storage of hydrogen to match US consumer appetites for a 500 km (~300mi) range for their family vehicle had been identified as the greatest challenge to the implementation of a hydrogen economy, because even the filling of the present fuel tanks of an automobile with liquid (or solid) hydrogen would fall short of meeting the DOE 2015 targets (Table 1-1). H_2 molecules strongly repel each other because of their spherical electronic shells and they have a very low mass density, even in the liquid or solid phase. This is why storage materials that bind hydrogen usually have a higher hydrogen density than liquid hydrogen, since the chemical bond between hydrogen and the storage material changes the H_2 electronic structure and allows H_2 molecules or atoms to come closer than they would in a gaseous or liquid phase.

The auto industry has taken a different approach toward addressing consumer appetites and is using increased operating efficiency and hybrid vehicle technology to manage the storage requirements. Although researchers from the auto industry are anxious for the academic

38

community and government-supported research laboratories to come up with a chemisorbed or physisorbed hydride solution for hydrogen storage, the auto industry does not now see the hydrogen storage problem as a technical show-stopper, though widespread public acceptance of the hydrogen gas cylinder technology has not been seriously tested. Thus, the auto industry is looking to the research community for major breakthroughs in renewable hydrogen production, reversible solid state hydrogen storage and higher efficiency hydrogen fuel cells to help make widespread adoption of the hydrogen fuel cell vehicle option a reality by mid-century. The arguments on the central role that new materials, and especially nanostructured materials, will play in these breakthroughs, as presented in the 2003 hydrogen report [1], remain valid through the present time.

What has changed in the interim is the vital role that industry is now playing and the need for the research community to be in close contact with industrial R&D developments, and to play a role in the incubation of start-up companies to develop the new technology options that will be provided by future suppliers to the auto companies. Thus, one strategic issue for the planning of hydrogen research is the coordination, not only between basic and applied research by the multidisciplinary players, but also to look for opportunities where academic and national laboratory research could have a large impact on future industrial product development. An effective way to accomplish those goals and to raise awareness for the hydrogen economy could be to develop niche markets for current hydrogen technologies. For examples, there could be opportunities in portable energy storage where hydrogen technology could currently compete on cost, end-user convenience, and storage capacity basis with current battery technologies. The knowledge and capital generated from those niche market successes could further fuel the R&D necessary to develop new materials that could satisfy the evolving requirements of the auto

industry. We have seen the impact that private investment can have on the development of a technology in other fields, such as solar energy, where competition for market share has driven research towards roadmaps that follow the same pattern as Moore's law has set in motion for semiconductor electronics.

Table 1-1. DOE goals for selected properties of hydrogen storage systems and comparisons with the current state of research in metal hydrides and compressed hydrogen gas [3].

	Metal Hydrides	10,000-psi gas	DOE Goals 2010	DOE Goals 2015
Gravimetric capacity (specific energy)	<0.18 kg H_2/kg <5.9 kWh/kg	0.057 kg H_2/kg 1.9 kWh/kg	0.060 kg H_2/kg 2.0 kWh/kg	0.090 kg H_2/kg 3.0 kWh/kg
Volumetric capacity (energy density)	<0.15 kg H_2/L <5.0 kWh/L	0.039 kg H_2/L 1.3 kWh/L	0.045 kg H_2/L 1.5 kWh/L	0.081 kg H_2/L 2.7 kWh/L
Refueling rate	Too slow	Acceptable	1.5 Kg H_2/min	2.0 Kg H_2/min
Delivery temperature	Above 200°C	Room temperature	-30/85°C	-40/85°C
System cost	$16 /kWh	$16 /kWh	$4 /kWh	$2 /kWh
Cycle life	Not sufficient	Sufficient	1000 cycles	1500 cycles

A second strategic issue concerns scale. Projections of global energy needs imply a doubling in overall energy demand and a tripling of the electricity demand by the year 2050 relative to the year 2000. The only renewable energy source with sufficient capacity to meet these growing energy demands is solar energy, though other competitive technologies such as wind will play a large role in the near future as solar energy further develops. An increase from the present 14TW to 28-30TW by 2050 is expected to come from solar energy used for generating electricity

(photovoltaic), providing fuels (biofuels, water splitting, close cycle synfuels), and supplying space and water heating (solar thermal). In this big picture, with solar electric, solar fuel and solar thermal as the energy sources, electricity and hydrogen are identified as complementary energy carriers. When thinking of hydrogen as a chemical carrier of energy, its role in energy storage from the electric grid emerges as an interesting opportunity, as does the generation of close-cycle renewable synfuels using hydrogen from H_2O and carbon from CO_2 to produce a hydrocarbon fuel using sunlight as an energy source [4]. The latter research direction, denoted by "transformation and recycling of CO_2 into a new material", was also identified in the Declaration issued by the First World Materials Summit held in Lisbon in 2007 [5].

The need for breakthroughs with high impact follows from the huge scale of the energy challenge involving a multi-trillion dollar business worldwide. Therefore major emphasis must be given to those research directions which will have the potential for large orders of magnitude impact.

1.2 Challenges of Hydrogen Storage in Metal Hydrides and the Role of Nanotechnology

Hydrogen has the potential to become the most important energy carrier due to its overall abundance, easy synthesis, potential for implementation in a carbon-free emission cycle, and high efficiency when used in a fuel cell [1, 7, 8]. To improve the so far limited properties of hydrogen storage materials, new technologies must be developed. In the following chapter, we

review the main challenges associated with hydrogen storage and offer a review of how nanotechnology has been used to improve the properties of hydrogen storage systems.

Safety concerns and the relatively low volumetric density for conventional compressed hydrogen gas in storage tanks demand a better storage system [9]. Metal hydrides provide a good alternative for hydrogen storage due to the possibility of high volumetric and mass densities and long-term stability [10]. However, to reach the Department of Energy (DOE) requirements, improved reaction kinetics near room temperature, storage capacity, storage efficiency, and better cycling performance are required. Nanostructured materials have recently been investigated to address the limitations of bulk metal hydrides due to their unique chemical, physical, thermodynamic and kinetic properties.

The benefits of nanostuctures for hydrogen storage have been reported by many groups [11, 12, 13, 14, 15, 16, 17, 18]. A deeper understanding of the physical principles underlying nanoscale effects will no doubt facilitate the development of metal hydrides that address the requirements of the transportation sector. For metal powders and nanoclusters, it is essential to understand not only their potential storage capacities, but also the influences of size and property changes during the hydriding reaction. Such insights may hold the key to the successful design of hydrides, both from the size and the composition point of view. Fundamental questions to be answered are:

(1) What are the effects of size on the thermodynamic and kinetic properties of hydrogen storage, hydrogen transport and heat transfer?

(2) What are the mechanisms behind the observed hydrogen reactivity enhancement of nanostructured materials?

(3) How small must a cluster be to observe size effects on storage properties?

(4) How can nanostructures be stabilized to increase the cyclability of the system and prevent the destruction of the nanoscale properties by sintering?

(5) How are the electronic properties of metallic clusters affected by size and how will those changes affect the storage of hydrogen in metal nanoparticles?

Several reviews already summarize recent advances in hydrogen storage [10, 19, 20, 21, 22], describing progress made with carbon structures based on the physisorption process, and metal or chemical hydrides based on the chemisorption process, as well as other hydrogen storage media. In this chapter, the general concepts behind nanoscale phenomena and their potential for enhancing hydrogen storage will be summarized. I will also discuss the research priorities from a systems point of view and emphasize the trade-offs that must be made in order to design a storage system for practical applications. I thus hope to stimulate a more quantitative focus to better enable future experimental breakthroughs to occur.

This chapter begins with a brief introduction to the basic knowledge related to hydrogen storage in metal hydrides. Next, fundamental concepts and current experimental advances are presented to show how nanoscale materials address the main bottlenecks of hydrogen storage, namely: high release temperature, slow reaction kinetics, insufficient storage capacity, and poor thermal conductivity. The trade-offs accompanying the use of nanostructures are also addressed.

1.3 Basic Knowledge on Hydrogen Storage

In this section, the key concepts associated with hydrogen storage in metal hydrides are reviewed.

1.3.1 DOE Requirements

Some of the principal DOE requirements for hydrogen storage [3] are presented in Table 1-1, showing the current state of research in metal hydrides and pressurized gases. Present research is driven toward reaching the stated DOE goals. When considering the metal hydrides for hydrogen storage, each of those goals is strongly connected to fundamental properties of the hydrogen-metal system. For example, the refueling rate is a function of the kinetics of absorption of hydrogen into the metal, and includes energetic considerations, such as the potential energy barriers that could slow doen the reaction. Even if gravimetric and volumetric capacities have historically been the properties of choice for the selection of potential hydride candidates, all of the DOE requirements must be addressed to achieve on-board automotive performance that is comparable with the current oil-based technology. In addition, any storage system should have a good cyclability, meaning that the system should maintain its physical and chemical properties through multiple absorption/desorption cycles.

1.3.2 Metal Hydrides

A metal hydride is defined as a single-phase compound formed between a metal host and hydrogen. Binary hydrides can essentially be classified into three categories depending on the nature of the bonding between hydrogen and the metal host [10]. Ionic or hydrides salts (e.g. MgH_2, NaH, CaH_2) are formed by alkali and alkaline earth atoms and are characterized by ionic bonding between the hydrogen and metal atoms. Covalent hydrides are formed by non-metal elements like S, Si, C or B, and metallic hydrides (e.g. $LaNi_5H_6$, $PdH_{0.6}$, $FeTiH_2$) originate from the metallic bonding between hydrogen and either a transition metal, a rare earth, or an actinide-series metal. In addition, group IA, IIA, and IIIA light metals form metal-hydrogen complexes ($[AlH_4-]$, BH_4-), which form covalent or ionic bonds with a cation, giving rise to highly stable complex hydrides (e.g. $NaAlH_4$, $Mg(AlH_4)_2$) in which hydrogen usually resides at the corners of a tetrahedron with B or Al at the center.

1.3.3 Methods to Make Nanocrystalline or Nanoscale Metal Hydrides

Reducing the size of metal hydride particles leads to a dramatic change in their physical and chemical properties and it is currently the starting point in most metal hydride investigations. Methods like laser ablation, vapor condensation, sputtering, and ball milling of the metal hydride are conventionally used to produce nanograined materials. Ball milling is the most commonly used method among experimentalists due to its scalability and ease of use. The metal is placed

in a rotating cylinder or conical mill partially filled with an inert grinding media, such as balls or pebbles. The collisions between the grinding media and the metal cause fracturing and cold welding of the elemental constituent particles thus reducing the particle size, creating cracks and fresh surfaces, and producing some degree of alloying. The final result is a powder made of nanocrystals (~10-50 nm) which aggregate into larger grains (~300 nm). Often activation by annealing is required to cause an amorphous to crystalline structural transformation and to produce grain boundaries. Due to the high energy cost of both the processing and the resulting materials, the cyclability of the milled hydride is essential for making this approach both energy and cost efficient.

1.3.4 Hydriding Mechanism

The absorption of hydrogen to form a metal hydride consists of several steps which may be described using the long-range attractive/short-range repulsive Lennard-Jones potential. As the molecular hydrogen approaches the metallic surface, it encounters successive minima in the potential curve corresponding to molecular adsorption, atomic adsorption, and bulk absorption, as shown in Fig. 1-5: (i) physisorption for both activated and non-activated processes, (ii) dissociation and surface chemisorption, (iii) surface penetration and chemisorption on subsurface sites, and (iv) diffusion (see [21]).

Molecular hydrogen is first physisorbed on the surface of the metal. Physisorption is a process whereby a molecule adheres to a surface without the formation of a chemical bond, the adhesion usually being due to van der Waals forces or electrostatic attraction with energy levels approximating those of condensation (1-5kJ/mol) [23]. Physisorption is a reversible process

46

strongly dependent on both pressure and temperature. For monolayer adsorption, the Langmuir isotherm describes the coverage ratio θ (defined as the number of adsorbed molecules divided by the number of adsorption sites) as a function of pressure (P), binding energy (ε_b), temperature (T) and a rate constant (K_L).

$$\theta = \frac{K_L P}{1 + K_L P} \qquad (1\text{-}1)$$

$$K_L \propto T^{-1/2} \exp\left(\frac{-\varepsilon_b}{k_B T}\right) \qquad (1\text{-}2)$$

The weak bonding usually prevents significant absorption at room temperature, which is why hydrogen storage on high surface area materials like carbon nanotubes or metal organic frameworks is achieved only at cryogenic temperatures [24]. Other models like the BET (Brunauer-Emmett-Teller) model are capable of describing multilayer adsorption. The multiple layers are the result of the gas interacting with its condensate so that the binding energy approaches the condensation energy.

If the pressure and temperature are high enough, the adsorbed hydrogen is then dissociated at the surface and becomes chemisorbed. Chemisorption is the chemical combination of hydrogen with the metal to form a new compound, which characteristically has a binding energy well above 50kJ/mol. Both the host and the absorbate are chemically changed in the process and the initial compound is usually trapped irreversibly on the surface or within the bulk of the solid media. This involves an electron transfer between the metal and the hydrogen and may require thermal or catalytic activation due to the dissociation energy barrier.

47
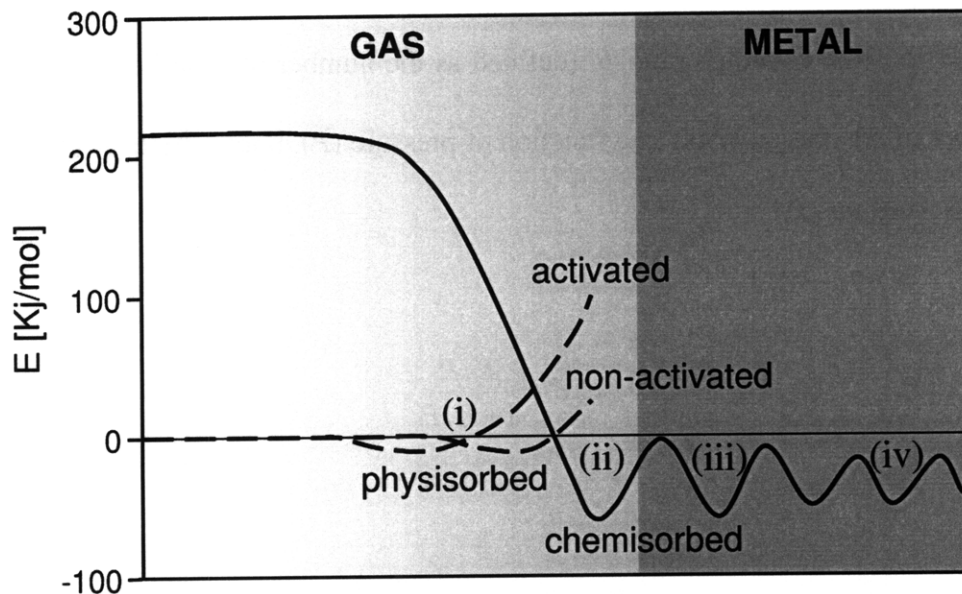
Figure 1-5 Potential energy curve for the Lennard-Jones potential for hydrogen binding to a metal: (i) physisorption for both activated and non-activated processes, (ii) dissociation and surface chemisorption, (iii) surface penetration and chemisorption on subsurface sites, and (iv) diffusion [21].

After surface chemisorption, the hydrogen atoms move to subsurface sites and rapidly diffuse through the material. This solution of H in the metal is referred to as the α phase (Fig. 1-6a). As the hydrogen concentration in the α phase increases, hydrogen-hydrogen interactions become important and a more stable phase nucleates (β phase) (see Fig. 1-6 b)). The β phase is characterized by a higher hydrogen density and often a different crystalline structure.

This phase transition is usually characterized by a crystalline structure change, a latent heat of reaction, a volume expansion, and a nucleation energy barrier associated with volume expansion and an interface energy between the phases.

(a)   (b)

| • hydrogen | • α phase | ○ β phase |
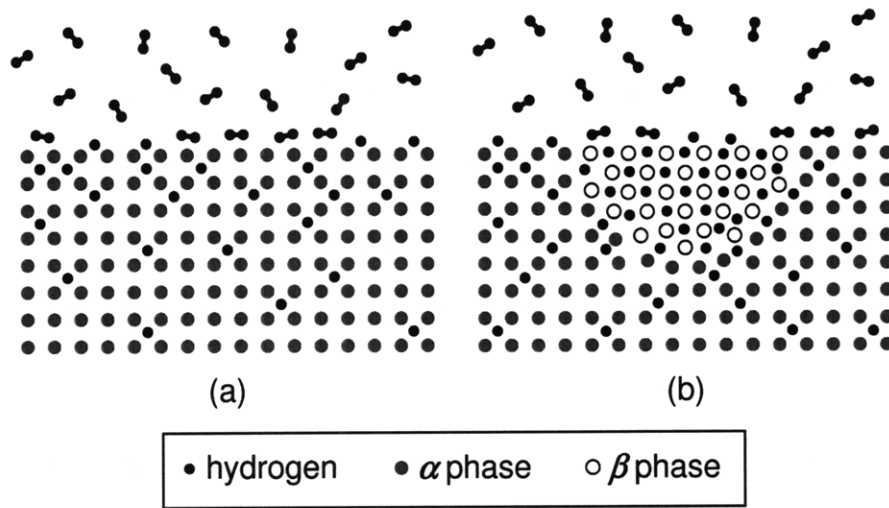
Figure 1-6. Simple representation of the nucleation of the β phase of the hydride host.

1.3.5 Thermodynamics of Reaction

The thermodynamics of the hydriding reaction serves as a starting point for understanding the positive effects that nanoengineering can have on the properties of metal hydrides. At a fixed temperature and pressure, the main force driving the hydride reaction is the Gibbs free energy (ΔG). A negative ΔG through a chemical reaction indicates that the process is thermodynamically favorable even if an energy barrier or slow diffusion process renders the reaction kinetically unfavorable. Figure 1-7 shows a sketch of the energy barrier for the hydriding reaction. Even if the hydriding reaction is thermodynamically favorable due to a negative Gibbs free energy ΔG, the reaction cannot take place at low pressure and temperature because of the energy barrier for adsorption E_{bar}^{ads} that must be overcome. The energy barrier E_{bar}^{des} is even larger for the desorption process, which explains the high release temperature for

49

metal hydrides. The heat released is directly related to the difference in internal energy ΔE between the initial and the hydrided states. Destabilizing the hydride will speed up the desorption kinetics and reduce the heat released, while the use of a catalyst can help both the hydriding and dehydriding kinetics. By destabilization of the metal hydride, we refer to a treatment that brings the energy level of the metal hydride closer to that of the metal. Examples and ways to destabilize metal hydrides are given in section 1.4.

The energy barrier in a reaction can be estimated using an Arrhenius rate equation that relates the energy barrier E_{bar} (also called the activation energy) to the temperature-dependent reaction rate $K_r(T)$:

$$K_r(T) \propto \exp\left(\frac{-E_{bar}}{k_B T}\right) \tag{1-3}$$

The Gibb's free energy in a bulk system is composed of the enthalpy of reaction (ΔH) (also called enthalpy of formation or heat of reaction/formation) and the energetic contribution due to the entropy change ($-T\Delta S$), where ΔS is the entropy of formation. ΔH represents the heat released or absorbed at constant pressure during the reaction and it is negative for the hydriding reaction. Neglecting surface reconstruction and entropy change in the lattice, the main contribution to ΔS is from the entropy reduction from the gaseous phase to the chemisorbed hydrogen (-130KJ/mol-K). The hydriding reaction is favored at low temperature where ΔH is large in magnitude and makes ΔG negative upon hydriding. At high temperature though, $-T\Delta S$ is larger in magnitude than ΔH, so that ΔG becomes positive and the dehydriding reaction becomes

thermodynamically favored. This explains why most hydrides must be heated above 200°C for

hydrogen release.
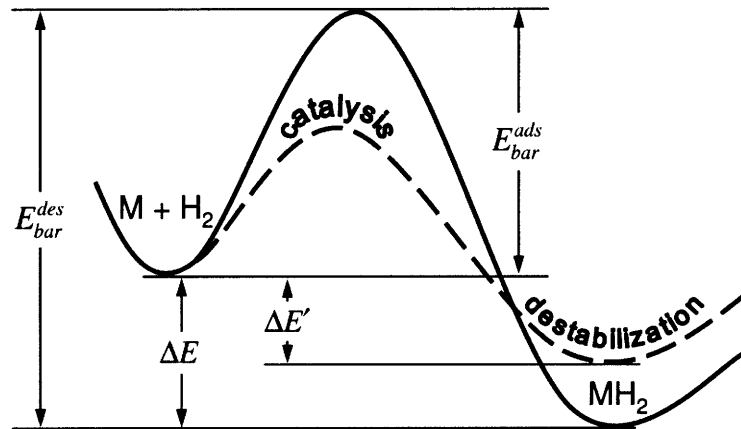
**Figure 1-7 Example of an energy barrier for hydrogen adsorption
and desorption.**

Starting from the molar free energy at the reference state (ΔG_0), one can calculate ΔG of an

ideal gas, in this case hydrogen, at a given temperature and pressure from

$$\Delta G = \Delta G_0 + \int_{P_0}^{p} \frac{RTdP}{P}$$

(1-4)

where P_0 is typically 1 atm. Equation 1-4 can be generalized for any solid, liquid, or non ideal

substance by replacing pressure with the activity coefficient (A) that takes account of all the non-

ideality of the compounds. For an ideal solid with no impurities, the activity is approximately

unity [25]. For the simple reaction $M + H_2 = MH_2$, ΔG is approximated by

51

$$\Delta G = \Delta G_0 + RT \ln\left(\frac{A_{MH_2}}{A_M P_{H_2}}\right) \tag{1-5}$$

where $\Delta G_0 = \Delta H_0 - T\Delta S_0$.

Values of the standard enthalpy (ΔH_0) and entropy (ΔS_0) of reactions are obtained from a van't Hoff plot as described below. The equilibrium pressure corresponding to the phase transition between the hydrogen dissolved in the α phase and the β phase can be drawn as a function of temperature; this is illustrated for several temperatures in Fig. 1-8(a). The van't Hoff plot is obtained by plotting the logarithm of the equilibrium pressures thus obtained against inverse temperature as shown in Fig. 1-8(b). Since equilibrium corresponds to $\Delta G = 0$, then ΔH_0 and ΔS_0 can be obtained, respectively, from the slope and intercept of the van't Hoff plot:

$$\ln P_{H_2}^{eq} = \frac{\Delta H_o}{RT} - \frac{\Delta S_o}{R} \tag{1-6}$$

Also, for the pressure equal to the reference state pressure, one finds the decomposition temperature T_{dec}:

$$T_{dec} = \frac{\Delta H_0}{\Delta S_0} \tag{1-7}$$

52
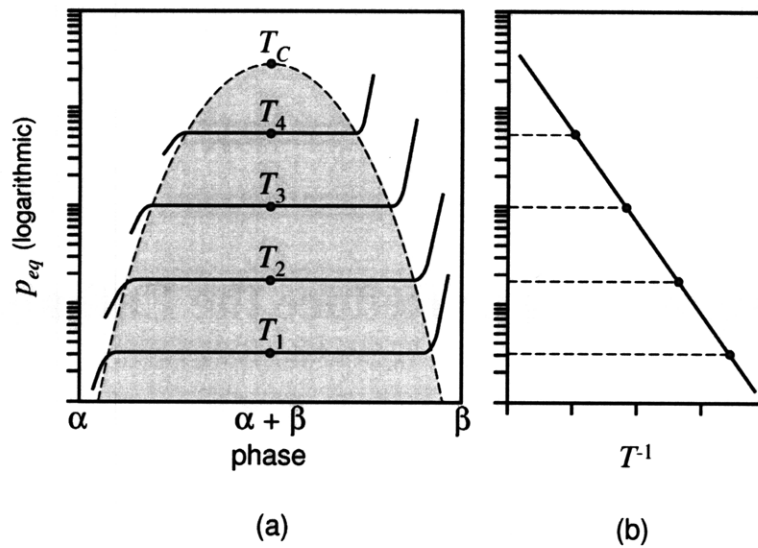
Figure 1-8. Obtaining the enthalpy and entropy of formation from a van't Hoff plot. In a) the plateau pressure is obtained at various temperature. In b) the equivalent molar enthalpy of formation is extrapolated from the plateau pressures.

1.3.6 Surface Energy

Due to the high surface area density in nanoparticles, the surface energy can be expected to play a major role in hydrogen absorption in nanostructured materials. The energy needed to separate two surfaces in contact is called the work of cohesion for surfaces of the same material, and the *work of adhesion* for surfaces of different materials. The surface free energy γ (or surface tension) is half the value of the *work of cohesion* and is defined as the work needed to

create a unit surface area.[1] It represents the excess energy that surface atoms have with respect to bulk atoms due to unsatisfied electronic bonds.

1.4 Nanoengineering to Reduce the Enthalpy of Formation

The strong chemical bonds that form between hydrogen and metals during chemisorption explain the high storage capacity of hydrides and their stability at room temperature, but these strong bonds also lead to an enormous energy release during the hydriding reaction. To release hydrogen, the hydride must be heated to high temperature in order to supply sufficient energy to break the chemical bonds. This energy requirement considerably reduces the energy efficiency of the hydrogen storage process if the enthalpy of formation is a substantial fraction of the energy content of the hydrogen (roughly 30% for MgH_2). Obtaining a destabilized hydride that is in thermodynamic equilibrium with the hydrogen gas closer to room temperature is the key to reducing the heat of formation which would in turn reduce the release temperature and increase the energy efficiency of the whole process. It is one of the most important challenges that must be addressed before automotive applications become practical.

---

[1] In general, for crystalline materials, the surface tension and the surface free energy will only be equivalent for a specific choice of the Gibb's dividing surface. This confusion in the literature often appears because the two are the same in liquids. A good discussion of this topic can be found in [26]. Using the exact formulation is necessary in order to generalize the thermodynamic relations in solids. In this thesis, we will simply adopt the term surface energy and use it as defined.

Figure 1-9 shows the range of binding energies (E_b) targeted by DOE. In most materials, hydrogen is stored by chemisorption (metal and chemical hydrides) or physisorption (carbon structures, metal organic frameworks, etc.). Physisorption bonding is usually too weak (<10kJ/mol) and demands cryogenic temperatures for significant storage capacity. Chemisorption shows a stability that is too high (>50kJ/mol) and demands high desorption temperatures. An ideal binding energy in the range of 10-50kJ/mol is achieved by reducing the chemisorption binding energy (destabilizing) or increasing the physisorption binding energy.
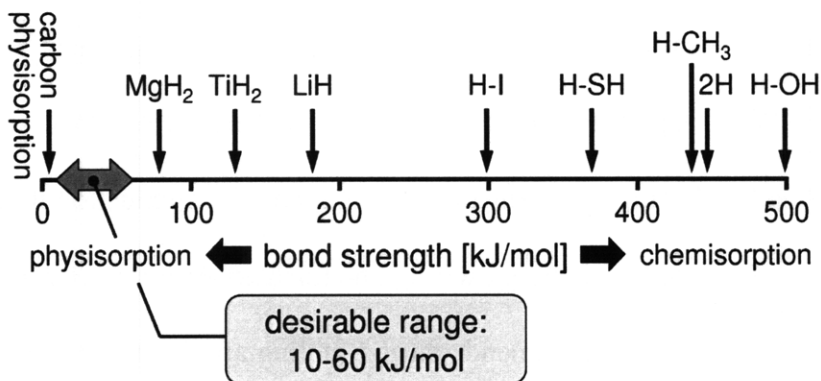
Figure 1-9. Targeted range of bond strengths that allow hydrogen release around room temperature, and values for the bond strengths for various materials.

A given material can exhibit both chemisorption and physisorption. The binding energies are quite different for the two approaches: too high for chemisorption and too low for physisorption. Effort is therefore necessary to increase (lower) E_b for physisorbed (chemisorbed) materials. Thermodynamic destabillization to lower E_b can be done chemically by introducing a new element or compound that forms intermediate states or structurally by introducing surfaces, grain boundaries, defects, and interfaces that would reduce the stability of the hydride relative to the

metallic state. Since storage capacity remains a priority, it is important to achieve destabilization while minimizing the storage capacity reduction that can arise from weaker metal-hydrogen bonding and the presence of added elements in destabilized hydrides. The relative potential for these methods is reviewed in the next sub-sections.

1.4.1 Chemical Destabilization

Introducing a new chemical species that reacts with the metal to form an intermediate state is one way to reduce the heat of formation. A classic example is Mg doped with 5% Si [27], as shown in Fig. 1-10(b). Upon hydrogen release, Mg will not return to its original crystalline structure, but instead will form an intermediate compound with a reduction in the enthalpy ΔH of roughly 40kJ/mol. This 40kJ/mol energy will not be released during the hydriding reaction, thus reducing the thermal management demands during fueling and lowering the heat input required for hydrogen release. The drawback of this method is the reduction of the uptake capacity from 7.6wt% to 5.0wt%. Similarly, one can add an element that reacts with both the metal and the hydrogen to form a destabilized hydrogenated state as shown in Fig. 1-10(c). In each case, however, there is a trade-off between the storage capacity and the reduction of the enthalpy of formation and release temperature. This loss is storage capacity is usually directly related to the concentration x of the dopant.

$$M+H_2 \qquad M + xA + H_2 \qquad M + xB + H_2$$

$$MA_x + H_2 \quad \Delta H''$$

$$\Delta H \qquad\qquad\qquad MB_xH_2$$

$$\Delta H'$$

$$MH_2 \qquad MH_2 + xA \qquad MH_2 + xB$$

$$\text{(a)} \qquad\qquad \text{(b)} \qquad\qquad \text{(c)}$$
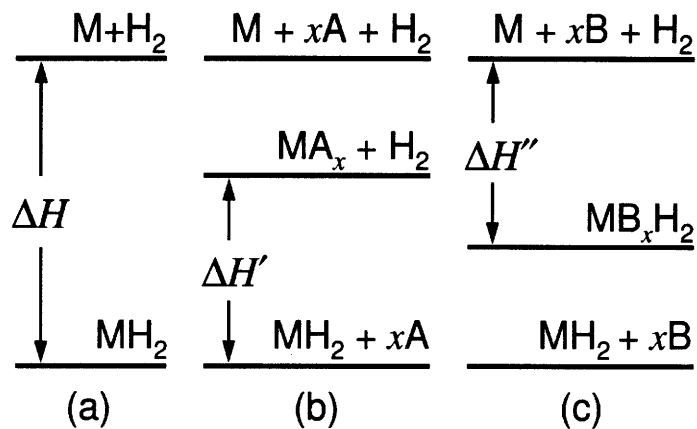
Figure 1-10. Two ways of reducing the enthalpy of formation by the introduction of a new chemical species. a) Standard reaction, b) stabilization of the metal phase, c) destabilization of the metal hydride phase.

1.4.2 Structural Destabilization

By contract to chemical destabilization where new elements are added to the hydride to modify its chemical properties, structural destabilization affects the properties of the metal and its respective hydride by introducing structures of defects that are not present in the bulk materials. As demonstrated in chapters 3 to 5 of this work, the incorporation of structures or defects at the nanoscale in the materials can have a profound impact on certain storage-related properties.

A typical way to achieve structural destabilization is through high energy mechanical treatments such as ball milling (see section 1.3.3). Such treatments will induce stress into the material and lead to the creation of compressed or elongated chemical bonds, new surfaces, extra grain boundaries, metastable phases, or dislocations. The presence of these structures affects the

hydrogen energy landscape within the metal hydride and can modify the thermodynamic properties of the hydrogen bonding. They also often create a network of pores and surfaces that can alter the reaction kinetics associated with the hydrogen storage/release and the thermal management within the sample. Many experiments have reported that the creation of nanostructures and the introduction of defects could lead to a modification of the thermodynamic properties, such as the enthalpy of formation of metal hydrides [28, 29, 30, 31, 32, 33, 34, 35, 36, 37] but a quantitative analysis of the relative importance of the different nanostructures remains to be given. This is the subject of this thesis. The impact of the most important defects and nanostructures on the storage capacity and the enthalpy of formation will be treated in subsequent chapters.

1.4.3 Recrystallization

The surface energy, lattice strain and defects, and excess enthalpy in the grain boundaries provide ways to lower the enthalpy of formation, but are usually unstable since the excess enthalpy thus gained will increase the free energy and drive recrystallization [38]. This is a major hindrance to the design of storage materials that have good cycling properties necessary for durable and cost-efficient automotive applications. Recrystallization occurs by the migration of the grain boundary of a growing crystal into surrounding particles and results in the partial lost of the nanostructure properties. In a kinetic context, one can relate the grain growth rate u to the excess free energy of the recrystallizing grains ΔG_{ex} [39] by:

$$u = \frac{M_b \Delta G_{ex}}{v} \qquad (1\text{-}8)$$

where M_b is the boundary mobility and v is the molar volume of the material. Grain boundaries with larger excess enthalpy will thus recrystallize much faster, leading to a reduction of the benefits of the initial nanostructures.

Boundary migration can be reduced by doping with incoherent second phase particles [40] to limit recrystallization. For a doping agent with a particle size r and volume fraction f, the maximum grain size diameter that can be stabilized by such doping is

$$d = \frac{3r}{4f} \qquad (1\text{-}9)$$

This approach has been used for micrometric systems but demands ultra-small particles or a high volume fraction to stabilize nanoparticles which could impair the hydrogen storage capacity. According to the Gibbs adsorption theorem, solute atom segregation at the grain boundary offers a way to stabilize nanoparticles by reducing the surface energy [41], which hinders recrystallization and prevents grain growth [42]. A simple equation can be used to approximate the effect of solute segregation at the grain boundary on the boundary mobility. For a surface density of solute Γ and an intrinsic mobility M_{b0} (mobility without the present of solute), the boundary mobility M_b is:

$$M_b = \frac{M_{b0}}{1 + \zeta T} .$$

(1-10)

Where the parameter ζ depends on the solvent and the particular solute that is studied [43]. As the surface density of the solute increases, the boundary mobility is reduced, which in turn diminishes the recrystallization rate (Eq. 1-8). This reduction in mobility is directly related to the reduction of the surface energy at the boundary which in turn results from the segregation of the solute. This highlights the competing behavior between the thermodynamic destabilization needed for a reduction of the enthalpy of formation and the thermodynamic stability needed to prevent recrystallization of the nanostructure.

In summary, nanoscale phenomena can be used to reduce of the heat of formation of metal hydrides, which in turn leads to a lower release temperature, faster kinetics, and better storage efficiency. Additional surfaces, interfaces, grain boundaries, and defects have a natural tendency to relax to more stable structures over time. Such relaxation processes will jeopardize the cyclability of the hydrides. Therefore, strategies to prevent the recrystallization of nanocrystalline materials must also be investigated, as part of the effort toward achieving successful hydrogen storage in metal hydrides. An approach to nanostructure stabilization based on the excess entropy content of heavily deformed regions is presented in chapter 5.

1.5 Reaction Kinetics and Reactivity

Reaction kinetics is another issue that must be addressed before practical application becomes feasible. Fast absorption kinetics directly translates to shortening the time spent refueling a hydrogen-powered car (this could be avoided by swapping the fuel tank each cycle) while fast desorption kinetics is essential for adequate performance. Nanostructures have shown impressive results when it comes to speeding up both the dissociation and diffusion kinetics [44, 45, 46, 47, 48, 49, 50, 51, 52]. In the case of MgH_2, 30 nm particles have been observed to release up to 5wt% in less than an hour at $300^{\circ}C$ compared to less than 0.5wt% for bulk over the same time period [44]. The bulk thermodynamic property differences between the pure metal and the metal hydrides are generally not the issue that is responsible for the slow kinetics, since the thermodynamic properties are usually favorable, but multiple energy barriers limit the reaction rate (see Fig. 1-5 and Fig. 1-7). As the reaction progresses, the limiting reaction rate changes from the dissociation and penetration of hydrogen at the interface to the nucleation of the β phase, and finally the diffusion of hydrogen through the β layer that eventually forms around the particle [53]. For the desorption process, the slow diffusion through the β layer and the high hydrogen dissociation energy barrier remain the primary factors limiting the reaction rates. The structural and electronic properties of nanostructures offer different ways to catalyze the different reactions, often eliminating the need for slow activation treatments at high pressure and temperature. The following section covers the principal phenomena responsible for the faster kinetic properties that are observed in nanostructures.

1.5.1 Surface Dissociation

The increased surface area and porosity of nanostructures naturally favor the dissociation of hydrogen atoms by offering a larger number of dissociation sites and allowing fast gaseous diffusion to the center of the material. In addition, the use of a proper surface catalyst like Pd [51] can dramatically improve the kinetics by facilitating the electron transfer and hydrogen dissociation in a process known as spillover [54] as shown schematically in Fig. 1-11.
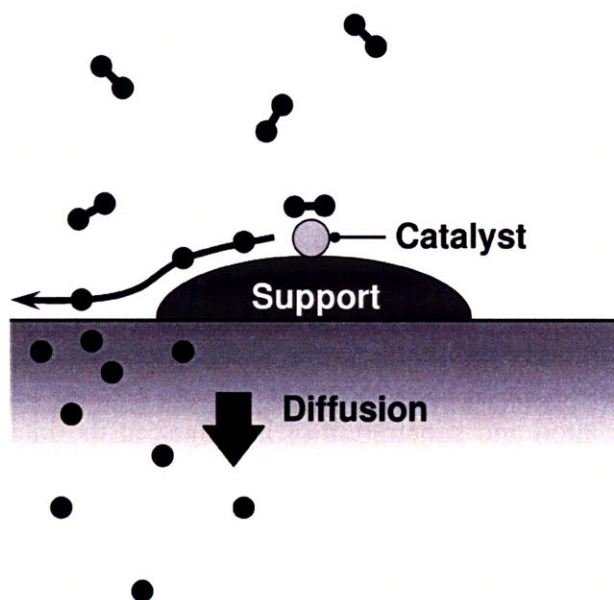
Figure 1-11. The spillover mechanism: the hydrogen molecules dissociate on the catalyst and the resulting hydrogen atoms diffuse into the metal.

During spillover, some hydrogen atoms remain attached to the catalyst, while others diffuse to the catalyst support and subsequently penetrate into the metal, where the hydrogen is said to spillover and interact directly with the metal. In spillover, the hydrogen molecule is dissociated

on the highly reactive metal catalyst on the surface from where the hydrogen diffuses into the surrounding storage media. A catalyst can also make the diffusion through the surface insensitive to the oxide layer that often forms on the metal. This removes the need for an activation process and increases the resistance to contaminants and air exposure.

1.5.2 Diffusion and Nucleation

The increased volume in the amorphous grain boundary weakens the binding between the metal and hydrogen atoms. This reduced binding energy favors site-to-site hopping for hydrogen and enhances diffusion in the α phase. Internal strain also widens the solubility distribution and makes certain binding sites more accessible at lower pressure. This can significantly reduce the time, and pressure necessary to saturate the α phase and initiate the hydride nucleation [48, 55, 56]. But the strain field at the α-β boundary due to the increased volume of the β phase is also associated with both a reduction in hydrogen transport from the β to the α phase in PdH and a reduction of maximum storage capacity in Mg_2Ni [57, 58]. Such competing behavior highlights the challenges in designing optimal metal hydrides since a desired improvement in one property can come at the cost of degrading another desirable hydride property.

Nucleation of the first β phase particle creates many interfaces between the β phase and the surrounding α phase. The interface energy barrier that must be overcome during the β phase nucleation can reduce the reaction rate. Multiple cracks, lattice defects, dislocations, and interfaces can help speed up the kinetics by favoring the heterogeneous nucleation of the β phase. In the case of dislocations, for example, nucleation is energetically helped if part of the high-energy dislocation is replaced by the new phase or if nucleation of a new phase along the

dislocation line reduces the excess free energy or strain energy associated with the dislocation [59]. Such defects can lead to irreversible processes, however, and the increase in reaction rates should not come at a cost to cyclability.

If the temperature and pressure are high enough, the β phase will nucleate from the saturated α phase and grow. It is known that the limiting reaction rate will be the diffusion through the β layer [60, 61, 62]. Nucleation of the β phase followed by the formation of a hydride layer prevent diffusion to the particle core, as represented in the single particle model, as shown in Fig. 1-12(a) [63, 64, 65, 66]. Since the diffusion rate in the β phase can be significantly smaller than in the α phase, minimizing this effect through control of the transportation path of hydrogen to the β phase could promote faster kinetics [53]. Figure 1-12 shows that for a sufficiently small particle, it might be possible to prevent the formation of a closed β layer that would limit access to the particle core during the hydriding reaction or prevent hydrogen from leaving the core upon the dehydriding reaction.
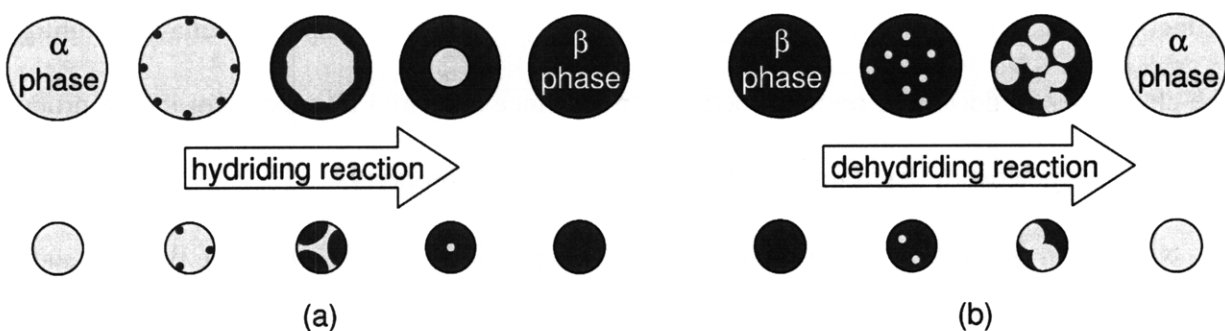
Figure 1-12. The impact of particle size on the reaction kinetics is seen from the earlier formation of a β layer around larger particles during the hydriding reaction (a) and the slower disappearance of this β layer around larger particles during the dehydriding reaction.

1.5.3 Catalysis and Doping

Section 1.5.1 reviewed many positive aspects of surface catalysts, but improvements in kinetics can also be obtained by distributing catalysts or doping agents inside the particles. Typical metals used are Pd, Fe, Ni, V, Zr, Mn, and Ti [67] along with transition metals (V, Cr, Mn), oxides, or AB_2 type compounds like $FeTi_2$. The distribution of the additives is generally achieved by sintering the material and the doping agent together or by high energy ball milling of the material followed by a low energy milling to disperse the additives. The mechanisms behind the improved kinetics associated with the additives are not fully understood, but reduction of the enthalpy of formation (resulting in a reduction of the energy barrier for dissociation) and improved diffusion in the β phase are the main enhancements observed [67]. For example, doping $NaAlH_4$ with 4% $TiCl_3$ reduces the heat of formation from 118kJ/mol to 80kJ/mol [68]. Doping Mg with carbon black, carbon nanotubes, or graphite flakes also speeds up the kinetics with no loss of storage capacity, while preventing particle growth by reducing the grain boundary mobility [69].

When a significant fraction of dopant relative to the host is used, the final product is usually referred to as a nano-composite. Good catalytic properties have been observed, for example, in Mg ball milled with 35wt% of amorphous transition metal alloys, where a 3.4wt% hydrogen release at 300°C is obtained in 30min instead of 75min as in pristine Mg [70]. The storage capacity, though, is half that of Mg. To avoid the loss of storage capacity resulting from the use of catalysts which have no hydrogen storage capacity, the mutual catalytic properties between different metal hydrides has been investigated. Ball milling different hydrides together was observed to yield dramatically improved results. A classic case is the mixing of MgH_2 with

Mg_2NiH_4 in which the final storage capacity in each remains unchanged, but the mixture offers a reduction in the desorption temperature for the more stable hydride [44]. A potential explanation for this effect is that the ternary hydride which releases hydrogen at a lower temperature offers a large interface that enhances the binary hydride desorption process [71]. It appears that the two phases maintain their sorption properties, but that one phase acts as a catalyst to the other, so that MgH_2 releases its hydrogen content around 275°C instead of above 350°C.

The above results show that the reaction kinetics of hydrogen storage can be significantly improved by nanotechnology. An increased reaction cross section, catalytic effects, and better diffusion all contribute to faster reaction rates without reducing too much the absorption properties of commonly studied metal hydride systems. The many orders of magnitude improvements in the reaction rates are encouraging, but further research is still necessary, since current absorption/desorption rates remain far below the DOE requirements.

1.6 Storage Capacity

Although the storage capacities of certain metal hydrides satisfy the DOE requirements for volumetric and gravimetric storage capacity, most still fall short of the DOE goals for 2015. One could, in general, expect the porosity of nanostructures to reduce the gravimetric and the volumetric storage densities. However, the increased surface area and porosity in nanostructures will offer additional binding sites on the surface and in the pores that could increase storage mainly through physisorption. The possibility of storing a significant amount of hydrogen on high surface area density materials has been a key driver in the investigation of hydrogen

sorption properties of nanotubes, graphite sheets, metal organic frameworks and aerogels [72, 73]. Adding physisorption capabilities to the high capacity chemisorption present in most hydrides would result in a fraction of the total absorbed hydrogen to be released at a lower temperature due to the lower binding that characterizes physical bonds compared to typical chemical bonds. In a practical context, this extra hydrogen could be used during the initial warming up of the fuel cell and used to heat the rest of the tank to activate the desorption of the chemisorbed hydrogen. Such a physi/chemisorption coexistence regime has not been explored yet. The following sections look at different mechanisms that could affect the storage capacity of hydrogen in chemisorption. The impact of nanostructuring on physisorption has not been addressed much in the literature and these effects will be quantified in more details in chapter 2.

1.6.1 Size Effects for Hydrogen Absorption in the α Phase

Although the direct condensation of hydrogen near room temperature in nanoporous structures may not be feasible, additional adsorption of hydrogen on nanoparticles has been predicted [30]. As the size of a particle is reduced, the fraction of atoms occupying surface sites is increased and therefore more adsorption sites are available. Moreover, the fraction of surface atoms residing at corners or edges of the nanoparticle particle is also increased. These edge or corner atoms are more weakly bound to the substrate (they have fewer nearest neighbors, and thus a higher coordination number) and can offer higher reactivity toward hydrogen. Models for small Pd clusters have shown that the higher coordination number of atoms positioned at the corners or edges of low-indexed planes can favor additional binding of hydrogen [74], and there are experiments showing H/Pd ratios of eight on small 1 nm Pd clusters [75]. Supersaturation of

the α phase due to surface and interface energies was also predicted[2]. It was calculated that the supersaturation of hydrogen in the Mg α phase could be three orders of magnitude greater than bulk values for nanoparticles with radii below 2 nm. This can be explained by an increase in the nucleation energy of the β phase due to the larger contribution of the metal hydride surface energy in nanoparticles. For practical purposes though, supersaturation in the β phase needs to be investigated as well, because the α phase in metal hydrides remains a low-density phase that is very unlikely to reach DOE's goals.

1.6.2 Size Effects on the Hydrogen Absorption in the β Phase

A density functional theory calculation on isolated Mg clusters with less than 60 atoms indicates the stability of supersaturated clusters with an H/Mg ratio of up to 2.25 (such small clusters cannot be characterized as a β phase despite their high hydrogen content because they lack the proper crystalline structure) [30]. The decreased binding energy of the extra hydrogen atoms also reduces the effective heat of formation of the system. In the case of extremely small clusters (less than 10 atoms), DFT simulations demonstrate that the enthalpy of formation may be tuned to permit the desorption of hydrogen at room temperature. One must bear in mind that these results refer to simulated, isolated clusters not subject to sintering or interaction with other clusters, and that no experiments on such small clusters have been reported so far.

Although a decreasing particle size is generally desirable for enhancing the hydrogen absorption properties in the α phase, many experiments have shown that size reduction will

---

[2] Based on a private conversation with Bruce Clemens and Stephen Kelly at Stanford University.

ultimately degrade the hydrogen storage properties in the β phase [76, 77]. For MgCu alloys, polycrystalline samples show a 2.6wt% capacity compared to 2.25wt% for nanocrystalline materials of 30 nm grain size. This reduction in hydrogen uptake is attributed to excess strain in the nanocrystals as well as to induced disorder that reduces the number of binding sites for hydrogen. Experiments on Pd nanograins have revealed that 1.3% and 2.4% strain in the <111> and <100> crystal planes, respectively, will deform the lattice and reduce the effective volume of certain octahedron sites (thus making these Pd nanograins less favorable for H occupation), while increasing the effective volume of others [87]. This distribution in binding site energies increases the diffusion in the α phase at low pressure, but also reduces the β phase storage capacity. This occurrence led to a 50% decrease in the β phase storage capacity for hydrogen. It is thus necessary to find the optimal size and milling conditions to optimize the absorption and kinetics jointly.

The above illustrates that nanoengineering can lead to an increase in the storage capacity of certain materials. These results must, however, be regarded critically, since there are major drawbacks and trade-offs associated with them:

(1) Most of the reported enhancements in hydrogen absorption consist of an increase in the α phase solubility, which remains far below the capacity of the β phase.

(2) The hydrogen storage increases associated with high surface coverage were only seen at low temperature where the weak physisorption bonds are stable.

(3) Most simulations and experiments are done on free standing clusters, and the effects of sintering and interaction with neighboring clusters that would reduce the surface area are neglected.

(4) The nanoparticle size necessary to obtain significant enhancement in hydrogen absorption remains in the single digit nanometer range, which is difficult to achieve for most materials.

(5) In many experiments, size reduction led to decreased storage capacity in the β phase, in some cases because conditions relevant to competing interactions were not optimized.

Much research remains to be done to determine whether or not additional physisorption in the β phase can be achieved, and if the bond strength can be made strong enough to achieve a significant increase in hydrogen storage capacity at room temperature. The effect of ball-milling-induced stress must be characterized quantitatively, in order to ensure that the decreased storage capacity in the β phase can be limited, if it cannot be increased. As before, consideration of the overall effect of size reduction shows that trade-offs are required in order to optimize the various properties of metal hydrides.

1.7 Electronic Size Effects on Hydrogen Storage

Many of the metal hydride property changes described above result from physical changes due to the nanostructuring of the materials, such as the addition of surfaces and interfaces and the introduction of lattice defects. In metallic materials, however, a size reduction can lead to a change in the chemical properties of the material due to a modification of the electronic interactions between the atoms composing the nanoparticles. The metallic properties of bulk materials come from the long-range interactions and the collective behavior of free conduction

electrons that create a continuum energy level distribution in the valence and conduction bands. Therefore, changes are expected in the properties of metals as the number of atoms in a cluster is reduced and the energy levels become discrete. One such phenomenon is the metal to insulator transition that occurs in clusters when the energy spacing between electronic levels becomes larger than $k_B T$. The ionization potential and electron affinity changes that occur with decreasing particle size in metals lead to significant changes in the chemical properties of metallic clusters. For example, the absorption of hydrogen in a metallic cluster is improved by increasing the tendency of the cluster to form chemical bonds with hydrogen during the hydriding reaction [78]. The following section provides a few illustrations of size-dependent phenomena; the interested reader should refer to an excellent book [78] for further information.

1.7.1 Size Effects on the Reactivity of Metallic Clusters

Studies of the hydrogen adsorption by transition metal clusters reveal that stable clusters composed of optimal numbers of atoms (8, 10, 16,...) with a high first ionization potential will not react with H_2 [79, 80, 53, 78]. This effect may be due to the difficulty in creating the chemical bond necessary to dissociate H_2. These experimental results can be explained in the context of free conduction electrons confined by the positive background created by the screened coulomb attraction of the nuclei. This gives rise to quantized energy levels inside the quasi-spherical atomic clusters and, as in the case of noble gases; a filled orbital shows a higher stability and is less likely to react electronically with other atoms or molecules to form bonds. Other experiments with Fe reported a decreasing coverage by hydrogen when the cluster size increases ($\theta \sim 1$ for Fe_{40} and $\theta \sim 0.8$ for Fe_{250}) which demonstrates how the reactivity of the

cluster with hydrogen can vary with size [78]. Furthermore, the adsorption of NH_3 on Co clusters has shown that higher coverage along with a lower heat of formation can be achieved by the proper choice of nanoparticle size. The heat of formation for the 12th NH_3 molecule on Co_{55} was measured as -61.1 kJ/mol [78] compared to -68.6 kJ/mol for the 12th NH_3 molecule on Co_{71}. This difference in ΔH is due to the lower coverage on Co_{71} which makes it more likely to create a stronger bond with hydrogen while minimizing the repulsive interactions between neighboring hydrogen molecules.

The above discussion highlights the fact that there is more to size reduction than simply increasing the surface area and introducing high energy structures with defects within the metal clusters. Size reduction can affect the chemical properties of the hydride itself in a non-trivial and nonlinear way. This means that a reduction of the grain size may not always lead to improved properties, since a smaller but electronically more stable particle could lower the hydrogen storage capacity and slow down the kinetic properties as compared to a large particle with a higher reactivity. Current methods of nanoparticle generation do not offer the size discrimination attributes necessary to take advantage of potentially promising size-dependent effects, but fundamental research on the size dependence of the hydrogen-metal interaction should remain a high priority, since size-dependent effects are expected to provide guidance for future experimental research that could lead to the breakthroughs needed to reach the DOE goals.

1.8 Thermal Management

Most research on metal hydrides is concerned with increasing the storage capacity and decreasing the release temperature of metal hydrides. However, developing strategies to reduce the heat generation and to provide efficient heat removal during the hydriding reaction is essential to provide optimal energy utilization efficiency and fast kinetics for metal hydrides. DOE requirements demand a reaction rate for the hydride formation on the order of $1.5 kgH_2/min$ [81]. For Mg, with an enthalpy for MgH_2 formation of $75 kJ/mol$ H_2, approximately 1MW of heat over more than 3 minutes is generated for 5kg of H_2. Assuming no heat removal (this is a reasonable assumption considering that a very low thermal conductivity of ~0.1W/mK in milled hydride powders has been reported [81]) in the hydride during the hydriding reaction, the temperature rise can be estimated from $\Delta T = Q/(nC_V)$. Here n is the number of moles, C_V is the specific heat, and Q is the total heat supplied to the system. For metallic Mg which has a specific heat of 24.9J/mol-K, this gives a temperature increase on the order of 1000°C. Without proper thermal management, this temperature increase would stop the hydriding reaction, which is suppressed with increasing temperature [82, 83]. Such large temperature excursions might even lead to local consolidation of the hydride which would destroy the nanostructure and prevent cyclability. A good thermal conductivity will also help during the dehydriding process by promoting the fast and uniform heating of the fuel tank required for a good rate of hydrogen release. In the following sections, the reduction in thermal conductivity k in nanostructures and strategies for thermal management of nanostructured materials are discussed.

1.8.1 Thermal Conductivity Reduction in Nanostructures

In bulk materials, the thermal conductivity has contributions from both electrons (k_e) and phonons (k_p), although k_p is dominant for dielectrics, while k_e is dominant for metals [84]. A spatially non-uniform temperature represents a non-equilibrium state for the energy distribution of heat carriers, and an entropy increase will drive the diffusion of high-energy electrons and phonons from warm to cold regions of the bulk solid. In nanostructures, the thermal conductivity becomes a function of size and structure, and a low thermal conductivity value is usually derived for nanostructured materials due to the following size effects:

(1) Porosity will decrease the thermal conductivity due to the presence of poorly conducting gas gaps between particles. The thermal conductivity of H_2 is roughly three orders of magnitude smaller than that of Mg leading to a significant barrier to thermal transport through the pore spaces, diverting the heat flow through the host material surrounding the pores. In addition, the pore size may be smaller than the mean free path of the gas molecules which is ~70 nm for air molecules at atmospheric pressure. The small pores limit the traveling distance of the gas molecules, which further reduces the thermal conductivity of the gas phase.

(2) For nanoparticles with a length scale smaller than the mean free path of the heat carriers, the thermal conductivity is reduced because the distance between successive boundaries becomes the effective mean free path [84]. At room temperature, the phonon and the electron mean free paths lie between 10 nm and 100 nm for most materials. Since the thermal conductivity is proportional to the mean free path in the kinetic theory approximation, a 5 nm nanoparticle will have a thermal conductivity roughly 2-20 times smaller than its bulk counterpart.

(3) The contact resistance between nanoparticles will also reduce the thermal conductivity in a nanopowder because of the following two factors: one is due to poor physical contact between the nanoparticles, and the other is due to the phonon reflection at the nanoparticle interfaces. This later factor being true even if the nanoparticles are made of the same material due to grain boundary misorientation at the interface.

1.8.2 Functional Matrices and Nanocomposites

The poor thermal transport properties of nanostructured materials can be improved by using conductive matrices to increase the heat transfer. The use of fins, foams, meshes and matrices formed by high conductivity materials like Cu, Al, Fe, and Ni have been reported [85], and the use of expanded graphite/metal-hydride compacts were shown to increase the conductivity from 0.1 to 3W/m-K [86] with only a 2.1wt% graphite additive. This opens up the possibility of designing functional nanocomposites, where an external matrix could play the double role of increasing the heat transfer while being chemically active in promoting desirable thermodynamic and kinetic properties of the hydride.

1.9 Summary and Thesis Outline

Metal hydrides are considered to be good candidates for hydrogen storage because they are safe to use and possess high volumetric and gravimetric hydrogen densities. Metal hydrides that satisfy all of DOE's requirements for storage capacity, kinetics, cyclability, cost, and release

temperature are not currently available. However, nanotechnology has opened new research directions offering additional ways to address a number of present bottlenecks associated with the use of metal hydrides for hydrogen storage applications. Specifically, nanoengineering can speed up the kinetics, reduce the hydrogen release temperature, and lower the enthalpy of formation. The impacts of nanoengineering on metal hydride properties are summarized in Table 1-2.

Table 1-2. Summary of the benefits and detriments of nanoengineering on selected metal hydride properties.

	Storage capacity	Kinetics	Enthalpy of formation	Heat transfer	Cyclability	Release temperature
Increased surface area	Increased physisorption	Increased surface dissociation	Decreased (nanograined materials)	Decreased	Potentially decreased	Potentially decreased
Increased grain boundaries	Decreased	Increased diffusion (α phase)	Potentially decreased	Decreased	Potentially decreased	Potentially decreased
Doping with catalysts	Decreased for excessive doping	Increased	No observed effect	Decreased	May help reversibility	Decreased
Increased porosity	Potentially increased physisorption	Faster gas diffusion	No observed effect	Decreased	No observed effect	No observed effect
Formation of nano-composites	Mean of the components	Increased	Potentially decreased	Decreased	Potentially increased or decreased	Decreased
Doping/ alloying	Potentially increased or decreased	Potentially increased	Decreased	Potentially increased or decreased	Potentially increased or decreased	Decreased

Although the benefits of nanotechnology are generally recognized, the description of the impact of nanostructures on key hydrogen storage parameters such as kinetics, storage capacity, release temperature, thermodynamic properties currently remain mostly qualitative. Moreover, the exact processes by which nanostructures, such as particles or grains, are generated are not

fully understood which makes it hard to generate metal hydride samples with desired storage properties. Experiments also demonstrate that while nanotechnology can help improve certain properties such as the reaction kinetics, it can also have adverse effects on other important storage parameters such as the thermal management of the sample during the hydriding reaction. All those unanswered questions and ambiguities render the design of a functional hydrogen system for car application very challenging. My work, summarized in this thesis, was aimed at quantifying the impact of nanostructuring on some of the most important properties of metal hydrides so that storage systems could be designed to meet the needs of automotive applications. In the following chapters, some of the impact of nanostructuring will be quantified.

In chapter 2, the potential to improve the storage capacity of a metal hydride by nanoengineering is evaluated and some limitations related to the generation of nanoparticles are quantified. The importance of thermal management is presented and the adverse effects of nanostructuring on the heat transfer properties of metal hydrides are presented. A regime map for the construction of a hydrogen storage system satisfying both the DOE's requirements for storage kinetics is presented.

In chapter 3, arguments stating why the enthalpy of formation is one of the most important parameters to control for hydrogen storage in metal hydrides are given. The impact of nanostructuring on the enthalpy of formation of metal hydrides is quantified. Finally, the excess volume present in deformed regions is identified as a leading structure responsible for experimental observations of the reduction of the enthalpy of formation in milled materials.

In chapter 4, the impact of temperature on the enthalpy of formation of metal hydrides containing excess volume is evaluated. Criteria to determine if the effect of temperature on the enthalpy of formation of a given metal hydride is positive are presented.

In chapter 5, the relaxation of deformed regions containing excess volume over multiple hydriding/dehydriding samples is assessed. The impact of excess entropy of deformed regions on their stability is evaluated and a way to stabilized the hydride over multiple hydriding/dehydriding cycles is proposed.

In chapter 6, the experimental characterization of MgH_2 powder milled under various conditions is performed using Raman spectroscopy and a transmission electron microscope.

Chapter 7 presents a summary of the present work and future projects and experiments related to this thesis work are presented.

2 Size Effects on Physisorption, Kinetics, and Heat and Mass Transfer

Reducing the metal hydrides particle size through chemical or mechanical treatment was shown to improve storage properties under certain conditions (see chapter 1). In chapter 2, we look at mechanisms that could lead to improve the storage capacity. Since the size of particles that can be reached is ultimately limited by the physical properties of the hydride, we also looked at limitations in terms of particle size that can be achieved through mechanical treatments. Finally, a simple estimate of the size of a storage system that represents the best compromise between improved storage capacity and kinetics and reduced heat transfer properties as the particle size is reduced.

2.1 Improved Physisorption in Nanopores

The next three sub-sections will look at potential mechanisms that could improve hydrogen physisorption in pores of nanometric size.

2.1.1 Capillary Condensation

Ball milled powder offers a network of small pores and cracks in which increased van der Waals attraction and surface tension effects could lead to increased storage capacity [87]. A good example of the potential of these effects is the capillary condensation of gas in small pores at pressures below the equilibrium vapor pressure. To find the relation between the condensation pressure in a pore P_{pore} of mean radius r compared to the condensation pressure over a flat interface P_{flat}, we first start from the requirement that at equilibrium, the free energy of the system should be at a minimum. This translates into the condition that an infinitesimal change in the radius of curvature of the pore should not lead to a change in the free energy of the system. Applying the condition that the chemical potential in the liquid and gaseous phase must be the same in both the flat and the curved interface we obtain the following equation:

$$dG = n(\mu_l - \mu_g) - \gamma dA = -2\pi r \left(\frac{RT}{\upsilon_l} \ln\left(\frac{P_{Pore}}{P_{Flat}} \right) r dr + 2\gamma dr \right) = 0 \qquad (2\text{-}1)$$

where μ_l and μ_g refer to the chemical potential in the liquid and gas phase, respectively. It is assumed that the molar volume υl of the condensed phase is much smaller than that of the surroundings. Solving for the ratio between the condensation pressure of a pore to that of the flat interface gives:

$$\ln\left(\frac{P_{pore}}{P_{flat}} \right) = -\frac{2\gamma \upsilon_l}{rRT}. \qquad (2\text{-}2)$$

80

This is known as the Kelvin relation [88, 89]. The Kelvin relation shows that gas condensation can be achieved in an environment where the pressure is ordinarily too low for condensation to take place. If ammonia is used as a hydrogen carrier for example, the Kelvin relation shows that the condensation pressure of ammonia at 310K can be brought from 13atm to less than half that value for pore sizes below 1 nm (see Fig. 2-1). In the case of hydrogen, this approach could only work for low temperature systems since hydrogen cannot be liquefied at any pressure for temperatures below its critical temperature of 33K. Moreover, the very small surface tension of liquid hydrogen (~1mN/m at 30K) limits capillary effects [90]. The use of capillary condensation for metal hydrides is therefore very challenging.
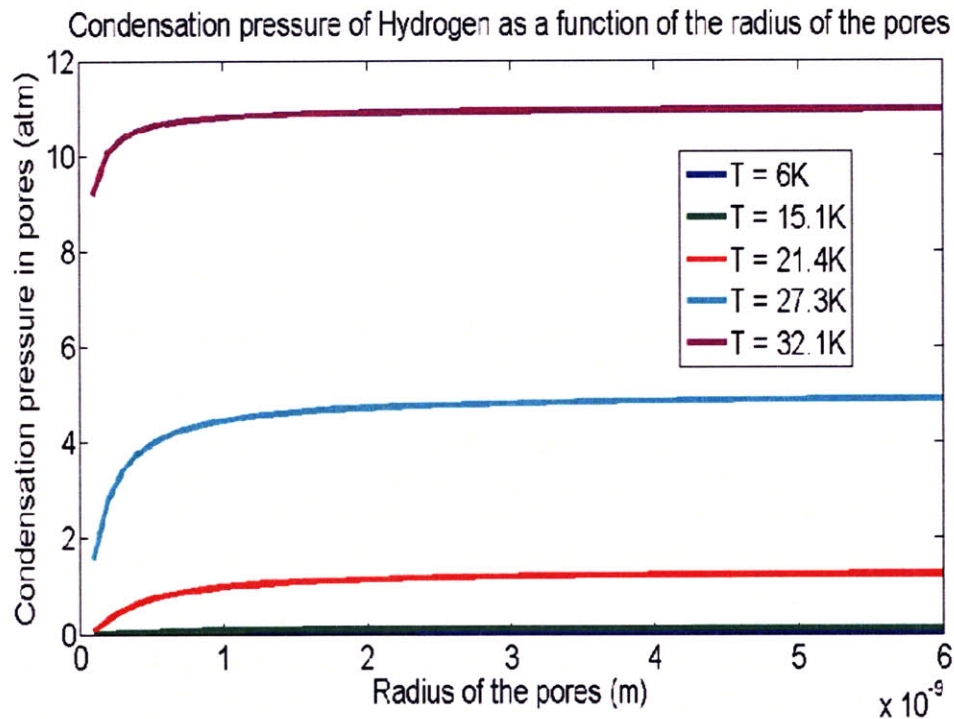
Figure 2-1. Condensation pressure of hydrogen as a function of the nanopore radius for various temperatures.

2.1.2 Increased Absorption in Sintering Generated Pores

Results from section 2.1.1 reveal that to take advantage of the capillary effects for hydrogen storage, one would need to use materials with pores of the order of 1 nm. For a material such as Mg, one would need to reduce the size of the pores beyond the smallest particle size that is achievable through ball milling (the minimum radius achievable is roughly 15 nm) (see section 2.2). To see if capillary condensation could be taken advantage of, we calculated the pore size that would be created from the contact of multiple nanoparticles. When nanoparticles of sufficiently small size are in contact, surface tension and the elasticity of the material will cause sintering which will in turn create a system of pores of sizes smaller than the particle size (see Fig. 2-2). From [88], one calculates that the size of the Van der wall bridge b (see Fig. 2-2) between two spherical nanoparticles as a result of surface tension is:

$$b = \left(\frac{(8 + \sqrt{42})R^2 \pi \gamma}{B} \right)^{1/3}. \tag{2-3}$$

And the bridge thickness δ is given by:

$$\delta = \frac{b^2}{R} \left(1 - \frac{2}{3} \left(\frac{b_o}{b} \right)^{3/2} \right) \tag{2-4}$$

where b_o is given by:

$$b_o = \left(12\pi R^2 \gamma / B\right) \tag{2-5}$$

From these equations, we used Pythagoras theorem to find the size of the pore r created between the nanoparticles:

$$r = \frac{2R\delta + \delta^2 + b^2}{2R - 2b} \tag{2-6}$$

Here, R refers to the particle radius, r is the pore radius created by the sintering, γ is the surface tension of the material, and B is the bulk modulus. Using values of $\gamma = 550 \text{mJ/m}^3$, $B = 45 \text{GPa}$ and $R = 15$ nm for Mg, we find that the pore radius would be $r = 2.6$ nm. Even if small, this 2.6 nm radius is still too small to take advantage of capillary effects (see Fig. 2-1) and we conclude that capillary effects are not likely to be of any use to increase the storage capacity of metal hydrides, such as Mg.
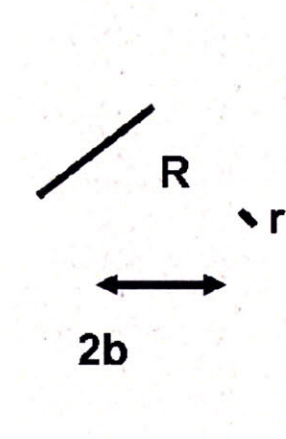
Figure 2-2. Schematic of the sintering between two nanoparticles that can lead to the formation of nanopores.

83

2.1.3 Ammonia as a Hydrogen Carrier

Because of the numerous diffuculties associated with the storage of hydrogen at ambiant conditions of temperatures and pressure, we looked at the possibility of using a carrier for the hydrogen atom. That carrier would ideally be used directly in a fuel cell for automotive applications or could be converted back to hydrogen prior to the combustion. An example of such a carrier that we investigated was ammonia. Because of the stronger attraction between molecules of ammonia than hydrogen, ammonia can be liquefied at reasonable pressures at room temperature. Condensation pressure could further be reduced by taking advantage of capillary effects at room temperature. Figure 2-3 plots the condensation pressure of ammonia as a function of the pore size at various temperatures. Figure 2-3 shows that capillary effects take place even at high temperatures due to the elevated critical point of ammonia (critical $T = 132^{\circ}C$). Nevertheless, an important reduction in the condensation pressure only takes place for radii smaller than 2 nm. Even if 2 nm is smaller than the smallest pore size that one can expect in milled metal hydrides, one could use an alternative carrier to store ammnia at low pressures. A porous silica aerogel or vycol glass could offer such an alternative because of their small pore size that can be as small as a few nanometers.

We investigated the possibility to use porous glass as a support for ammonia storage at room temperature. Vycor glass (SiO_2 @ 62.7%, B_2O_3 @ 26.9%, Na_2O @ 6.6% and Al_2O_3 @ 3.5%; pore diameter between 4 to 6 nm; porosity of 28%; surface area of $200m^2/g$) from Corning was subjected to 53 psi of NH_3 for 2 hours. The mass change measured from the NH_3 was not significant and we could not conclude that any capillary condensation of NH_3 took place. In accordance with Fig. 2-3, we thus believe that smaller pores would be needed to reduce the

condensation pressure of ammonia at room temperature. From chapters 2.1.1, 2.1.2, and 2.1.3 we thus conclude that capillary condensation is not promising for hydrogen storage given the small pore size and low temperature necessary to obtain a significant hydrogen condensation.
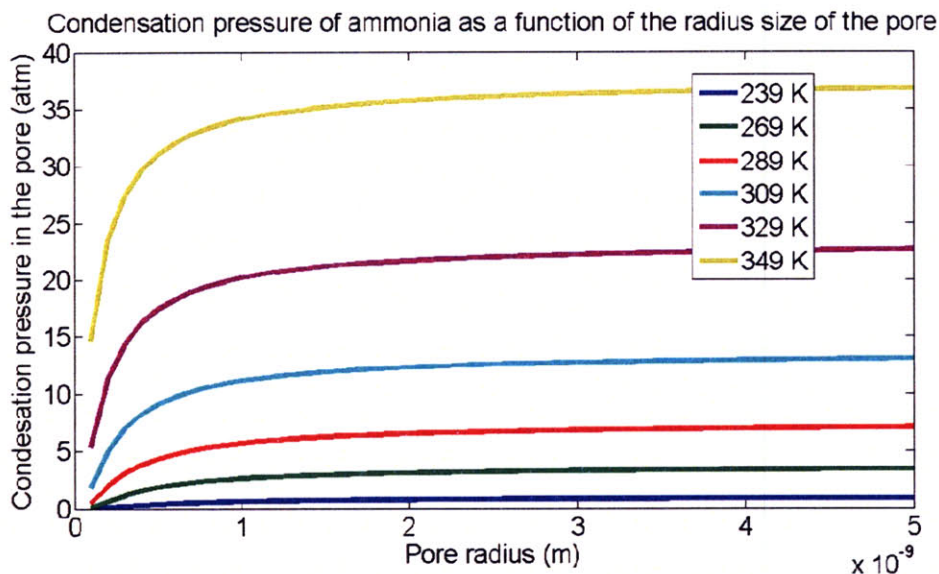
Figure 2-3. Condensation pressure of ammonia as a function of the nanopore radius for various temperatures.

2.2 Limitations to the Size of Nanoparticles and Nanosystems

Before trying to quantify the impact that nanoparticles or nanostructures can have on metal hydride properties for hydrogen storage, it is important to have an idea of certain mechanical and practical limitations regarding the size of nanoparticles that can be or should be generated.

2.2.1 Limitations from Mechanical Treatment

The most common way of reducing the particle size of a material to obtain nanoparticles with improved kinetic and thermodynamic properties is through ball milling (see section 1.3.3). The collisions between the grinding media and the metal cause fracturing and cold welding of the elemental constituent particles, thus reducing the particle size, creating cracks and fresh surfaces, and producing some degree of alloying.

To evaluate the smallest particle size that can be achieved using ball milling for a given material, it was assumed that the smallest particle size is equal to the smallest grain size obtainable [91]. The dominant mechanism assisting deformation is based on dislocation movement and interaction with the grain structure of the polycrystalline material. The limit for grain size is therefore determined by the reduction of the grain size to a length scale comparable to that of the dislocation structures involved with the deformation. The minimum grain size is thus related to the closest distance between two dislocations, such that in principle, a dislocation pile up leading to a refinement of the grain cannot happen when the grain size is smaller than the closest possible distance between dislocations [22]. Nieh and Wadsworth [91] evaluated the minimum dislocation distance d from the balance of the repulsive elastic energy between two dislocations and the hardness of the material $\bar{h}$:

$$d = \frac{G_s \bar{b}}{\bar{h}(1 - v_P)} \tag{2-7}$$

where G_s is the shear modulus, $\bar{b}$ is the Burgers vector, and v_P is the Poisson ratio. For Mg that will be further studied in this thesis, ball milling leads to a minimum particle size of roughly 15 nm using G_s = 17GPa, v_P =0.29, and h = 2.5 [92]. The Burgers vector $\bar{b}$ obtained by noting that the magnitude of $\bar{b}$ for a dislocation is of a magnitude equal to the interatomic spacing of the material, since a single dislocation will offset the crystal lattice by one close-packed crystallographic spacing unit [93]. For other popular metal such as Pd, the predicted particle minimum size is of roughly 5 nm [31] which agrees well with experimental data [74]. Mechanical treatments can thus be used to reduce the size of metal hydrides, such as Mg or Pd, to nanometric sizes. This is promising considering the low cost and potential scale that ca be reached for nanoparticles production using ball mills.

2.3 Practical Sizing of a Hydrogen Reactor Based on Heat and Mass Transfer in the Hydrogen Absorption Reaction

One of the fundamental issues with storing hydrogen in a metal hydride reactor for transportation applications is the slow rate of hydrogen absorption. Although this is partially addressed by high-energy ball milling, the diminished heat and gas phase mass transfer due to the reduced particle size remains a serious issue. In the case of MgH_2, the heat released during the hydriding reaction is of the order of 30% of the energy generated by the hydrogen

combustion in the fuel cell. This represents a significant energy waste that adversely impacts the overall energy efficiency of the system. This heat, when released over a short period of time, can also slow down the hydriding reaction kinetics significantly and make metal hydrides impractical for automotive applications. In this section, we perform a simplified heat and mass transfer scale analysis to predict practical system-level length scales that provide an adequate absorption rate to meet the DOE 2010 rate goals. Modeling assumptions were compared to a one-dimensional hydrogen reactor simulation.

Nanotechnology can lead to improved hydride properties [93]. In particular, MgH_2 reaction kinetics can be significantly increased by high-energy ball milling [47, 94, 95] and recent measurements [10] show that a powder with a 500 nm particle size has sufficiently fast reaction kinetics to absorb over 7 wt% in less than 100 s. However, such fine powders suffer from degraded heat transfer and gas phase mass transfer[3], which severely limits the hydrogen absorption rate. We have mentioned in section 1.8 that heat transfer can be improved by using porous metal or graphite compacts, or by designing cooling channels [81], while gas phase mass transfer can be improved by using distributed porous tubes or screens to supply hydrogen [96].

Numerous heat and mass transfer simulations have been performed, but most use the properties of low temperature hydrides, such as lanthanum nickel hydride ($LaHi_5H_6$). Only two simulations have been performed on MgH_2 reactors: Askri $et.$ $al.$ [97] used a two-dimensional simulation to show that radiative heat transfer is important for MgH_2, while it is negligible for $LaHi_5H_6$, and Marty $et.$ $al.$ [98] simulated a three-dimensional hydrogen reactor. Such simulations can be computationally expensive and have been performed only for specific

---

[3] Although the gas phase mass transfer in the pore space between the hydride particles is reduced for smaller particle size, the solid phase mass transfer, or diffusion of hydrogen into the hydride particle is enhanced. Here the solid phase mass transfer is considered to be part of the reaction kinetics (see section 2.1).

configurations, where the most common geometric configurations are cylindrical [97, 99, 100] and annular [100, 101, 102] reactors.

In contrast, we developed simple analytical tools to approximate the overall size of the reactor, based on the desired reaction rate and the properties of the hydride powder using a simplified heat and mass transfer analysis. Such results provide useful system-level design metrics for hydride reactors. These analytical tools were validated using a one-dimensional heat and mass transfer simulation, and reasonable agreement was found. Hydride particle size effects were introduced into the heat and mass transfer analysis through the hydrogen permeability and effective thermal conductivity model equations.

The key result is a procedure for estimating the distance between hydrogen gas sources and heat transfer enhancement surfaces required for sufficient heat and mass transfer rates that will not stall the reaction kinetics. This technique is practical for systems-level sizing of hydrogen reactor features. The appropriate convective boundary temperature to achieve optimal kinetics for reactor simulations was also approximated.

2.3.1 Model

The key transport processes in the hydrogen absorption reaction are shown in Fig. 2-4. A typical hydrogen reactor geometry [101] is shown in Fig. 2-4(a), where the macroscopic length scale is related to the separation distance between the hydrogen supply channels and the coolant passages. Within the hydride material (Fig. 2-4 (b)), gas phase mass transfer supplies the hydride particles with fresh hydrogen to be absorbed, while heat is transferred out through the effective media consisting of both the hydride powder and the hydrogen gas. At the particle

level, hydrogen is absorbed into the hydride particle and participates into the highly-exothermic

absorption reaction where heat is released.
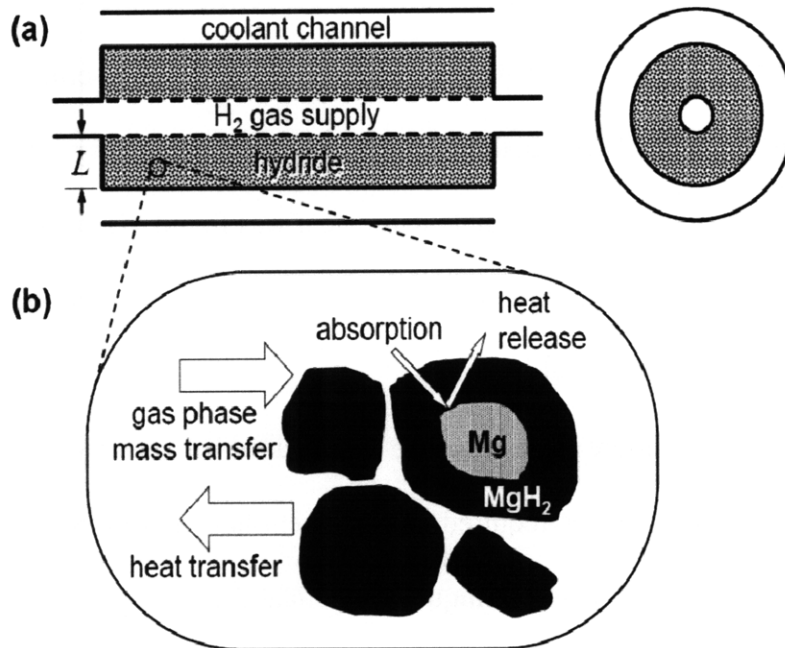
Figure 2-4. (a) A typical annular hydrogen reactor (see [101]) showing the hydrogen supply channel, the coolant channel, and the characteristic length scale L. (b) Heat transfer, mass transfer, and absorption reaction in MgH$_2$ particles.

2.3.1.1   Absorption Reaction Kinetics

The absorption reaction is a combination of several different processes at the particle level, namely physisorption, surface dissociation, surface penetration and chemisorption, diffusion through the hydride layer, and hydride formation [103]. The rate limiting process is initially chemisorption, but this quickly transitions into a regime where diffusion is the rate limiting

process [104]. Overall, diffusion through the hydride layer is the rate limiting process [105].

The diffusion limited model allows for a simplified treatment of the reaction kinetics [106, 107], where the key parameter is proportional to the diffusivity of hydrogen in the hydride phase and inversely proportional to the particle size squared. The diffusivity obeys an Arrhenius law $\left(D = D^0 e^{-E_a/RT} \right)$, where the activation energy E_a depends on the grain size. The most commonly used reaction rate model in hydrogen reactor simulations is [108]

$$\overline{m} = C_a e^{-E_a/RT} \ln\left(P/P_{eq} \right) \left(\rho_{s,s} - \rho_s \right) \tag{2-8}$$

Here, R is the ideal gas constant, T is the temperature, P is the pressure, C_a is a constant, and ρ_s and $\rho_{s,s}$ are the fictitious solid density and the fictitious solid density at saturation, respectively. The equilibrium pressure P_{eq} is determined by the van't Hoff equation

$$\ln \frac{P_{eq}}{1 \text{ bar}} = \frac{\Delta H}{RT} - \frac{\Delta S}{R} \tag{2-9}$$

in terms of the enthalpy (ΔH) and entropy (ΔS) of formation.

Using the absorption data obtained for 500 nm particles by Dornheim [10], a rate constant of $C_a = 2 \times 10^9 s^{-1}$ was found. The activation energy was obtained by fitting Eq. 2-8 and the fit yielded a result of $E_a = 104$ kJ/mol-H_2 for 500 nm particles.

The optimal temperature (T_{opt}), defined as the temperature which gives the highest reaction rate at a given pressure, is found by differentiating Eq. 2-8 and Eq. 2-9.

$$T_{opt} = \frac{\Delta H / R}{\Delta H / E_a + \ln\left(P/1 \text{ bar}\right) + \Delta S / R}$$ (2-10)

A plot of the normalized reaction rate $\overline{m}/(\rho_{s,s}\text{-}\rho_s)$ for 500 nm particles is shown in Fig. 2-5. At 10 bar, the peak hydrogen reaction rate occurs at 618 K, but if the temperature approaches 650 K due to insufficient heat transfer, the reaction will stall. From the plot, it is clear that significant absorption occurs in a temperature band that is ~150 K wide (roughly, from 500-650 K), which is a result that is used in a later section to size the reactor.
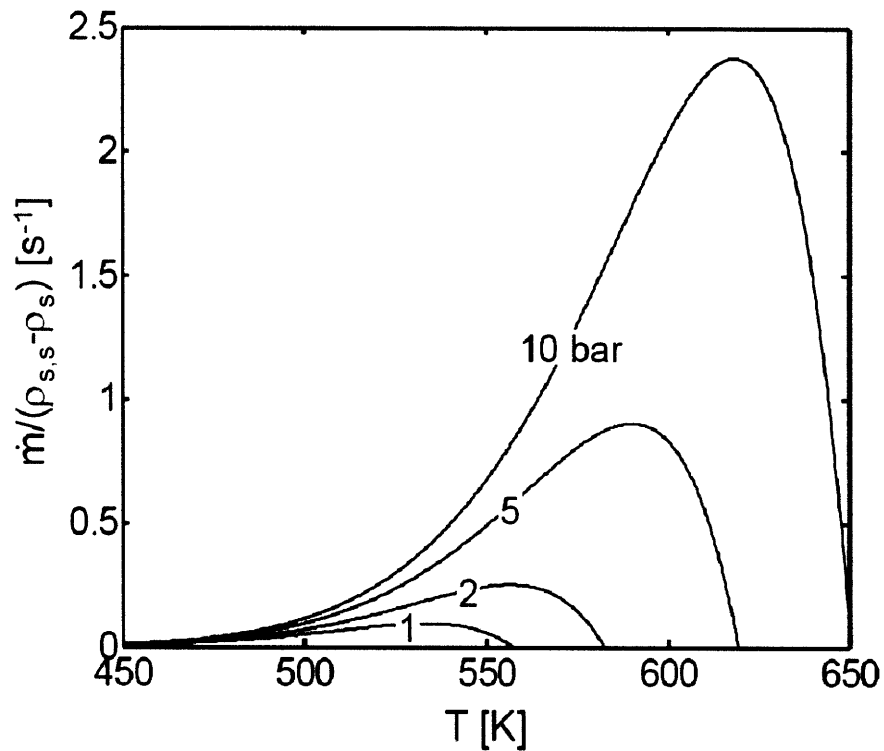
Figure 2-5. Approximate temperature dependence of the reaction rate model for 500 nm MgH₂ particles.

The reaction rate Eq. 2-8 determines the overall limit of the reaction kinetics. For MgH_2, the reaction rate is adequate for 500 nm particles, but too slow for 5 μm particles [10]. For the simplified heat and mass transfer analysis, the reaction rate was approximated as constant in time and uniform in space. This approximation was validated by comparison with a hydrogen reactor simulation, where reasonable agreement was obtained (see section 2.3.2.3). For a refueling rate that meets the DOE 2010 target and assuming 5 kg of total stored hydrogen in MgH_2, the required reaction rate is $\overline{m}$ =0.609 kg/ m^3-s, and the total absorption time is Δt=200 s.

A uniform and constant reaction rate allows the heat transfer to be analyzed separately from the gas phase mass transfer problem. This decoupling was achieved by analyzing mass transfer while assuming isothermal conditions, and by analyzing heat transfer while assuming constant gas density.

2.3.1.2   Hydrogen Reactor

Although practical hydrogen reactors are two- or three-dimensional in geometry, the relationship between the relevant length scales is investigated effectively by using a simple one-dimensional model. Typically, the hydrogen gas supply and thermal boundary conditions are defined on different boundaries, for example as shown in Fig. 2-4(a). The one-dimensional reactor model used in this study has a hydrogen gas supply on one boundary and a convective heat transfer thermal boundary condition at the other boundary as shown in Fig. 2-6(a). For simplicity, the gas supply is taken to be adiabatic, although this can also be modeled as a convective heat transfer boundary condition. The length scale (L) is the separation between gas supply and thermal boundary conditions, which is the relevant length scale of the overall reactor. Since many practical designs have more than one gas supply and/or thermal boundaries, the

model can be stacked to simulate a reactor with multiple, periodic heat and mass transfer surfaces as shown in Fig. 2-6(b). This analysis allows the determination of approximate length scales that allows adequate heat and mass transfer to meet the DOE 2010 goals without considering a specific reactor geometry.

The heat and hydrogen transport in the reactor was modeled in two distinct time regimes: transient and steady-state absorption. Transient mass transfer refers to the absorption phase where gaseous hydrogen flows into the reactor until it approaches mechanical equilibrium with the supply line pressure. In the heat transfer transient phase, the hydride powder heats up due to the hydriding reaction until a steady temperature profile is established. In the steady-state regime, the heat and mass transfer rates were compared to those sufficient to support the DOE 2010 absorption rate goal.
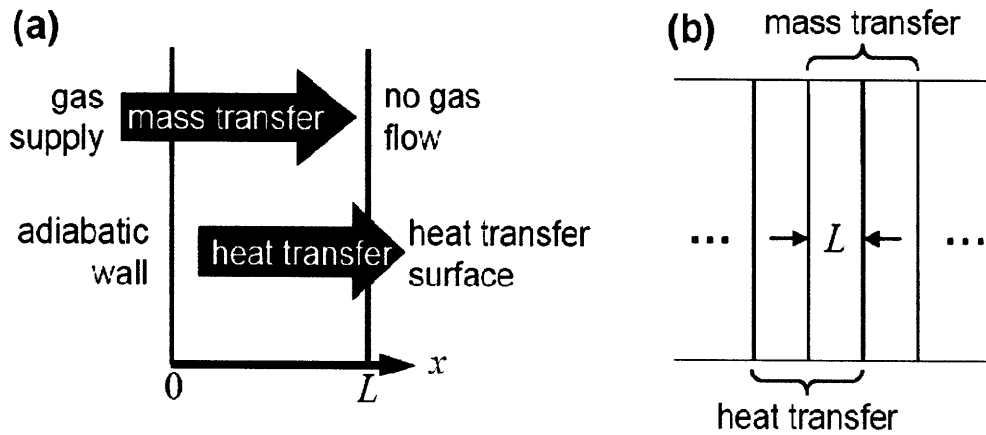
Figure 2-6. (a) Heat and mass transfer boundary conditions for the one-dimensional hydrogen reactor model. (b) Periodic spacing of heat and mass transfer surfaces to represent a hydrogen reactor with numerous hydrogen supply channels and cooling channels.

2.3.2 Analysis

This chapter presents the mathematical derivation of the main components of our model.

2.3.2.1   Gas Phase Mass Transfer

The conservation of mass for gas phase density ρ_g is given by

$$\varepsilon \frac{\partial \rho_g}{\partial t} + \nabla \cdot \left(\rho_g \mathbf{u} \right) = -\overline{m} \tag{2-11}$$

where ε is the porosity and t is the time. The gas is assumed to follow the ideal gas equation of state $P = \rho_g RT / M$, where R is the universal gas constant and M is the molecular mass of hydrogen. The local gas velocity $\mathbf{u}$ is related to the pressure gradient using Darcy's law,

$$\mathbf{u} = -\frac{K}{\mu} \nabla P \tag{2-12}$$

in terms of the permeability K and the hydrogen gas viscosity μ. Particle size effects were introduced using a permeability model, which is discussed in a later section. In order to decouple the gas phase mass transfer from the solid phase mass transfer and heat transfer, the assumptions from section 2.3.1 were enforced, i.e. approximately isothermal operation, and uniform absorption rate in time and space. Using these assumptions, Eq. 2-11 was rewritten in terms of pressure for a one-dimensional hydrogen reactor.

$$\frac{\partial P}{\partial t} = \frac{K}{\varepsilon\mu}\frac{\partial}{\partial x}\left(P\frac{\partial P}{\partial x}\right) - \frac{R\overline{T}\,\overline{m}}{\varepsilon M} \qquad (2\text{-}13)$$

The appropriate boundary conditions are fixed pressure at the gas inlet side ($x=0$) and no flow at the convective surface ($x=L$) to yield

$$P(0,t) = P_1, \quad -\frac{K}{\mu}\frac{\partial P}{\partial x}(L,t) = 0 \qquad (2\text{-}14)$$

The nonlinear term in Eq. 2-13 was approximated[4] as $\partial\left(P\,\partial P/\partial x\right)/\partial x \approx \overline{P}\,\partial^2 P/\partial x^2$ which gives a linear governing equation for the pressure:

$$\frac{\partial P}{\partial t} = \frac{K\overline{P}}{\varepsilon\mu}\frac{\partial^2 P}{\partial x^2} - \frac{R\overline{T}\,\overline{m}}{\varepsilon M} \qquad (2\text{-}15)$$

The transient time scale was determined from the related eigenvalue problem $K\overline{P}\Phi'' + \varepsilon\mu\lambda\Phi = 0$ with boundary conditions $\Phi(0) = 0$ and $\Phi'(L) = 0$. The lowest eigenvalue was calculated as $\lambda_1 = \frac{\pi^2}{4L^2}\frac{K\overline{P}}{\varepsilon\mu}$. Allowing for three time constants for full absorption $(1 - e^{-3} \approx 95\%)$ gives:

---

[4] Although this approximation introduces additional error, it is adequate to provide an estimate of the transient length scale for mass transfer. It is shown in a later section (see Figure 2-7, for example) that the steady state length scale is more than one order of magnitude more restrictive than the transient length scale for mass transfer, and therefore a precise evaluation of the transient mass transfer equation is unnecessary.

$$\Delta t = \frac{3}{\lambda_1} = \frac{12\varepsilon\mu L^2}{\pi^2 K \overline{P}} \qquad (2\text{-}16)$$

We solved Eq. 2-16 to obtain the length scale for mass transfer based on transient mass transfer

$$L_{m,t} = \frac{\pi}{2\sqrt{3}} \sqrt{\frac{K\overline{P}\Delta t}{\varepsilon\mu}} \qquad (2\text{-}17)$$

The steady solution was found from Eq. 2-13 in one dimension neglecting the transient term.

$$\frac{K}{\varepsilon\mu} \frac{d}{dx}\left(P\frac{dP}{dx}\right) = \frac{R\overline{T}\,\overline{m}}{\varepsilon M} \qquad (2\text{-}18)$$

Then Eq. 2-18 was integrated analytically to obtain

$$\frac{P}{P_1} = \sqrt{1 - \frac{\mu R\overline{T}\,\overline{m}L^2}{MKP_1^2}\left(2\frac{x}{L} - \frac{x^2}{L^2}\right)} \qquad (2\text{-}19)$$

The pressure evaluated at $x=L$ is a measure of how uniform the pressure is at this flow rate.

$$\frac{P(L)}{P_1} = \sqrt{1 - \frac{\mu R \overline{T} \, \overline{m} L^2}{MKP_1^2}}$$ (2-20)

The maximum gas flow into the reactor is achieved when $P(L)$ is equal to the initial pressure P_0. This leads to a length scale based on steady mass transfer of

$$L_{m,s} = P_1 \sqrt{\left(1 - \frac{P_0^2}{P_1^2}\right) \frac{MK}{\mu R \overline{T} \, \overline{m}}} \approx P_1 \sqrt{\frac{MK}{\mu R \overline{T} \, \overline{m}}}$$ (2-21)

where the last approximation holds when the H_2 supply pressure is much greater than the initial pressure, or $P \gg P_0$.

2.3.2.2   Heat Transfer

For the heat transfer, local thermal equilibrium between the solid and gas phase is assumed, and both convective (see, for example [107]) and radiative heat transfer[5] are neglected. The energy conservation equation is then given by

$$\left(\rho c_p\right)_{eff} \frac{\partial T}{\partial t} = \nabla \cdot \left(k_{eff} \nabla T\right) + \overline{m}\left[\Delta H^0 + \left(c_{P,g} - c_{P,s}\right)T\right]$$ (2-22)

---

[5] Although Askri *et. al.* [11] showed that radiative transfer is important for MgH_2, the difference in absorption time was off by a factor of two at most. Since our analysis was only approximate, this assumption was deemed adequate.

Here, T is the absolute temperature, ρ_s is the fictitious solid phase density, $c_{P,g}$ and $c_{P,s}$ are the specific heats of the gas and solid phase, respectively, and ΔH^0 ($=|\Delta H|/M$) is the heat of absorption. The effective heat capacity is defined as $\left(\rho c_p\right)_{eff} = \varepsilon \rho_g c_{P,g} + \left(1-\varepsilon\right)\rho_s c_{P,s}$. The effective thermal conductivity k_{eff} is calculated in a later section.

The key simplifications are a constant and uniform absorption rate (as before), and a constant effective heat capacity $\left(\rho c_p\right)_{eff}$. For one-dimensional heat transfer, Eq. 2-22 can be rewritten as

$$\frac{\partial T}{\partial t} = \overline{\alpha}_{eff} \frac{\partial^2 T}{\partial x^2} + \beta T + F \tag{2-23}$$

in terms of the effective thermal diffusivity $\overline{\alpha}_{eff} = k_{eff}\big/\left(\rho c_p\right)_{eff}$ and two additional coefficients:

$\beta = \overline{m}\left(c_{p,g} - c_{p,s}\right)\big/\left(\rho c_p\right)_{eff}$, and $F = \overline{m}\Delta H^0\big/\left(\rho c_p\right)_{eff}$.

The appropriate boundary conditions are an adiabatic boundary at the gas inlet side ($x=0$) and a specified heat transfer coefficient (h) at the other boundary ($x=L$).

$$-k_{eff}\frac{\partial T}{\partial x}(0,t) = 0, \quad -k_{eff}\frac{\partial T}{\partial x}(L,t) = h\left[T(L,t) - T_1\right] \tag{2-24}$$

The time scale was again determined from the lowest eigenvalue for the related eigenvalue problem $\overline{\alpha}_{eff}\Phi'' + \left(\beta+\lambda\right)\Phi = 0$ with boundary conditions $\Phi'(0) = 0$ and $k_{eff}\Phi'(L) + h\Phi(L) = 0$. This resulted in a transcendental equation for the eigenvalues,

$$\eta_h \tan \eta_h = Bi, \quad \text{where} \quad \eta_h^2 = \frac{\beta + \lambda}{\overline{\alpha}_{\text{eff}}} L^2 \tag{2-25}$$

where the Biot number is $Bi = hL/k_{\text{eff}}$. From the lowest eigenvalue λ_1, the time scale for three time constants was equated to the total absorption time limit and solved for $L_{h,t}$ numerically.

$$L_{h,t} : \Delta t = \frac{3}{\lambda_1} \tag{2-26}$$

For large Bi number (or, equivalently, for $T(L)=T_1$) Eq. 2-26 has a simpler expression. Using a modified second boundary condition for the transient eigenvalue problem ($\Phi(L)=0$), the lowest eigenvalue was obtained as $\lambda_1 = \left(\pi^2 \overline{\alpha}_{\text{eff}}/4 - \beta L^2\right)/L^2$, which gave a simpler form for the transient length scale.

$$L_{h,t} = \frac{\pi}{2} \sqrt{\frac{k_{\text{eff}} \Delta t}{3(\rho c_P)_{\text{eff}} + \overline{m}(c_{P,g} - c_{P,s})\Delta t}} \tag{2-27}$$

For MgH$_2$, we obtain $\overline{m}(c_{P,g} - c_{P,s})\Delta t > 3(\rho c_P)_{\text{eff}}$ although both terms are of the same order of magnitude. Thus, a rough estimate of the transient length scale was obtained by excluding the effect of the effective heat capacity.

$$L_{h,t} \approx \frac{\pi}{2} \sqrt{\frac{k_{eff}}{\overline{m}\left(c_{P,g} - c_{P,s}\right)}} \qquad (2\text{-}28)$$

For steady response, the governing equation reduces to

$$k_{eff} \frac{d^2 T}{dx^2} + \overline{m}\left[\Delta H^0 + \left(c_{P,g} - c_{P,s}\right)T\right] = 0 \qquad (2\text{-}29)$$

The solution for the given boundary conditions is then

$$T = \left(T_1 + \frac{\Delta H^0}{c_{P,g} - c_{P,s}}\right)\frac{Bi\cos\left(\xi x/L\right)}{Bi\cos\xi - \xi\sin\xi} - \frac{\Delta H^0}{c_{P,g} - c_{P,s}}, \text{ where } \xi^2 = \frac{\overline{m}\left(c_{P,g} - c_{P,s}\right)L^2}{k_{eff}} \qquad (2\text{-}30)$$

As noted in section 2.3.1.1, the temperature T should be kept between ~500-650K (or ΔT~150 K) to achieve favorable reaction kinetics (see Fig. 2-5). Equating this temperature difference to that from the solution in Eq. 2-31 yields an equation which was used to determine the steady heat transfer length scale.

$$L_{h,s}: \quad \Delta T = T(0) - T(L) = \left(T_1 + \frac{\Delta H^0}{c_{P,g} - c_{P,s}}\right)\frac{Bi\left(1 - \cos\xi\right)}{Bi\cos\xi - \xi\sin\xi} \qquad (2\text{-}31)$$

Because the reaction kinetics are very sensitive to temperature, it is useful to choose an optimal convective boundary temperature T_1 that maximizes the kinetics. Using the steady

temperature distribution (Eq. 2-30), the average reactor temperature is set to the optimal temperature for absorption (Eq. 2-10).

$$T_{opt} = \frac{1}{L}\int_0^L dx\, T = \left(T_1 + \frac{\Delta H^0}{c_{P,g} - c_{P,s}}\right)\frac{Bi}{Bi\xi\cot\xi - \xi^2} - \frac{\Delta H^0}{c_{P,g} - c_{P,s}} \qquad (2\text{-}32)$$

This results in a boundary temperature of

$$T_1 = \left(T_{opt} + \frac{\Delta H^0}{c_{P,g} - c_{P,s}}\right)\frac{Bi\xi\cot\xi - \xi^2}{Bi} - \frac{\Delta H^0}{c_{P,g} - c_{P,s}} \qquad (2\text{-}33)$$

We used Eq. 2-33 to eliminate the boundary temperature in Eq. 2-30 which yields the steady state heat transfer length independent of both the boundary temperature and the Biot number:

$$L_{h,s}: \quad \Delta T = \left(T_{opt} + \frac{\Delta H^0}{c_{P,g} - c_{P,s}}\right)\xi\frac{1 - \cos\xi}{\sin\xi} \qquad (2\text{-}34)$$

For MgH$_2$, we obtain $\Delta T/\left[T_{opt} + \Delta H^0/(c_{P,g} - c_{P,s})\right] \approx 0.0458$ (using ΔT=150 K), which results in $\xi \approx 0.302$. In general, for small values of ξ, $\xi(1 - \cos\xi)/\sin\xi \approx \xi^2/2$ (<5% error for ξ<0.771), and the steady length scale reduces to

$$L_{h,s} \approx \sqrt{\frac{2k_{eff}\Delta T / \overline{m}}{\left(c_{P,g} - c_{P,s}\right)T_{opt} + \Delta H^0}}$$ (2-35)

If $\left(c_{P,g} - c_{P,s}\right)T_{opt} = \Delta H^0$, Eq. 2-35 can be further simplified as shown below.

$$L_{h,s} \approx \sqrt{\frac{2k_{eff}\Delta T}{\overline{m}\Delta H^0}}$$ (2-36)

For MgH$_2$, we obtain $\left(c_{P,g} - c_{P,s}\right)T_{opt}/\Delta H^0 \sim 1/4$ and the result (Eq. 2-36) is a rough approximation given the approximation that yielded Eq. 2-36. So Eq. 2-36 is now independent of T_{opt}.

The convective boundary temperature estimate (Eq. 2-33) is also a useful quantity for use in hydrogen reactor simulations. When the change in internal energy of hydrogen from the gas to solid phase ($\approx \overline{m}\left(c_{P,g} - c_{P,s}\right)\Delta T$) is dominated by the conductive heat transfer ($\sim k_{eff}\Delta T/L$) the parameter ξ becomes small and further simplification is possible. Using $\xi\cot\xi \approx 1$ (<5% error for $\xi < 0.376$) resulted in an expression for the convective boundary temperature which is independent of the effective thermal conductivity.

$$T_1 \approx \left(T_{opt} + \frac{\Delta H^0}{c_{P,g} - c_{P,s}}\right)\left[1 - \frac{\overline{m}\left(c_{P,g} - c_{P,s}\right)L}{h}\right] - \frac{\Delta H^0}{c_{P,g} - c_{P,s}}$$ (2-37)

For $\overline{m}(c_{P,g} - c_{P,s})L/h = 1$, Eq. 2-37 reduces to the optimal temperature for reaction kinetics:

$T_1 \approx T_{opt}$. This situation occurs, for example, in MgH_2 with $h=4000$ W/m^2-K and $L=1$ cm.

2.3.2.3   Simulation

The governing equations for the hydrogen reactor are Eq. 2-11 and Eq. 2-22 and the solid phase mass conservation equation below.

$$(1-\varepsilon)\frac{\partial \rho_s}{\partial t} = \overline{m} \qquad (2-38)$$

The initial conditions are a uniform pressure P_0, temperature T_0, and solid density $\rho_{s,0}$. The same boundary conditions (Eq. 2-14 and Eq. 2-24) were used as before, with the boundary temperature defined by Eq. 2-33. The full set of nonlinear coupled partial differential equations was solved in MatLab® using the *pdepe* command. For the 500 nm particle size, the length was adjusted until 95% of the hydrogen was absorbed in 200 s (DOE 2010) in order to determine an allowable length scale L_{sim}. In order to compare results with the analysis of sections 2.3.2.1 and 2.3.2.2, the length scale was again obtained for infinite hydraulic permeability ($L_{h,sim}$) and infinite thermal conductivity ($L_{m,sim}$).

2.3.2.4   Physical Properties

The values for the parameters used in both the heat and mass transfer length scales and the simulation are given in Table 2-1. Particle size effects are introduced via the hydraulic

permeability and the thermal conductivity. For the permeability, the modified Carman-Kozeny equation was used [109].

$$K = K_D\left(1+1.15Kn\right);\ K_D = \frac{\varepsilon^3 d_p^2}{180(1-\varepsilon)^2},\ Kn = \frac{\Lambda_g}{\sqrt{K_D}},\ \Lambda_g = \frac{\mu}{P}\sqrt{\frac{\pi RT}{2M}} \qquad (2\text{-}39)$$

Here, the Knudsen number (Kn) is defined as the ratio between gas phase mean free path (Λ_g) and the Brinkman screening distance $\left(\sqrt{K_D}\right)$.

Table 2-1. Parameters used in the length scale analysis and simulation.

Property	Value
ε	0.5
P_0	1 bar
P_1	10 bar
T_0	450 K
$\rho_{s,0}$	1531 kg/m^{3†}
$\rho_{s,s}$	1658 kg/m^3
k_s	3.5 W/m-K‡
h	4000 W/m^2-K
$c_{P,g}$	14.89 kJ/kg-K
$c_{P,s}$	999 J/kg-K$^\&$
μ	1.41×10^{-5} kg/m-s
ΔH	-74.4 kJ/mol-H$_2$ [108]
ΔS	-133.5 J/(mol-H$_2$ K) [108]
C_a	9.57 s^{-1} [97]

† The densities $\rho_{s,0}$ and $\rho_{s,s}$ were taken to have the same average as that of Mg and MgH$_2$ (1590 kg/m^3), and also to reflect the proper mass change.
‡ The thermal conductivity of MgH$_2$ obtained from Ishido [111].
& The solid specific heat was approximated as the average between Mg and MgH$_2$, where the specific heat of MgH$_2$ (973 J/kg-K) was obtained from Wolf [113].

The effective thermal conductivity was modeled using an effective thermal conductivity model for packed beds [110].

$$\frac{k_{eff}}{k_{g,eff}} = \frac{1-\varepsilon}{k_{g,eff}/k_s + \phi}$$

(2-40)

The parameter ϕ is 0.09 for hydrogen with $\varepsilon = 0.5$ [110]. The gas phase effective thermal conductivity $k_{g,eff}$ is modified from the bulk value k_g to include the influence of the gas mean free path [111]:

$$\frac{k_g}{k_{g,eff}} = 1 + \frac{2\Lambda_g}{d_p}\left(\frac{2}{\gamma_a} - 1\right)$$

(2-41)

The energy accommodation coefficient γ_a is approximated to be 0.15 following the work of Ishido *et. al.* [111]. Size effects for the magnesium hydride thermal conductivity k_s are neglected because the estimated phonon mean free path[6] is too small (~5 nm) compared with the range of the particles sizes investigated (100 nm-100 μm).

---

[6] The phonon mean free path was estimated from the bulk thermal conductivity $k_s = \frac{1}{3}\rho_s c_{P,s} v_s \Lambda_s$, where the speed of sound v_s was approximated using results of a lattice dynamics simulation [27].

106

2.3.3 Results

The transient and steady length scales were graphed using Eq. 2-17, Eq. 2-24, and Eq. 2-27, and are shown in Fig. 2-7. Clearly, the transient length scales are irrelevant as they are significantly less restrictive than their steady counterparts. It is also clear that heat transfer is significantly more limiting than mass transfer for absorption kinetics, although when the particle size is below 1 μm, they are within one order of magnitude of each other.
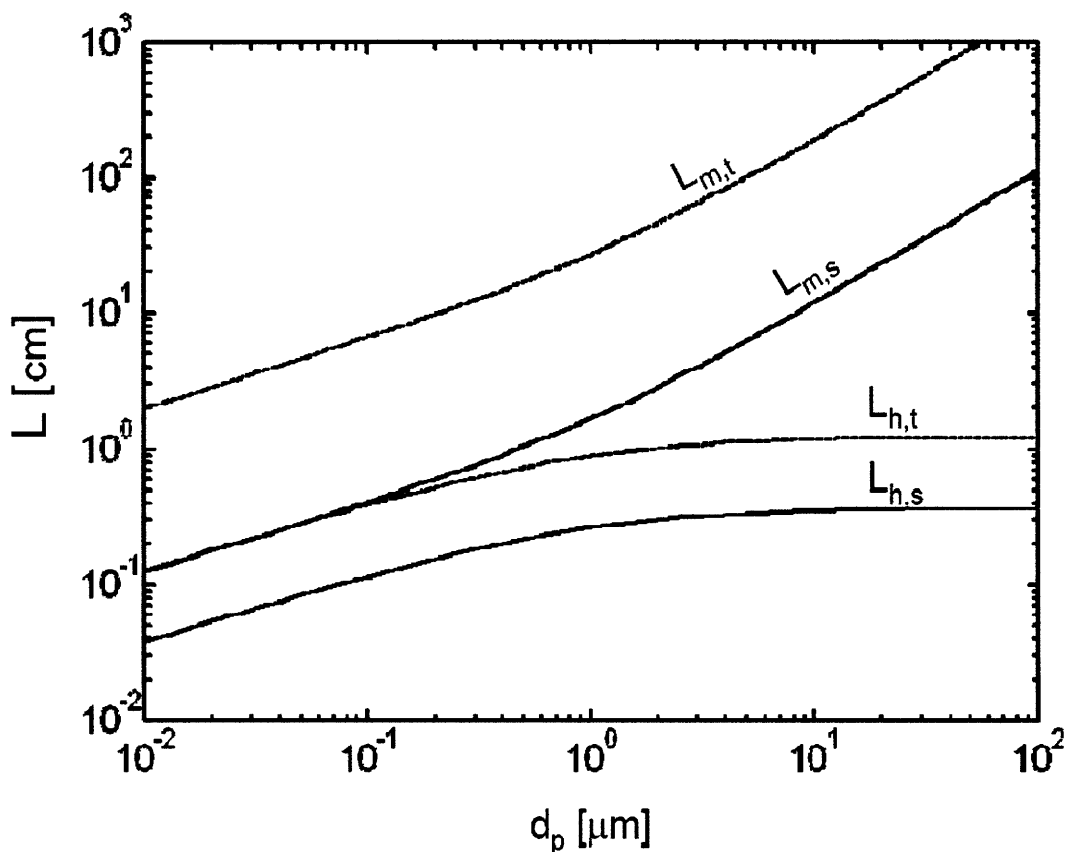
Figure 2-7. Steady ($L_{h,s}$) and transient ($L_{h,t}$) heat along with steady ($L_{m,s}$) and transient ($L_{m,t}$) mass transfer length scales, where the broken and solid lines correspond to transient and steady transport respectively. Overall, steady heat transfer (lower solid line) is rate limiting.

The effect of the heat transfer coefficient on the transient heat transfer scale is shown in Fig. 2-8. Here, Eq. 2-15 and Eq. 2-16 for variable heat transfer coefficients are plotted against Eq. 2-27 and the steady heat transfer scale (Eq. 2-35) is shown for comparison. Even for moderately low boundary heat transfer (h=100 W/m-K), the transient length scale remains higher than the steady length scale. The transient length scale begins to approach the infinite Biot number limit as h~4000 W/m-K, which demonstrates that very little improvement in heat transfer is possible at this state.
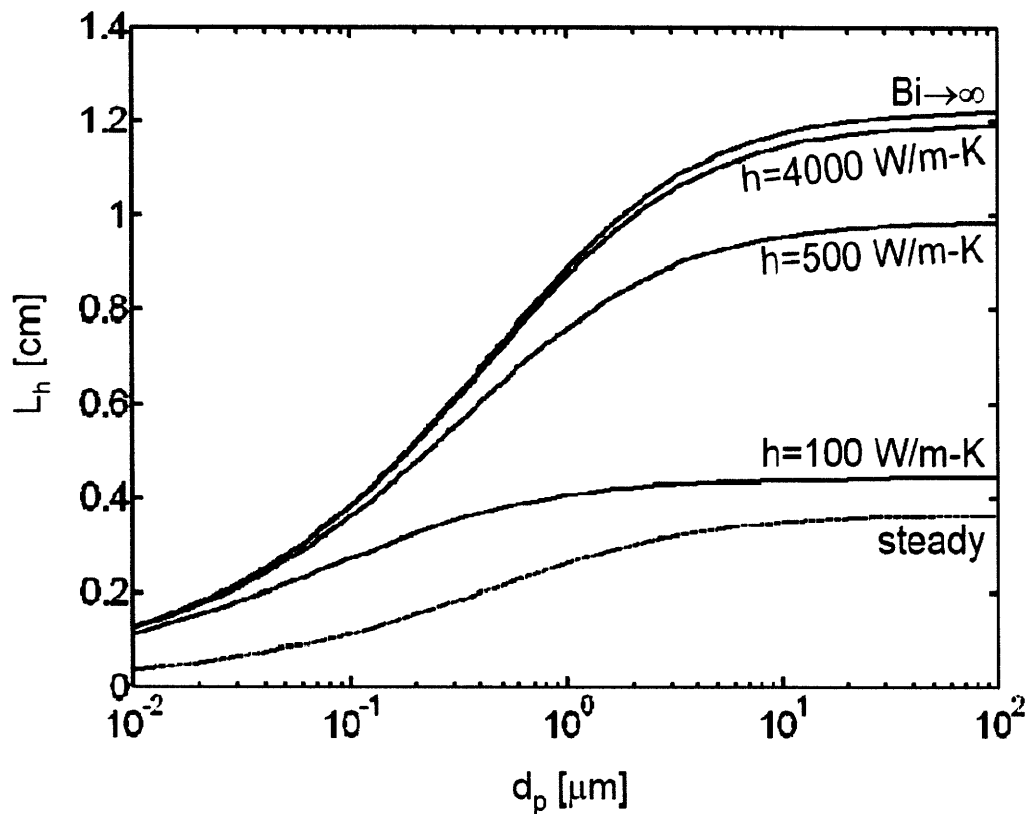
Figure 2-8. Transient heat transfer length scales for various values of the heat transfer coefficient. The solid lines are calculated for MgH_2 using the heat transfer coefficient indicated with the upper line representing the high Biot number limit. The length scale based on steady heat transfer (broken line) is shown for comparison.

The hydrogen reactor simulation for 500 nm particles gave the following results for length scales that just meet the 2010 goals for the hydrogen absorption rate: $L_{sim}=L_{h,sim}=3.5$ mm, and $L_{m,sim}=1.5$ cm. This verifies that the heat transfer is the kinetically limiting phenomena for 500 nm particles as was predicted by the scale analysis. The simulation results are plotted with the steady length scales in Fig. 2-9. The scale analysis seems to underpredict the allowable length scale, but otherwise shows good agreement.
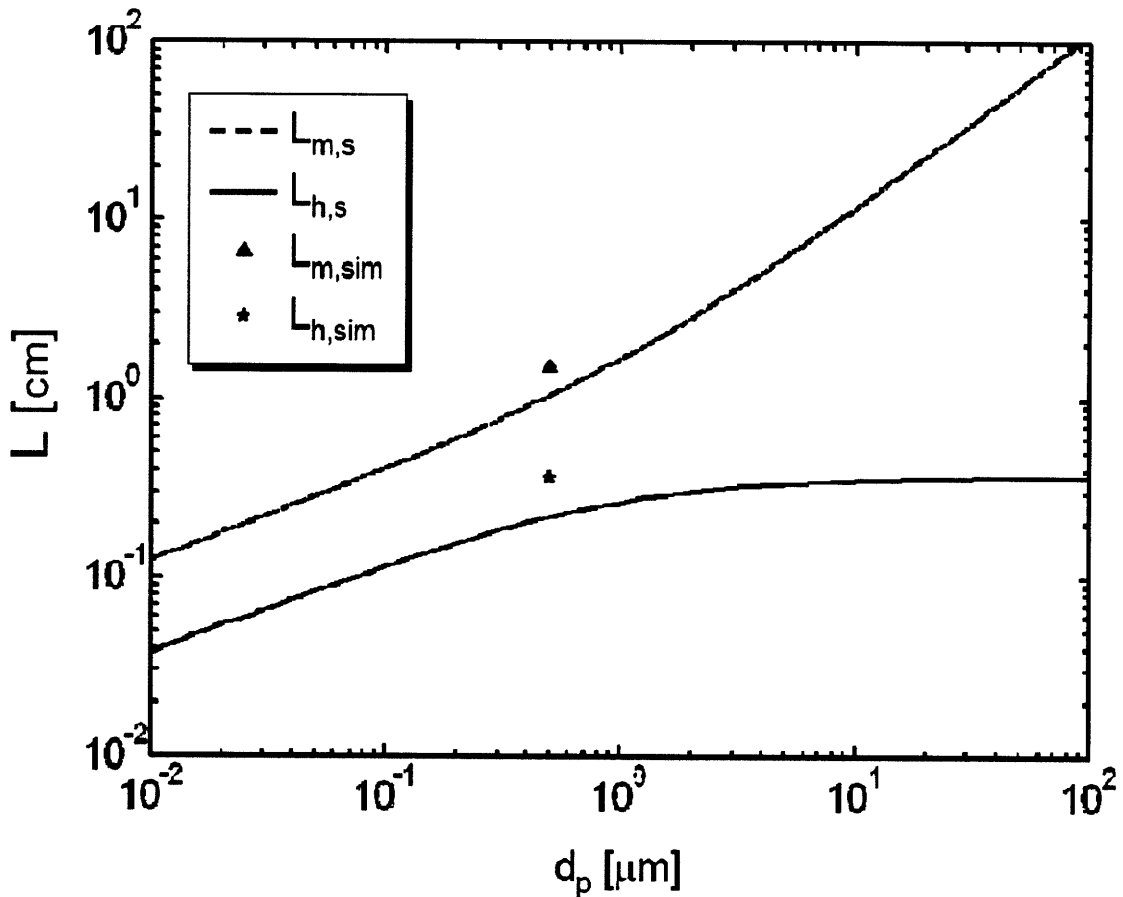
Figure 2-9. Simulation results compared to the approximate length scale analysis based on steady heat and mass transfer.

The temperature for the $L=3.5$ mm case is shown in Fig. 2-10. The rapid transient response is apparent, and a steady heat transfer regime is established for most of the absorption time. As the absorption rate (Eq. 2-8) slows due to $\rho_s \to \rho_{s,s}$, the heat rate released from the absorption reaction is reduced, which results in the average temperature dipping below the optimal temperature until the reaction is completed at $t=200$ s. The pressure response for this case is rather uninteresting as it remains at 10 bar for the entire simulation.
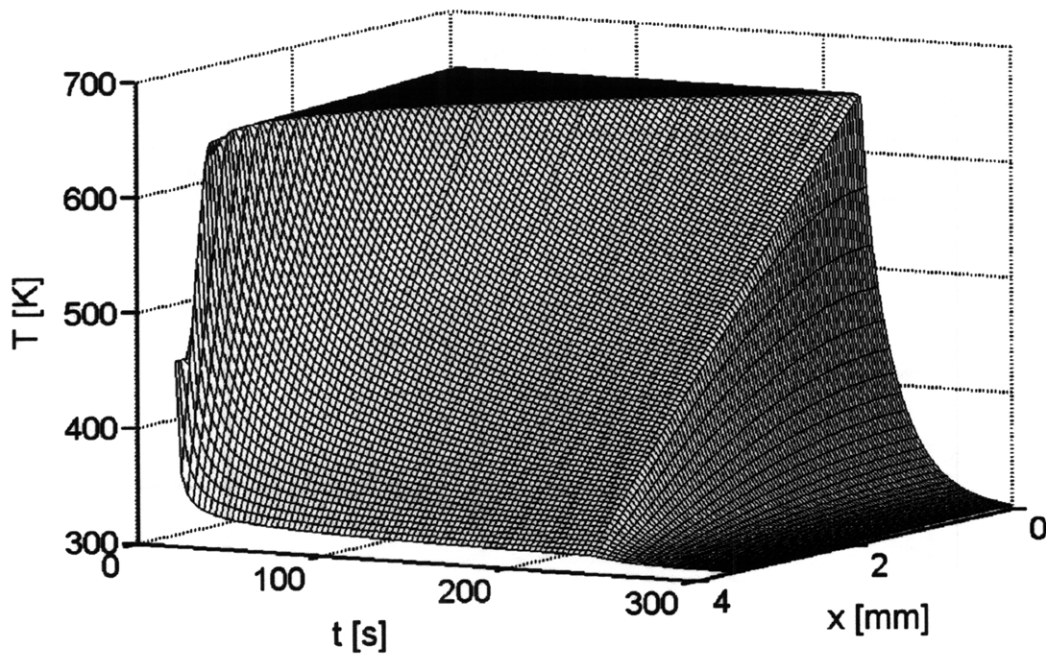
Figure 2-10. Hydrogen reactor simulation temperature response (heat transfer limited) shown as a 3D plot including time and distance coordinates.

For the case of infinite thermal conductivity with $L=1.5$ cm, the temperature remains isothermal for the entire simulation. Reduced mass transfer is the kinetically limiting process for this case, as is shown in the pressure response in Fig. 2-11. The wide region with a steady pressure distribution is apparent, which validates the assumptions leading up to Eq. 2-21.

The results in Fig. 2-9 are organized into a useful regime map as shown in Fig. 2-12. The vertical line showing the maximum particle size required for fast reaction kinetics is approximate, but certainly lies between 500 nm and 5 μm [10]. The steady heat (L_h) and mass (L_m) transfer length scales define the regimes where heat or both heat and mass transfer limit the overall absorption rate. Overall, heat transfer is more limiting than mass transfer. The regime with an absorption time that meets the DOE 2010 requirements is the white area at the bottom left corner of the diagram.
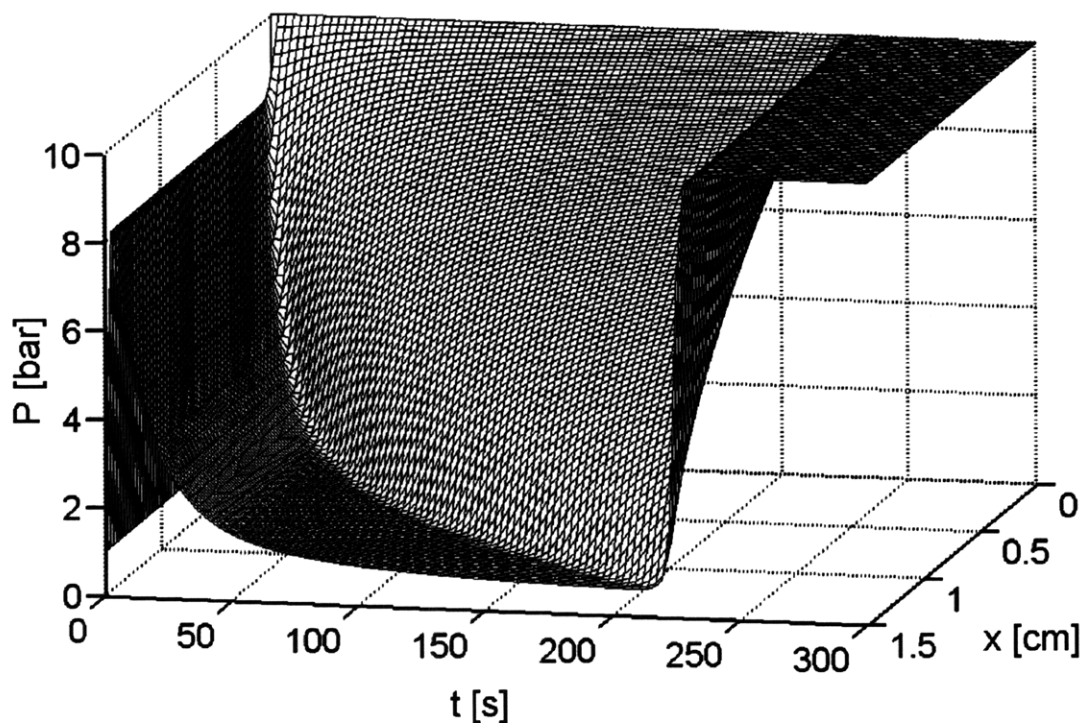
Figure 2-11. Hydrogen reactor simulation pressure response for infinite thermal conductivity (mass transfer limited) shown as a 3D plot including time and distance coordinates.
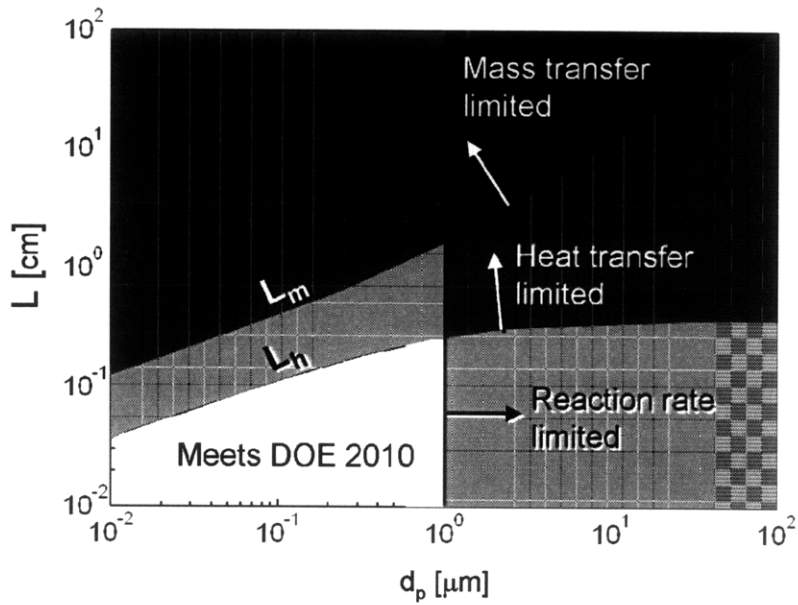
Figure 2-12. Regime map for MgH$_2$ (see text).

2.3.4 Conclusions

A simplified analysis of the heat and mass transfer in a hydrogen reactor was performed. The analysis was validated by achieving good agreement with a one-dimensional hydrogen reactor simulation. The simplified analysis based on steady transport processes predicts the lengths between hydrogen gas supply surfaces (L_m) and heat transfer augmentation surfaces (L_h) that meet the DOE 2010 targets. Rough approximations were derived (Eq. 2-21 and Eq. 2-36) and are repeated below.

$$L_m \approx P_1 \sqrt{\frac{MK}{\mu R \overline{T} \, \overline{m}}} \qquad (2\text{-}42)$$

112

$$L_h \approx \sqrt{\frac{2k_{eff}\Delta T}{\overline{m}\Delta H^0}} \qquad (2\text{-}43)$$

The convective boundary temperature (Eq. 2-37), a useful quantity for reactor simulations, was estimated to be independent of the effective thermal conductivity and is given by,

$$T_1 \approx \left(T_{opt} + \frac{\Delta H^0}{c_{P,g} - c_{P,s}}\right)\left[1 - \frac{\overline{m}\left(c_{P,g} - c_{P,s}\right)L}{h}\right] - \frac{\Delta H^0}{c_{P,g} - c_{P,s}} \qquad (2\text{-}44)$$

This simplified analysis is applicable to any hydride material (subject to the assumptions used), and is useful for hydrogen reactor design. Heat transfer enhancement through use of a porous metal or graphite compacts may also be included as long as the size effects are included in appropriate thermal conductivity and permeability models. For MgH_2, we determined that the hydrogen supply surfaces must be placed ~1 cm apart and heat transfer augmentation must be placed ~1 mm apart for the ~1 μm particle size necessary to meet the DOE 2010 absorption rate targets.

3 Impact of Excess Volume on the Enthalpy of Formation of Metal Hydrides

The strong chemical bonds that form between hydrogen and metals during chemisorption explain the high storage capacity of metal hydrides and their stability at room temperature, but these strong bonds are also responsible for the following engineering hurdles that must be addressed before hydrogen storage in metal hydrides can be practically used for on-board automotive applications [93]:

1. Slow diffusion of hydrogen in the hydride.

2. The high hydrogen release temperature, which must be brought down to a level closer to the waste heat temperature of the operating fuel cells.

3. Low storage efficiency, resulting from the wasted energy needed to overcome the high enthalpy of hydride formation and the elevated energy barriers to hydrogen release.

4. Inadequate heat transfer during the highly exothermic hydriding reaction to prevent high temperatures which may stall the hydriding reaction.

It has been shown in section 1.4 that reducing the enthalpy of formation of the metal hydride could positively impact the four bottlenecks mentioned above by reducing the energy barrier associated with the release of hydrogen [93]. The enthalpy of formation of most hydrides is negative since the hydriding reaction is exothermic. By reduction of the enthalpy of formation we refer to a reduction of the magnitude of the enthalpy which results in a destabilization of the hydride. In a destabilized metal hydride, the hydrogen forms a weaker bond with the host metal and the energy needed to extract the hydrogen is thus smaller. Nanotechnology offers new ways to reduce the enthalpy of formation of metal hydrides by taking advantage of the distinctive chemical and physical properties available in nanostructures [44, 46, 48]. Reducing the characteristic size of a material through mechanical treatments creates new structures and may lead to mechanical destabilization of the sample. In this chapter, we quantitatively examine the contribution to the reduction of the enthalpy of formation that arises from the generation of new nanostructures in ball milled materials. More precisely, we look at the impact of new surfaces, extra grain boundaries, metastable phases, and lattice deformations (see Fig. 3-1). We compare the predicted change in enthalpy reduction to experimental data obtained for different size distributions of MgH_2 particles. The results show that while the reaction kinetics can be increased by reducing the particle and grain sizes and by introducing metastable phases, lattice deformations, where excess volume is present need to be considered to account for the magnitude of the enthalpy reduction that has been observed in ball milled hydrides [114]. We investigate the impact of excess volume in deformed regions using three different equations of states (EOS). The results of those EOSs agree quantitatively with experiments and offer a plausible explanation for the observed reduction of the enthalpy of formation of certain metal hydrides.

115
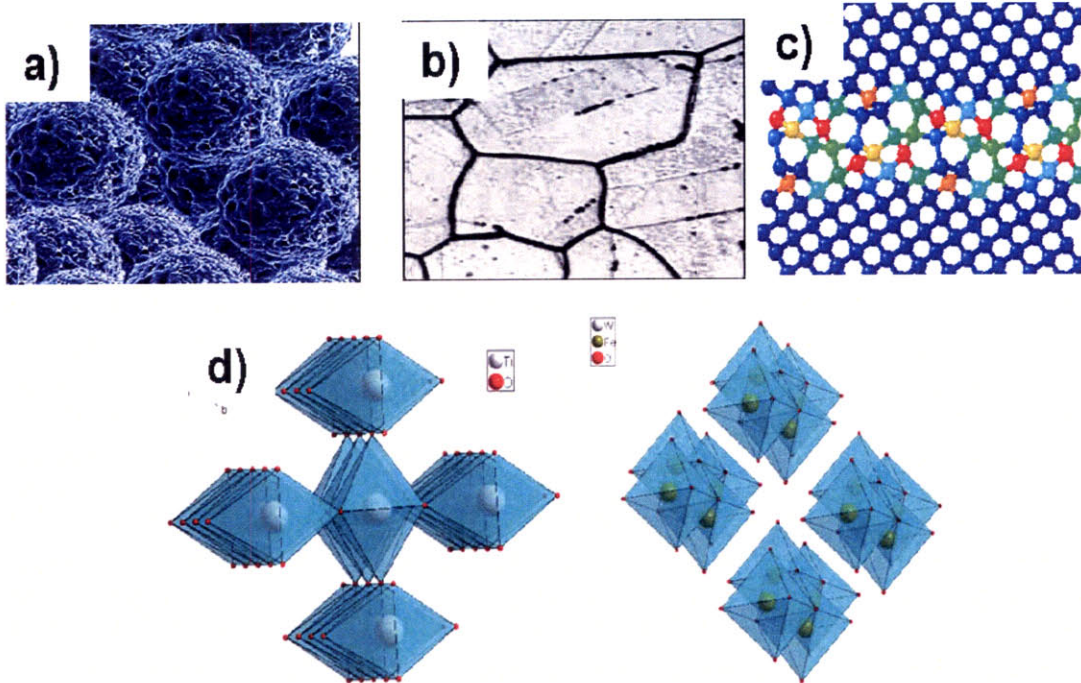
Figure 3-1. Extra a) surfaces b) grain boundaries c) deformed regions characterized by an excess volume and d) metastable phases that can play a role in reducing the enthalpy of formation in metal hydrides.

3.1 The Impact of Nanostructures on the Enthalpy of Formation

This section dicusses multiple mechanisms through which nanostructuring can affect the enthalpy of formation of metal hydrides.

3.1.1 Surface Area

A decreased particle size leads to an increased surface to volume ratio. Creating surfaces has an energy cost that will ultimately reduce the enthalpy of formation of the system if the surface energy of the hydrided phase is higher than that of the non-hydrided phase. Compared to the large enthalpy of formation for metal hydrides (75 kJ/mol for MgH_2, for example) [115], the surface energy of macroscopic sized particles is usually negligible. However, for particles of sufficiently small size, the surface energy term cannot be ignored, and the molar free energy of reaction may be reduced. For example, in the case of metal powders made from spherical nanoparticles of radius r, the free energy of formation becomes:

$$\Delta G(r) = \Delta G_0(r) + RT \ln\left(\frac{A_{MgH_2}}{A_{Mg} P_{H_2}}\right) + \frac{3 \upsilon_{Mg} \Delta_{Mg \to MgH_2}(\gamma, r)}{r} \tag{3-1}$$

where the volume-adjusted surface energy difference $\Delta_{Mg \to MgH_2}$ is given by

$$\Delta_{Mg \to MgH_2}(\gamma, r) = \left[\gamma_{MgH_2}\left(\frac{\upsilon_{MgH_2}}{\upsilon_{Mg}}\right)^{2/3} - \gamma_{Mg} \right] \tag{3-2}$$

Here, υ_i denotes the molar volume of each phase that accommodates the 10-30% volume increase that is usually observed in metal hydrides upon hydriding, while γ is the surface energy of each phase, A_i is the activity coefficient of the phases (in atm), and P_{H_2} is the pressure of the hydrogen gas (in atm). The binding of H_2 at the surface of both the metal and the metal hydride will

reduce their surface energy by minimizing the excess energy arising from unsatisfied bonds of surface atoms. This surface energy reduction must be treated by an additional energy term ΔE_{ads} in Eq. 3-2 because the surface energy reduction might not be the same in both the metallic and the hydride phases.
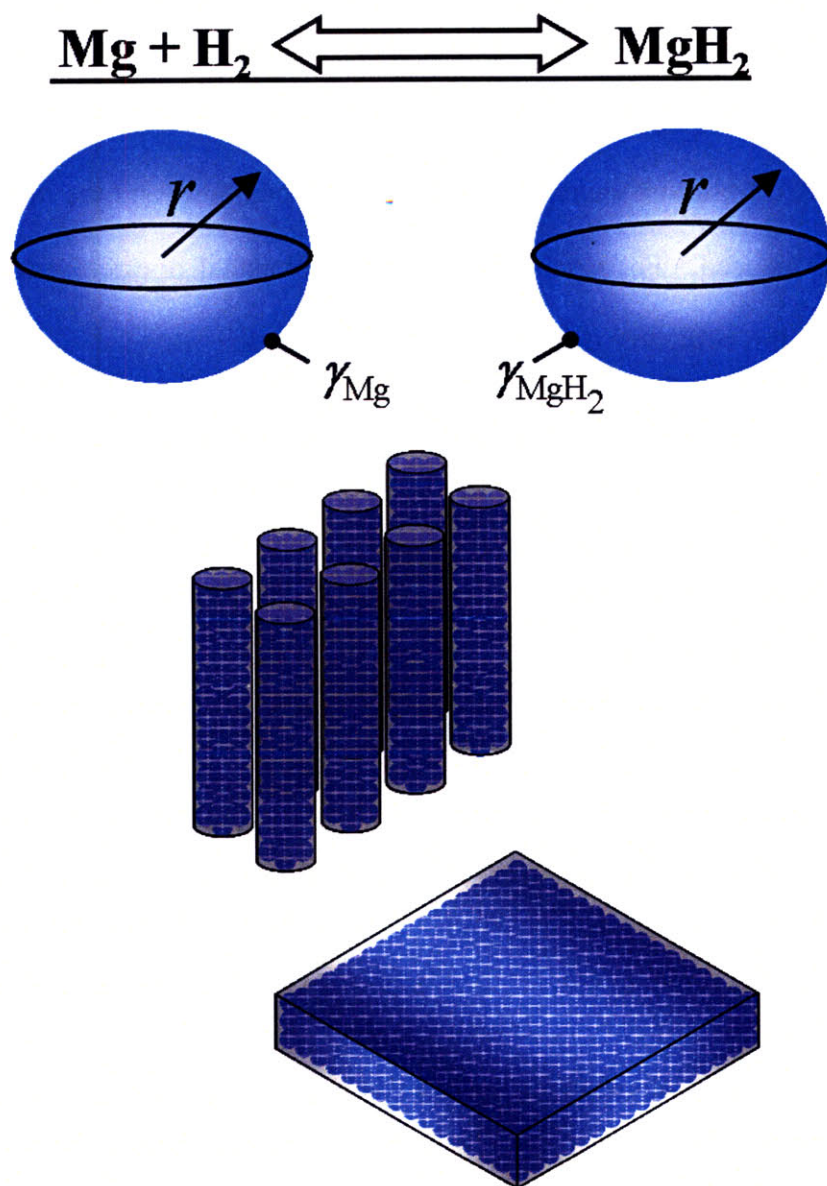
Figure 3-2. Example of nanostructures where surface area can play a role in reducing the enthalpy of formation.

Inclusion of the surface energy terms gives a new van't Hoff relation (Eq. 3-3 and Eq. 3-4), showing that size reduction lowers the enthalpy of hydride formation (ΔH) for the nanostructured hydride, as long as $\Delta_{Mg \to MgH_2}$ is positive.

$$\ln P_{H_2}^{eq} = \frac{\Delta H'}{RT} - \frac{\Delta S_0}{R} \tag{3-3}$$

$$\Delta H_{sphere} = \Delta H_0 + \frac{3 \upsilon_{Mg} \Delta_{Mg \to MgH_2}}{r} \tag{3-4}$$

Applying the same treatment to other types of nanostructures (see Fig. 3-2), we find the reduction in the enthalpy of formation that can be expected for a cylindrical or a slab-like nanostructures:

$$\Delta H_{Cylinder} = \Delta H_o + \overline{V_M} \Delta_{M \to MH} \left(\frac{2}{r} + \frac{1}{l} \right) \tag{3-5}$$

$$\Delta H_{Slab} = \Delta H_o + \overline{V_M} \Delta_{M \to MH} \left(\frac{1}{r} + \frac{4}{l} \right) \tag{3-6}$$

where l represents the length of the cylinder or that of the square slab, and r represents the radius of the cylinder and half the thickness of the slab (see Fig. 3-2).

Here, ΔH_0 is a negative quantity corresponding to the enthalpy of formation of the crystalline hydride at standard pressure and temperature. As seen in Eq. 3-2, $\Delta_{Mg \to MgH_2}$ will be positive if

119

the surface tension of the hydride is larger than that of the metal, since a volume expansion usually accompanies the hydriding reaction. A smaller magnitude for ΔH means that MgH_2 nanoparticles will be destabilized with respect to bulk MgH_2. The hydriding reaction would be less exothermic in that case, and the extraction of hydrogen out of the Mg host would become easier in the nanoparticles compared to the bulk phase. To estimate the contribution to the enthalpy of formation coming from the surface energy, we use a surface energy of 0.55 J/m^2 for Mg [88] and 2.08 J/m^2 for MgH_2 [116]. Here $\Delta_{Mg \rightarrow MgH_2}$ also depends on the molar volume of the metal and hydride phases. Taking into account a 34% volume increase upon hydriding [30] and the maximum surface energy difference between Mg and MgH_2, then the maximum value obtained for $\Delta_{Mg \rightarrow MgH_2}$ is roughly 2 J/m^2. Using this value in Eq. 3-4 predicts that the magnitude of ΔH could be 20% smaller than that of ΔH_0 for hydride particles with radii smaller than 5 nm (see Fig. 3-3). Figure 3-3 shows the predicted enthalpy of formation of MgH_2 as a function of radius for different nanostructures. Equation 3-1 and Eq. 3-4 will change depending on the geometry of the nanostructure. The maximum reduction in ΔH is seen for nanoparticles for which the surface to volume ratio is larger than the surface to volume ratio of the other nanostructures presented in Fig. 3-3. In Fig. 3-3, the enthalpy of formation predicted from looking at the surface energy does not take into account surface reconstruction or any adhesion between the Mg and MgH_2 nanoparticles, and for the slab geometry, the radius is defined as half the thickness.
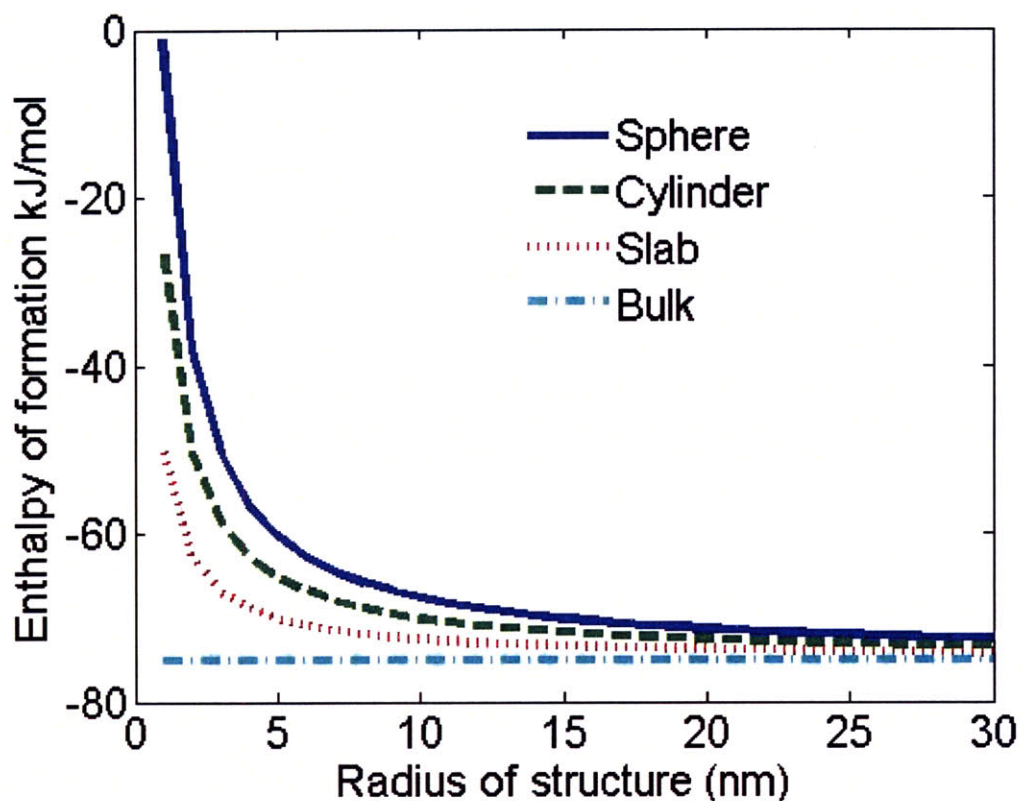
Figure 3-3. Enthalpy of formation of MgH$_2$ at 0K for different nanostructures.

Nevertheless, it would be difficult to implement this size-dependent effect for Mg nanoparticles because of the limitation on the nanoparticle size that can be achieved. Calculations based on the repulsive energy between dislocations predict that a minimum particle radius size of 15 nm is achievable through ball milling for Mg. At this particle size, the reduction in the enthalpy of formation predicted by Eq. 3-4 would only represent a 2-3% reduction in the enthalpy of formation of the hydride. In addition to that, van der Waals forces between the nanoparticles at small radii would create adhesion and surface reconstruction effects that would reduce the effective surface area of the particles [88]. As shown in Fig. 3-4, van der

Waals forces between nanoparticles in contact will create bridges of radius b between the particles (see Fig. 3-4) [9]

$$b \approx \left(46.9 \frac{r^2 \gamma}{B_o} \right)^{1/3}$$

(3-7)

where γ is the surface energy, r is the nanoparticle radius, and B_o is the bulk modulus of the material. Taking into account the adhesion forces and assuming that the nanoparticles are stacked in a hexagonal compact structure where each nanoparticle has 12 nearest neighbors, we can calculate the maximum reduction of the enthalpy in a powder made of spherical nanoparticles. This value can be compared to the results for free standing nanoparticles (Fig. 3-4 and Fig. 3-5). At very small radii, the van der Waals forces between the nanoparticles are strong enough to induce a surface reconstruction that reduces the effective surface area of the particles [88]. The fraction of the surface area lost to this mechanism becomes increasingly large in the region for which the size effects could substantially reduce the enthalpy of formation. This effect offsets the positive impact of reducing the particle size on the thermodynamics of the hydriding/dehydriding transformation by reducing the effective surface-to-volume ratio of the nanopowder compared to free standing particles. The new results, which incorporate the surface area reduction, show that the surface energy effects will not impact the enthalpy of formation by much if the nanostructures are in contact (see Fig. 3-5). These results suggest that size alone cannot account for the reduction of the enthalpy of formation observed experimentally in reference [114]. Moreover, first principles calculations by Wagemans *et al.* [30] have shown that for free standing MgH_2 clusters, the nanoparticles lose their crystalline structure for small

radii and that surface reconstruction takes place. The reconstruction increases the stability of the nanoparticles such that a significant enthalpy reduction only occurs for particles smaller than 2 nm. A 2 nm particle is beyond the smallest size achievable through ball milling. This means that the additional surface energy created in powders made of nanoparticles cannot explain the observed reduction of the enthalpy of formation that is found in some experiments (above 20% for MgH_2 in [114]). Therefore other mechanisms must be responsible for the large magnitude of the observed enthalpy reduction. The results by Wagemans also demonstrate the limitations of using a macroscopic description of surface energy effects to describe particles of such a small size where size-effects become dominant.
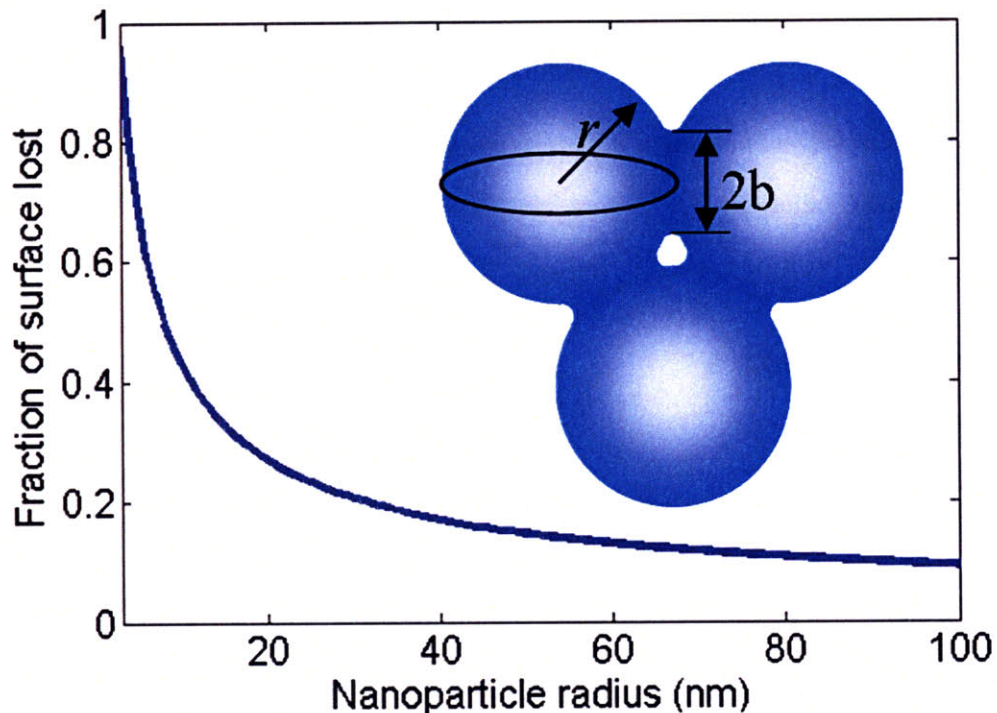
Figure 3-4. Fraction of the surface area lost as a function of the particle radius due to the van der Waals forces between the nanoparticles.
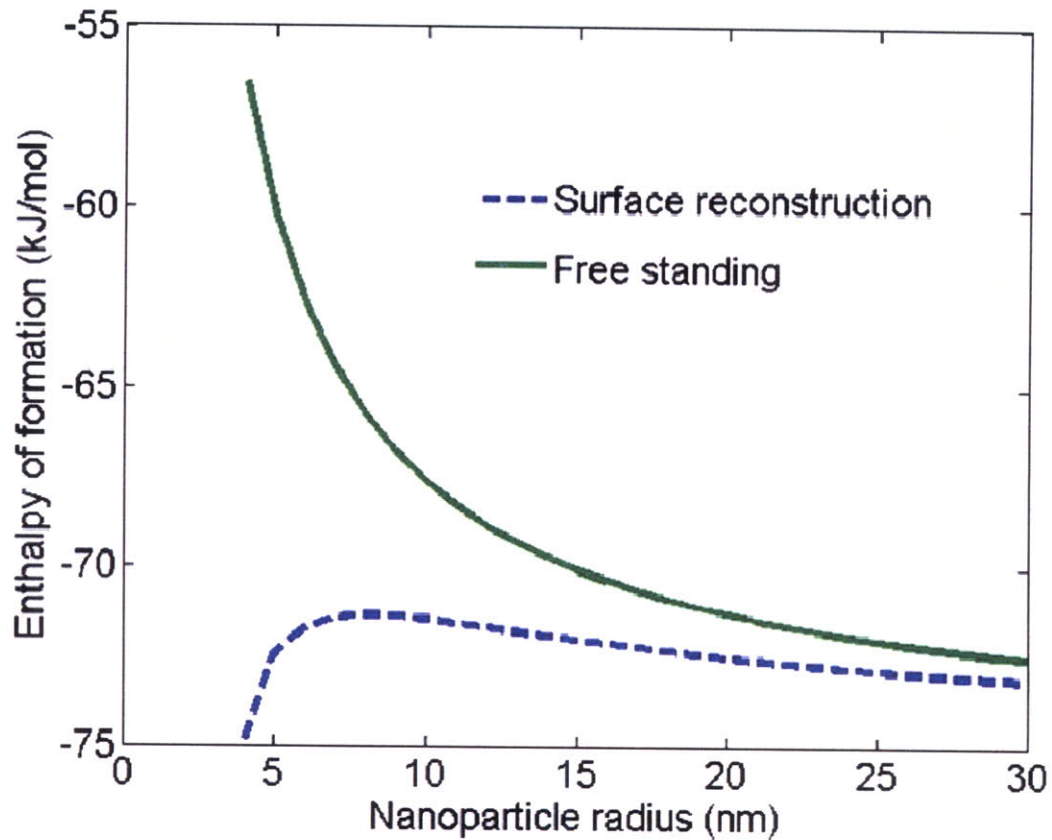
Figure 3-5. Enthalpy of formation of a MgH₂ powder made of nanoparticles as a function of the nanoparticle radius.

3.1.2 Grain Boundaries

High-energy mechanical treatments like ball milling also reduce the grain size of polycrystalline materials and introduce many grain boundaries. These grain boundaries are the result of mismatched crystal plane orientations and give rise to excess energy that in turn lead to excess enthalpy. As in the case of the nanoparticles, the exact grain boundary energy will depend on the crystal plane orientation on the two sides of the boundaries as well as on the exact grain size distribution in the sample. We can simplify this problem since we are interested in

estimating the maximum contribution to the enthalpy of formation that arises from a reduction in the grain size. To calculate the maximum excess enthalpy, we use an approach similar to that found in Eq. 3-1 through Eq. 3-4 and treat every grain boundary as two separate surfaces of two separate particles. Each grain thus becomes equivalent to a particle with a size equal to the grain size. A simple estimate of the maximum energy value of the equivalent surfaces can be obtained by equating the grain boundary energy difference between the metal and the metal hydride to the maximum surface energy difference between the two phases, as was done in the previous section. This naturally overestimates the contribution to the enthalpy of formation since a grain boundary has a lower energy than the two surfaces creating it, due to the binding between the two planes. But the estimate thus made still provides an order of magnitude approximation for the enthalpy of formation change attributable to grain boundaries. As in Section 3.1, we use a volume adjusted surface energy difference of 2 J/m^2 in our calculations. To convert the grain boundary energy difference between Mg and MgH_2 to a reduction of the molar enthalpy of formation when grain size is reduced, we assume that all MgH_2 grains are spherical and have the smallest grain size present in the sample (7-9 nm for the samples we consider in the relevant experimental study [114]) since the exact grain size distribution is generally not available. Our calculations for MgH_2 shows a maximum reduction in the enthalpy of formation of only approximately 9-10 kJ/mol (~12%) for a grain size of the order of 7-9 nm [114] (see section 3.2). While nonnegligible, this high estimate cannot account for all of the 24% reduction of the enthalpy of formation observed in [114] (see section 3.2).

3.1.3 Presence of a Metastable Phase

Another possible explanation for the reduction of enthalpy of formation in heavily ball milled materials is the presence of a metastable phase in the metal hydride produced by the high-energy mechanical treatment. For example, MgH_2 possesses multiple high pressure phases whose enthalpy of formation differs from its stable phase at standard temperature and pressure [117]. MgH_2 crystallizes with the TiO_2 rutile-type (β-MgH_2) structure at ambient pressure and low temperature. At higher temperatures and pressures (0.39GPa at 0K), β-MgH_2 transforms into orthorhombic γ-MgH_2 [117] and at even higher pressure, orthorhombic γ-MgH_2 turns into the δ-MgH_2 with a modified CaF_2 structure. Even if the δ-MgH_2 can be generated during heavy mechanical treatments, its elevated transition pressure (3.84GPa at 0K) makes it very unstable and it is rarely found in MgH_2 samples [118]. When generated during ball milling, the δ-MgH_2 usually relaxes into γ-MgH_2 which is metastable at ambient pressure and has often been observed in ball milled samples by neutron diffraction and other methods [31, 118].

In [117], Vajeeston et al. used VASP to calculate the unit-cell volume versus total-energy relations for MgH_2 for 11 different actual and possible structural arrangements. Figure 3-6 is adapted from Vajeeston's results and shows the relative molar energy (ratio of the energy to the equilibrium energy under standard conditions of pressure and temperature) of MgH_2 as a function of the relative molar volume (ratio of the volume to the equilibrium volume under standard T and P conditions) for the 3 phases of MgH_2 that are the most likely to be generated during ball milling. The first principles calculations [117] demonstrate that at standard temperature and pressure, the energy difference between the β-MgH_2 and γ-MgH_2 phases is less then 1% (<0.75kJ/mol) at ambient pressure (see Fig. 3-6). Thus the γ-MgH_2 could not play an

important role in reducing the enthalpy of formation, unless the external pressure becomes so high (>> 10 GPa) that the small difference in volume between the two phases leads to a large reduction of the enthalpy content of the γ-MgH$_2$ phase compared to the β-MgH$_2$ phase (the reduction comes from the PV term in the definition of the enthalpy: $H = E + PV$, where the pressure P corresponds to the pressure inside the solid that results from internal strain and stress). This approach to enthalpy reduction must however be disregarded in the present context, since such high pressures are impractical for hydrogen storage applications. As for the δ-phase, its contribution to reducing the enthalpy of formation could go up to almost 4 kJ/mol (see Fig. 3-6), but experiments show that the δ-phase is present in extremely small quantities due to its large instability and tendency to relax rapidly into more stable phases [118].
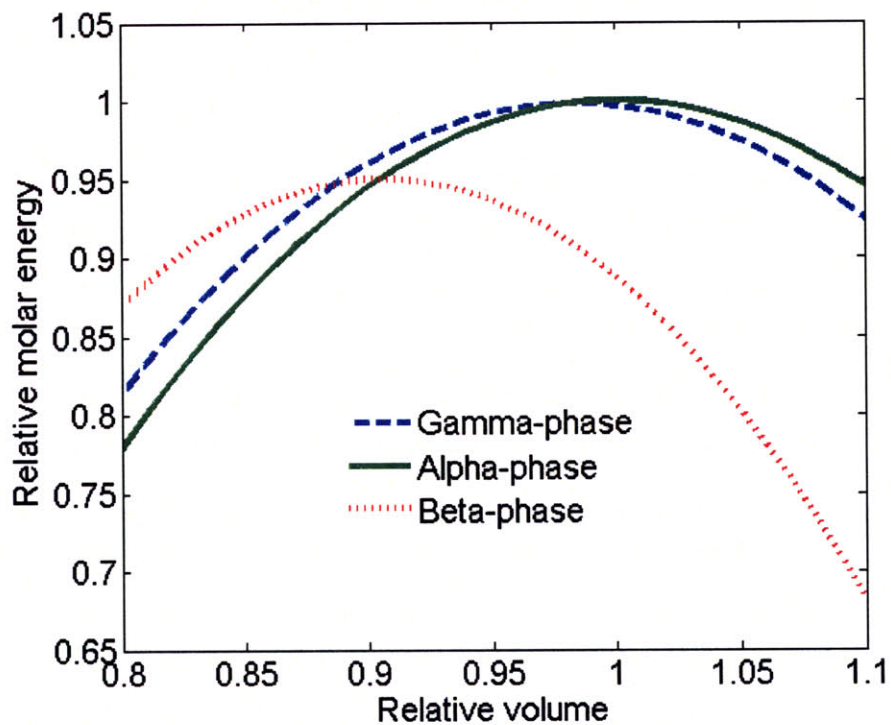
Figure 3-6. Relative molar energy of MgH$_2$ for different crystalline structures as a function of the relative volume. Adapted from [117].

It is worth mentioning, however, that experiments suggest that the interfaces between different metal hydride phases catalyze the hydrogen release reaction [114, 119]. In [114], experimental results indicate that the presence of γ-MgH$_2$ significantly reduces the release temperature of hydrogen. Such a catalytic interaction could offer new ways to improve the kinetics with respect to reversible hydrogen absorption/desorption cycles despite the fact that our modeling suggests that the γ-MgH$_2$ phase cannot significantly reduce the enthalpy of formation. Such considerations show that nanostructures could both benefit the thermodynamic properties of hydrogen storage materials and help speed up the slow kinetics that often characterizes materials with high storage capacity.

3.1.4 Excess Volume in Deformed Regions

The following section introduces the concept of excess volume as a way to explain the reduction of the enthalpy of formation of metal hydrides subject to intense mechanical treatments. The predictions of the model are presented for MgH$_2$ and TiH$_2$. The predictions for MgH$_2$ are also compared to experimental results.

3.1.4.1   Excess Internal Energy, Excess Enthalpy and Excess Volume

The surface energy, grain boundary energy, and metastable phase excess energy in nanostructured metal hydrides (sections 3.1.1-3.1.3) all favor a reduction of the enthalpy of formation, although their combined contribution, at least for MgH$_2$, is insufficient to explain the

experimental observations [114]. Another mechanism must therefore be responsible for the observed reduction in the enthalpy of formation of certain metal hydrides.

In addition to the presence of extra grain boundaries and extra surfaces, as well as the presence of metastable phases or isolated dislocations, it has been observed that materials subject to plastic deformations will show regions where defects such as dislocations and high angle grain boundaries accumulate around a crystalline grain [22, 120]. Those regions differ significantly from a crystalline region in terms of their density and of their physical properties. The resulting lattice distortions will change the energy content of the metal and hydride states and therefore could explain the enthalpy of formation change, as discussed below.

Characterizing the physical properties of these deformed regions can be quite challenging if one does not know their exact structure and concentration. Consequently, it becomes more convenient to describe the properties of deformed regions containing several types of defects in term of an effective excess volume than to treat each defect separately. The excess volume is thus a simple way to describe the elongation of the atomic bonds occurring in materials subject to plastic deformations as was introduced in [34, 35]. It must be emphasized that a large material sample is unlikely to be described by a single value of excess volume but rather by a distribution of numerous regions characterized by different excess volume values.

The excess volume V_{ex} is related to the ratio of the molar volume of the material in its current state of temperature and pressure compared to the molar volume that the material would have at equilibrium for that temperature T and at zero pressure [121]:

$$V_{ex} = \frac{\upsilon}{\upsilon_o(T, P = 0)} - 1 = V_R - 1 \qquad (3\text{-}8)$$

where v is the molar volume of the sample and $v_o(T, P=0)$ is the equilibrium molar volume at temperature T and zero pressure, and V_R is the relative volume. The excess volume thus takes into account the thermal expansion of the solid, since v_o will increase with T which will be of importance for temperature dependent calculations (chapters 4 and 5). In our mathematical model, we use the relative volume instead of the excess volume for mathematical simplicity in the EOS.

This type of deformation changes the energetic properties of materials and is related to the amount of work that must be done to displace the atoms out of their equilibrium positions. This work is stored in the solid as an excess energy and excess enthalpy, which will lead to an excess entropy contribution for nonzero temperature. By excess molar enthalpy and excess molar internal energy, we refer to the difference between the internal molar energy or molar enthalpy content of a material and the internal energy and enthalpy content of its crystalline state taken at a reference temperature $T = T_o$ and pressure $P = 0$. The excess internal energy and enthalpy arise from the presence of high energy defects or deformations. For example, in the case of the excess molar internal energy:

$$E_{ex}(T,v) = E(T,v)\big|_{\text{with defects and deformations}} - E(T_o,v_o)\big|_{\text{perfect crystal}} \tag{3-9}$$

It is shown in this section that the excess volume in deformed regions that develops as a result of the ball milling, or similar energetic mechanical treatments, can account for the large enthalpy changes observed experimentally [114]. In our discussion below, three different equations of state (EOS) are used to predict the enthalpy change that can be expected for a given excess volume. There are numerous EOSs that have been developed to describe different types

of solids [122]. Our choice of the universal EOS as well as the 2nd and 3rd order Birch-Murnaghan (BM) EOSs was motivated by their ease of use, as well as their good predictive power for different types of solids ranging from metals to insulators [34, 35, 122, 123, 124]. Though differences are observed between the three EOSs, all indicate that the excess volume formation is the mechanism that can explain the experimental observation of reference [114].

3.1.4.2   Universal EOS

A simple yet accurate way to explain the effect of lattice distortions on the energy of the crystal is by formulating an equation of state that relates the energy of the crystal to its actual volume relative to the equilibrium volume. A dimensionless excess volume V_{ex} in deformed regions of metallic nanoparticles due to their longer atomic bonds was demonstrated to also result in an excess energy, which can be related to a negative hydrostatic pressure [34, 35]. According to the universal equation of state developed by Rose and his coworkers [34], the internal energy of a solid under expansion or compression can be written as:

$$E(V_{ex}) = E_o \cdot E(a) = E_o \cdot (-1 - a - 0.05a^3)\exp(-a)$$
(3-10)

with the dimensionless parameter a defined in terms of the relative volume V_R by:

$$a = \frac{\left(\dfrac{3v_o}{4\pi N_A}\right)^{1/3}\left[(V_R)^{1/3} - 1\right]}{\bar{l}}$$
(3-11)

131

In the above equations, E_o is the molar energy content of the material at equilibrium (P=0, T=0), N_A is the Avogadro number, $\bar{l}$ is a length scale characteristic of each material and $\bar{l}$ depends on the electrical screening of the outer electronic shells, B_0 is the bulk modulus, and v_o is the equilibrium molar volume.

From this equation of state (Eq. 3-10), the enthalpy of the region characterized by an excess volume can be obtained from the usual thermodynamic relation:

$$H(V_R) = E(V_R) + \left| P(V_R) \right| v_o V_R \tag{3-12}$$

with the pressure given by:

$$P(V_R) = -\frac{\partial E}{\partial V}\bigg|_S = \frac{3B_0 \left[\left(V_R \right)^{1/3} - 1 \right]}{\left(V_R \right)^{2/3}} \left(1 - 0.15a + 0.05a^2 \right) \exp(-a) \tag{3-13}$$

In Eq. 3-12 we take the absolute value of the pressure to account for the fact that even for a negative hydrostatic pressure as well as for a positive one, the enthalpy content of the material will be increased (in the same way that the potential energy of a spring is increased both in tension and compression). Equation 3-12 is of special importance since it will allow us to calculate the excess enthalpy present in a deformed solid for the three different EOSs considered in this section. Equation 3-12 predicts that all solids will see their enthalpy content increase by the presence of excess volume. Therefore, the excess enthalpy associated with the excess volume in both the metal and the metal hydride will result in a reduction of the enthalpy of formation (reduction of the heat released) during hydrogenation only if the non-hydrogenated

phase has a smaller enthalpy increase for a given excess volume. This can be understood from the fact that the enthalpy of formation is the difference between the enthalpy of the metal hydride and the enthalpy of both the metal and the hydrogen gas taken together. On the other hand, if the enthalpy content of the metal is increased more than that of the metal hydride, then the difference between the two enthalpies will be increased instead of being reduced, and it would become even harder to extract the hydrogen from the host metal. By combining Eq. 3-10 through Eq. 3-13, we can derive the condition for which the enthalpy of formation of a metal hydride will be reduced. Assuming that a small excess volume ($V_{ex} \approx 0$) is present in both the metal hydride and the metal phases, we can show that the hydride phase (*MH*) will be destabilized with respect to the metal (*M*) if

$$\eta = \left[v_o B_o \right]_{MH} - \left[v_o B_o \right]_M \geq 0 \ \text{ for } V_R \approx 1 \ \Rightarrow \ (a \approx 0) \tag{3-14}$$

In Eq. 3-14, η gives a measure of the degree of destabilization of a hydride with respect to its metallic phase (a metal hydride is said to be destabilized with respect to its metallic phase if the energy difference between the two actual states is smaller than the energy difference between the two standard states). A large positive η is favorable for hydrogen storage applications since it means that the enthalpy of formation between the two phases is reduced by the introduction of excess volume. A negative η, however, indicates that the presence of highly deformed regions in the sample should be avoided for hydrogen storage applications because it renders the metal hydride phase more stable with respect to the metal phase.

To better illustrate the origin of Eq. 3-14, it is convenient to think of a quadratic solid (Eq. 3-15) in which the excess energy due to the excess volume is proportional to the product of the

bulk modulus and the molar volume times the square of the volume increase (just like a 3D

harmonic oscillator where the Hook's constant is the bulk modulus). Equation 3-15 shows that

for a given excess volume V_{ex} (V_R - 1), the excess energy present in a quadratic solid is directly

proportional to $v_o B_o$.   For small excess volume, it is reasonable to assume that the energy

dependence on volume of the metal and the metal hydride follows the quadratic potential given

by Eq. 3-15. Under that condition, we find that the energy difference between the metal hydride

and the metal will be reduced if the product of the bulk modulus and the molar volume of the

metal hydride is larger than the same product for the metal phase. This condition for a reduced

energy of formation corresponds exactly to the destabilization criteria given by Eq. 3-14:

$$E(V_R) - E_o = \frac{v_o B_o (V_R - 1)^2}{2} \qquad (3\text{-}15)$$

3.1.4.3   Second and Third Order Birch-Murnaghan EOSs

The 2nd order Birch-Murnaghan (BM) equation of state [123] can also explain how the excess

volume deformation can lead to a reduction of the enthalpy of formation. According to the 2nd

order BM EOS, at 0K, the energy and the hydrostatic pressure of a solid characterized by an

excess volume are given by

$$E(V_R) = E_o + \frac{v_o B_o V_R}{B'} \left(\frac{(1/V_R)^{B'}}{B'-1} + 1 \right) - \frac{B_o v_o}{B'-1} \qquad (3\text{-}16)$$

$$P(V_R) = \frac{B_o}{B'} \left(\left(\frac{1}{V_R} \right)^{B'} - 1 \right) \qquad (3\text{-}17)$$

Then, following Eq. 3-12, the enthalpy for a material with excess volume at zero temperature is given by

$$H(V_R) = E_o + \frac{v_o B_o}{B'} \left(2V_R - V_R^{1-B'} + \frac{V_R^{1-B'} - B'}{B'-1} \right) \qquad (3\text{-}18)$$

where E_o is the equilibrium molar energy, and B' is the derivative of the bulk modulus with respect to pressure evaluated at zero pressure and temperature ($B' = (\partial B / \partial P)_{T=0, P=0}$). As in the case of the universal EOS (Eq. 3-10), we can investigate the conditions under which the hydride will be destabilized with respect to the metal by the introduction of excess volume using Eq. 3-18. From this investigation we show that destabilization will occur if the excess enthalpy of formation due to the excess volume is positive ($\delta \Delta H(V_{ex}) > 0$):

$$\delta \Delta H(V_R) = \left[\frac{v_o B_o}{B'} \left(2V_R - V_R^{1-B'} + \frac{V_R^{1-B'} - B'}{B'-1} \right) \right]_{MgH_2}$$
$$- \left[\frac{v_o B_o}{B'} \left(2V_R - V_R^{1-B'} + \frac{V_R^{1-B'} - B'}{B'-1} \right) \right]_{Mg} \qquad (3\text{-}19)$$

For a bulk modulus that is independent of pressure ($B'=0$), the condition for instability $\delta \Delta H(V_{ex}) \geq 0$ is equivalent to what we obtained for Eq. 3-14 :

$$\eta = [\upsilon_o B_o]_{MgH_2} - [\upsilon_o B_o]_{Mg} \geq 0 \text{ for } V_R \approx 1 \tag{3-20}$$

However, for non-zero B' the condition for destabilization becomes:

$$\eta' = \left[\upsilon_o B_o \frac{B'-2}{B'-1}\right]_{MgH_2} - \left[\upsilon_o B_o \frac{B'-2}{B'-1}\right]_{Mg} \geq 0 \text{ for } V_R \approx 1 \text{ and } B' \neq 1 \tag{3-21}$$

Because most substances have a B' value close to 5 from the work of Bastide *et al.*[118], we see that the conditions given by Eq. 3-14 and Eq. 3-20 will tend to predict the same general results for the destabilization of metal hydrides at low excess volume. The 2nd order BM EOS is easy to use and provides an intuitive explanation for the destabilization of a material where excess volume is present. The 2nd order BM EOS, however, does not predict a Gibbs instability for high excess volume. The Gibbs instability in a solid corresponds to an excess volume for which the bulk modulus turns negative (B=0). A negative bulk modulus leads to an instability in which every subsequent increase of volume further reduces the Gibbs free energy of the solid, so that the solid cannot maintain its integrity and crumbles. Noting that B =0 for the minimum of the P(V) function ($B = -V(\partial P / \partial V)_T$) we can see that the monotonic decline of pressure with excess volume predicted by the 2nd order BM EOS will not predict such an instability (see Fig. 3-7).
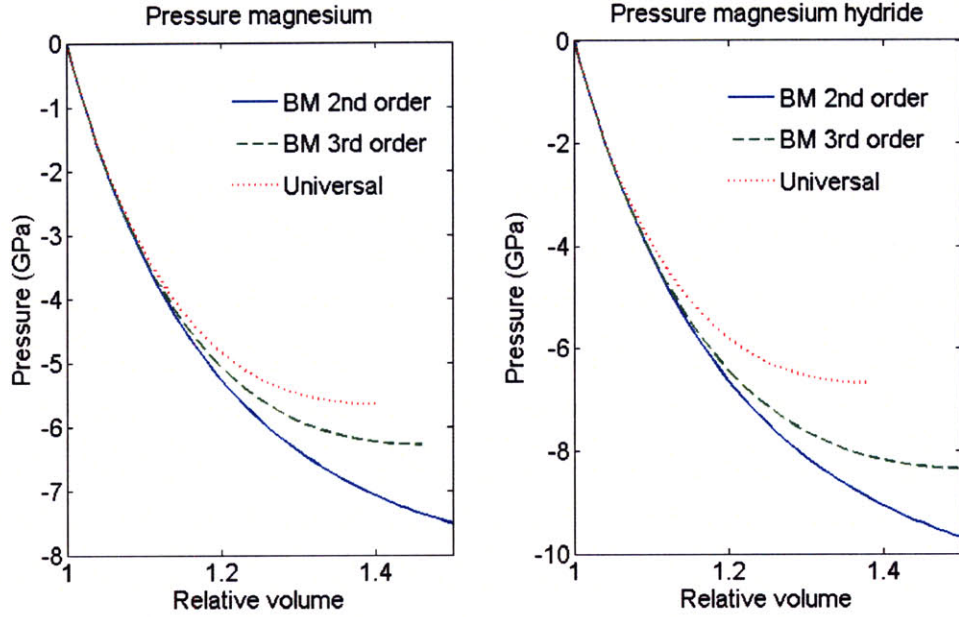
Figure 3-7. Negative hydrostatic pressure in Mg (left) and MgH$_2$ (right) corresponding to a material under tension.

This failure of the 2nd order BM EOS to predict a region of instability is unphysical, but can be remedied by using the 3rd order BM EOS. The prediction of the Gibbs instability is an important feature of the 3rd order BM EOS because it tells us what the maximum excess volume sustainable for the solid is and thus what is the maximum destabilization that can be obtained by deforming the metal hydride. The 3rd order BM EOS is written as [124]:

$$E(V_R) = E_o + \frac{9v_o B_o}{16}\left(\left[V_R^{-2/3} - 1\right]^3 B' + \left[V_R^{-2/3} - 1\right]^2\left[6 - 4V_R^{-2/3}\right]\right) \qquad (3\text{-}22)$$

Again, the enthalpy can be obtained from Eq. 3-12 where the pressure is given by the following equation:

$$P(V) = \frac{3B_o}{2}\left[V_R^{-7/3} - V_R^{-5/3}\right]\left[1 + \frac{3}{4}(B_o' - 4)\left[V_R^{-2/3} - 1\right]\right] \qquad (3\text{-}23)$$

Figure 3-7 shows the negative hydrostatic pressure in Mg (left) and MgH_2 (right) corresponding to a material under tension. For the 3rd order BM and the universal EOS, the curves stop at the pressure/relative volume corresponding to the Gibbs instability where the bulk modulus becomes negative. A negative Bulk modulus corresponds to a region where the slope of the P(V) curve is positive. Such an instability is not predicted by the 2nd order BM EOS, which is unphysical because it corresponds to a solid whose atomic bonds can be stretched continuously without the formation of cracks or the evaporation of the solid into a gas.

3.2 Excess Volume in Magnesium and Titanium Hydrides

Using the three EOSs defined in Sections 3.1.4.2 and 3.1.4.3, we can calculate the impact of excess volume on the energy and enthalpy of formation of well known hydrides: MgH_2 and TiH_2. Figure 3-8 and Fig. 3-9 show a comparison between the three EOSs for MgH_2 and TiH_2. For both graphs, the energy and enthalpy of formation are predicted as a function of the relative volume until the Gibbs instability is reached. Figure 3-8 shows the predicted energy (left) and enthalpy (right) of formation of MgH_2 as a function of the relative volume according to the universal EOS (Eq. 3-10) and the Birch-Murnaghan 2nd and 3rd order EOS (Eq. 3-16 and Eq. 3-

138

22). All three EOSs show that the hydrided phase can be substantially destabilized with respect to Mg. For large V_{ex}, the enthalpy of formation can become positive, which represents an endothermic hydriding reaction. For small V_{ex} up to 0.2, all three EOSs are in good agreement and predict a reduction of the enthalpy of formation (resulting from excess volume effects), whose magnitude is large enough to explain the experimental data of reference [114] (see Section 3.3).
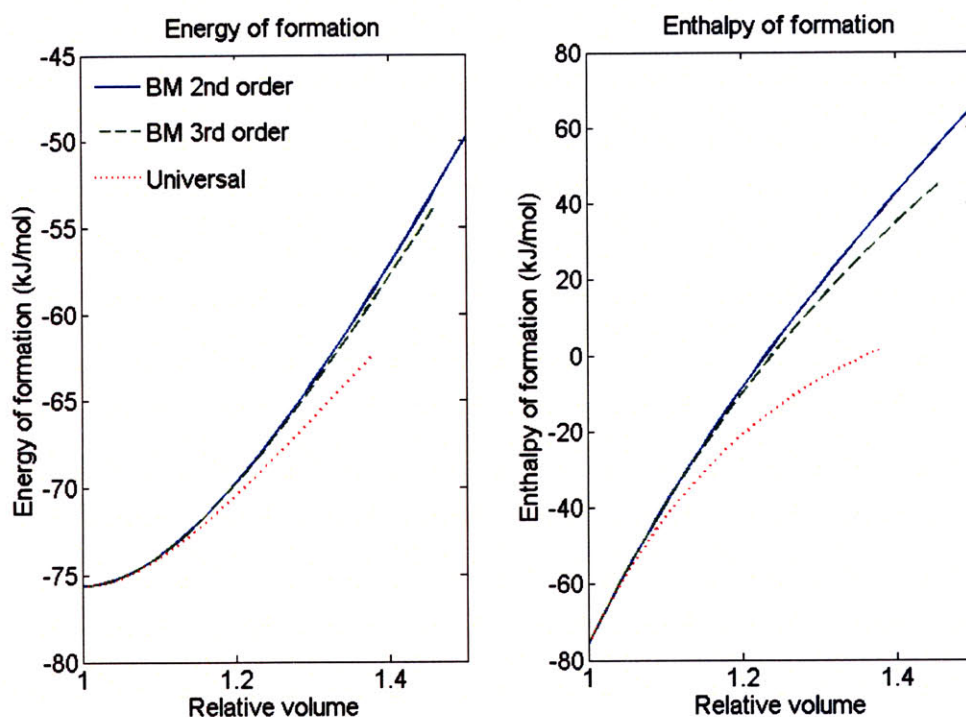
Figure 3-8. Predicted energy (left) and enthalpy (right) of formation of MgH$_2$ as a function of the relative volume.

Figure 3-9 shows the predicted energy (left) and enthalpy (right) of formation of TiH$_2$ as a function of the relative volume. For Ti/TiH$_2$, excess volume leads to an increase of the enthalpy of formation when such excess volume regions are introduced. The Ti hydriding reaction illustrates the fact that not all materials will benefit from the introduction of high energy

structural defects (Eq. 3-14). In the case of Ti, the bulk modulus of the hydrided phase (74GPa) is substantially smaller than that of titanium alone (106GPa) and Eq. 3-14 correctly predicts that the enthalpy of formation will be increased by the introduction of excess volume (η = -2270 for Ti/TiH$_2$ compared to 805 for Mg/MgH$_2$). For Ti, the hydride phase is less destabilized than the metal alone, which leads to an increase in the enthalpy of formation upon introduction of deformed regions. A simple argument is thus capable of predicting which materials are favored by the presence of excess volume, namely that MgH$_2$ is favored and that TiH$_2$ is not favored.
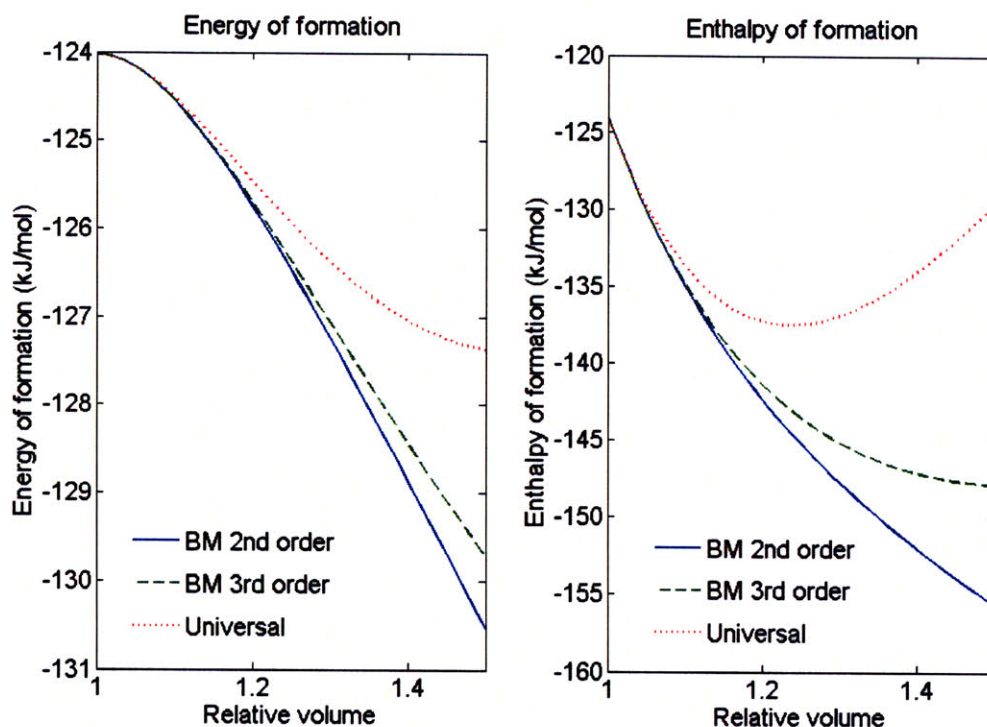
Figure 3-9. Predicted energy (left) and enthalpy (right) of formation of TiH$_2$ from Ti + H$_2$ as a function of the relative volume.

A difference in the value of the excess volume will have a dramatic influence on the enthalpy of formation of the destabilized hydride. It is also likely that as a result of a high

140

energy mechanical treatment, only a fraction of the sample would be deformed and be in a state of excess volume while the rest of the sample would remain in a crystalline state (for example, if 20% of the sample is in a state of excess volume, the excess volume fraction is 0.2). The fraction of the sample that is in a state of excess volume also has an important effect on the enthalpy reduction. The excess volume and the excess volume fraction will vary from sample to sample, even within distinct regions in the same sample. Figure 3-10 plots the relative molar enthalpy of formation of MgH_2 (ratio of the enthalpy to the equilibrium enthalpy under standard conditions) as a function of the relative volume and the fraction of the solid that is in a state of excess volume (denoted in the legend as a fraction). The change in enthalpy is calculated from the universal EOS (Eq. 3-10).

In a milled sample, there would most likely be a distribution of excess volume regions, each associated with an excess volume fraction. To calculate the exact contribution of the excess volume to reducing the enthalpy of formation, one would need to integrate over the distribution of excess volume regions in the sample. It is not a trivial matter to obtain such a distribution of excess volume experimentally. Precise structural characterization of hydride samples in which enthalpy reductions have been observed are currently not available, but it would be necessary to fit the theoretical models and to determine if crystal deformations can be responsible for the reduction in the enthalpy of formation that is observed experimentally. Because of this lack of experimental data, we assumed for simplicity that a material can be described by a unique excess volume over a known fraction of the sample (Fig. 3-10). This assumption helps us determine in Section 4 the magnitude of the destabilization that can be achieved by introducing an excess volume.

141
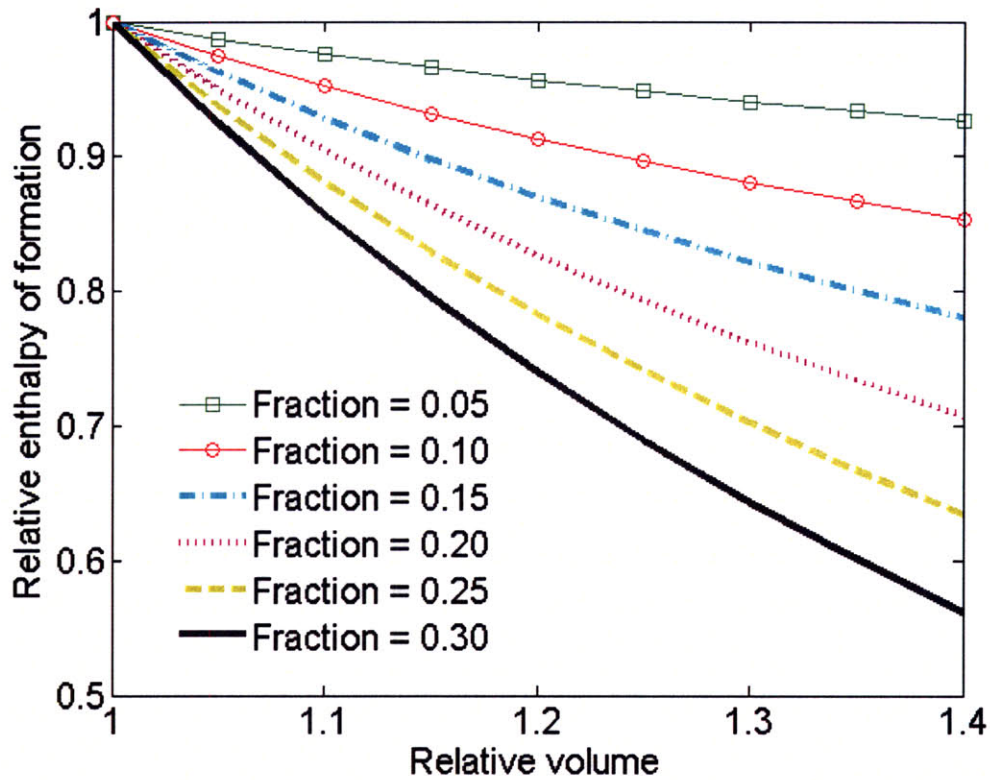
Figure 3-10. Relative molar enthalpy of formation of MgH_2 as a function of the relative volume and the fraction of the solid that is in a state of excess volume.

3.3 Discussion

The purpose of this section is to identify which nanostructures could explain the reduction of the enthalpy of formation that is sometimes measured in metal hydrides subjected to high energy mechanical treatment. Figure 3-11 compares the reduction of the enthalpy of formation in MgH_2 predicted by the four mechanisms presented in this paper with the experimental data obtained by Varin [114] (denoted by black lines). Each column represents a different size distribution of nanoparticles obtained by high energy ball milling (see [114] for more details on the exact

process used to produce the particles). Sample 1, 2, and 3, respectively, have mean particle radii of 393 nm, 374 nm, and 338 nm. Because no data were available on the explicit excess/relative volume that was present in the samples, we chose the dimensionless excess volume V_{ex} of 0.2 to be present over ~ 1% to 14% of the sample to reproduce the experimental results. Figure 3-11 shows the relative importance of the four different nanostructures that we introduced in Section 3.1 and how their combined effect can reproduce experimental results [114]. The surface and grain energy contributions were calculated using the method outlined in Sections 3.1.1 and 3.1.2 in conjunction with the experimental data provided by [114] on the particle and grain size distributions. The maximum contribution from metastable phases was obtained by assuming that the whole sample was in the lowest energy state of the metastable γ-MgH_2 phase as given in Fig. 3--6 which corresponds to a difference of less than 1 J/mol for the enthalpy of formation. It is clear from the data that even if of importance, the presence of surfaces, grain boundaries, and of metastable phases is not enough to predict the observed enthalpy of formation, but that the introduction of deformed regions with excess enthalpy can in fact explain the experimental observations. Figure 3.11 also illustrates that the presence of other phases as well as surface and grain boundary effects do not reduce the enthalpy sufficiently and that an excess volume effect is needed to explain the observed reduction in the enthalpy of formation. The potential impact of the excess volume on the enthalpy of formation is such that its impact can be one order of magnitude larger than the combined effects of surfaces and other phases and of the same order of magnitude as the grain boundary contribution. Since the fraction and extent of the excess volume in the deformed regions are not directly related to the particle and grain size distribution, the theory also explains why the reduction of the enthalpy of formation in certain samples is independent of the particle and grain size distributions. The particle and grain size are a function

of the type of mechanical treatment used to create the hydride powder and one can expect the

excess volume fraction and the magnitude of the excess volume to depend on the characteristics

of the mechanical treatment used [114]. Finally one should mention that the experimental results

were obtained at room temperature while the EOS model predicts the impact of the excess

volume at 0K. As we will see in the next chapter, this difference only plays a minor role and the

does not change the results mentioned above.
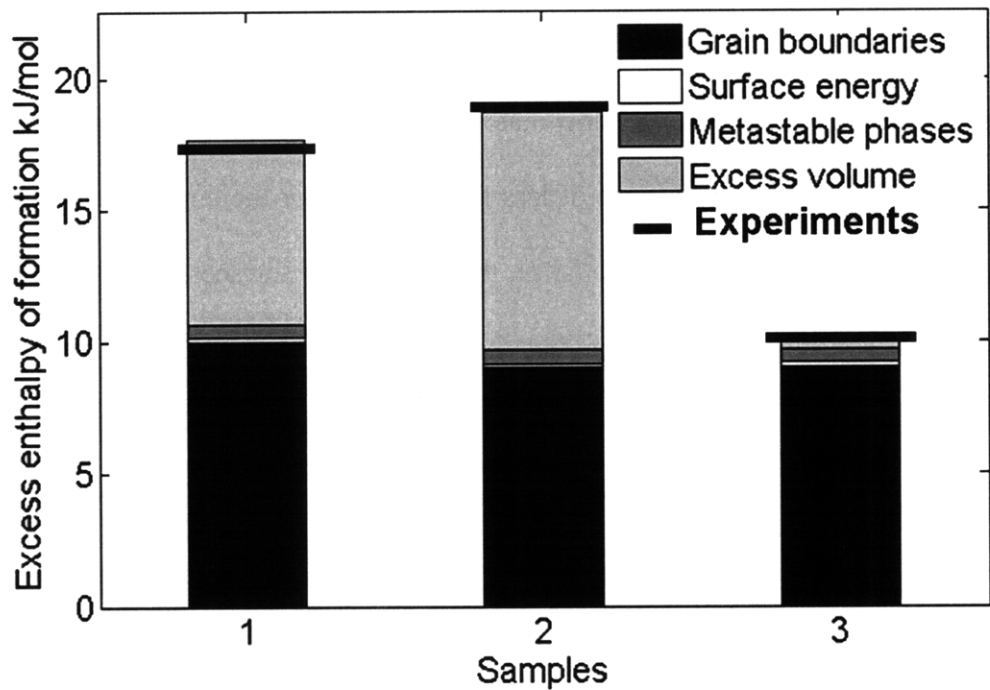
Figure 3-11. Comparison of the reduction of the enthalpy of formation in MgH$_2$ predicted

by the four mechanisms presented in this chapter with the experimental data obtained by

Varin [114].

A large reduction of the enthalpy of formation can dramatically improve the storage

properties of hydrogen in metal hydrides and it is thus important to understand which treatment

can maximize the reduction of the enthalpy by generating the desired structural changes in the

hydrides. This point is even more important, since we showed that not all nanostructures will favor a reduction of the enthalpy of formation, and that heavy mechanical treatments could also result in an increase of the enthalpy of formation in some materials. It is thus important to better understand the exact structural impacts of reducing metals to nanopowders to be able to tailor the mechanical treatments to our needs instead of simply milling the materials to yield a given size distribution.

It must be emphasized that even if a reduction of the particle and grain size as well as the presence of metastable phases cannot fully account for the observed reduction of the enthalpy of formation of metal hydrides, those structures can still play an important role in speeding up the kinetics and reducing the hydrogen release temperature [125]. For example, smaller grain and particle sizes can favor the diffusion of hydrogen in the material which speeds up the kinetics by limiting the slow diffusion through the hydride layer that forms around the larger particles during the hydriding reaction. In addition, the presence of metastable phases can play a catalytic role in releasing the hydrogen as in the case of the γ-MgH_2 phase in MgH_2 which is known to reduce the hydrogen release temperature. Reducing the enthalpy of formation of metal hydrides is only one of the goals associated with improving the properties of metal hydrides for hydrogen storage, and structures that do not favor its reduction should still be considered and studied. It has also been reported that while good for kinetics, the introduction of strain, surfaces and grain boundaries during mechanical treatments can have an adverse impact on the storage capacity of metal hydrides [126]. This emphasizes the tradeoffs that must be considered when improving metal hydrides for hydrogen storage through nanostructuring.

Deformed regions also show an increase in their specific heat. For example, 20% to 50% increases in specific heat have been measured for nanocrystalline Cr [22]. The phenomenon

associated with the increase in specific heat would also help to manage the temperature rise during the hydriding reaction by absorbing some of the heat released during the hydriding reaction into vibrational energy in the atomic bonds at the boundary.

The presence of excess volume can improve the properties of certain metal hydrides but as in the case of other nanostructures, it is likely that the excess volume regions will relax to their more stable crystalline state over multiple high temperature hydriding/dehydriding cycles [127]. Stabilizing those metastable excess volume regions is not a trivial task but excess entropy at high temperature could offer a way to do so. This will be discussed in chapter 5 after we discuss the high temperature properties of deformed regions in chapter 4.

3.4 Summary

Metal hydrides possess high storage capacity but there remain many issues that must be addressed before these materials can be used for hydrogen storage in automotive applications. These are:

1. Slow sorption kinetics

2. High hydrogen release temperature

3. Low storage efficiency

4. Thermal management

Reducing the enthalpy of formation through the introduction of nanostructures is a strategy to address these issues because it reduces the energy barrier for hydrogen release. Reducing this barrier, in turn, reduces the temperature needed for hydrogen extraction, which indirectly addresses the other bottlenecks mentioned above. The introduction of surfaces, grain boundaries as well as the presence of γ-MgH_2 can lead to a reduction of the enthalpy of formation of up to 15%, but cannot explain the experimental observations where reductions of more then 20% have been observed [114]. Only when considering the presence of deformed regions with excess volume were we able to reproduce the experimental data. For materials such as magnesium hydride, the calculations show that the enthalpy of formation can be reduced by up to 24% by only introducing a 20% (V_{ex}=0.20) excess volume over 15% of the material in addition to the effect of surface and grain boundary energies as well as the presence of other phases. Even if the presence of excess volume could ultimately reduce the gravimetric capacity of the hydrides by changing the energy distribution of the hydrogen binding sites, the gain in efficiency, thermal management, and kinetics would far outweigh this loss in gravimetric capacity for automotive applications. The above results were derived for 0K but a generalization of these thermodynamic relations to any temperature and pressure is presented in chapter 4.

4 Temperature Dependence of the Enthalpy of Formation of Metal Hydrides Characterized by an Excess Volume

In chapter 3, it was shown that reducing the enthalpy of formation of metal hydrides would increase storage capabilities in three ways: improving its energy efficiency by reducing the energy loss associated with the large heat release during the hydriding reaction, reducing the hydrogen gas release temperature, and improving the desorption kinetics by reducing the energy barrier for hydrogen release [121]. The exact mechanisms behind the reduction of the enthalpy of formation are not clear although we showed in chapter 3 that reducing the particle size, reducing the grain size, introducing metastable phases, and generating deformed regions that can be characterized by an excess volume could play an important role [121]. While the first three factors can play a role in reducing the enthalpy of formation, modeling suggests that deformed regions characterized by an excess volume provided the only mechanism which could reduce the enthalpy of formation sufficiently to reproduce the experimental observations [93, 121]. It must be emphasized that even if a reduction of the particle and grain size as well as the presence of metastable phases cannot fully account for the observed reduction of the enthalpy of formation

of metal hydrides, those structures can play an important role in speeding up the kinetics and reducing the hydrogen release temperature [121]. For example, smaller grain and particle sizes can favor the diffusion of hydrogen in the material which speeds up the kinetics by limiting the slow diffusion through the hydride layer that forms around the larger particles during the hydriding reaction. In addition, the presence of metastable phases can play a catalytic role in releasing the hydrogen as in the case of the γ-MgH_2 phase in MgH_2 which is known to reduce the hydrogen release temperature. Reducing the enthalpy of formation of metal hydrides is only one of the goals associated with improving the properties of metal hydrides for hydrogen storage, and structures that do not favor its reduction should still be considered and studied. It has also been reported that while good for kinetics, the introduction of strain, surfaces and grain boundaries during mechanical treatments can have an adverse impact on the storage capacity of metal hydrides [93]. This emphasizes the tradeoffs that must be considered when improving metal hydrides for hydrogen storage through nanostructuring [121].

In addition to having a model that describes the thermodynamic properties at 0K or room temperature [93], understanding the temperature dependence of the thermodynamic properties of metal hydrides is of crucial importance because the hydrogen release usually takes place at a temperature much higher than room temperature [119, 127, 128]. Since deformed regions characterized by an excess volume can be the main contributor to a reduction of the enthalpy of formation in metal hydrides, it is important to understand how the thermodynamic properties of deformed regions will be affected by the elevated temperatures needed for the hydrogen release [121]. In this chapter, a high temperature generalization of our findings in chapter 3 on the thermodynamic properties of deformed regions produced by the ball milling of metal hydrides is established. In particular, at these elevated temperatures, the energetic properties of deformed

149

regions may not favor the hydrogen release even if their room temperature or zero temperature properties behave favorably. As temperature is increased, the enthalpy content of the metal and the metal hydride change due to contributions from the heat capacity, the work associated with the thermal expansion, the increased entropy, and the temperature dependence of the hydrostatic pressure inside the solid. The different temperature dependences of the enthalpy content of the deformed regions in the metal and the metal hydride will determine how the enthalpy of formation is dependent on temperature.

This chapter first shows that the enthalpy of formation of metal hydrides at elevated temperature can be predicted using a temperature dependent equation of state (EOS) for the solid phases and the ideal gas law for the hydrogen gas at high temperature. Simple relations are obtained that can predict the behavior of metal hydrides using only the bulk modulus, the first derivative of the bulk modulus with respect to pressure, and the thermal expansion coefficient at a reference temperature as input parameters. The relative importance of the different contributions to the temperature dependence of the enthalpy of formation is calculated in the case of the Mg/MgH_2 system.

4.1 The Temperature Dependent Universal EOS

Equations of state are widely used in the literature to describe the relation between different thermodynamic variables in a simple and computationally manageable way [122]. There are a wide variety of EOSs that have different degrees of accuracy depending on which materials they describe. In chapter 3, we have used the universal EOS (UEOS) and the 3rd order Birch-

Murnaghan EOS (BMEOS) to express the pressure P, the excess molar internal energy E_{ex}, and the excess molar enthalpy H_{ex} present in deformed regions characterized by an excess volume V_{ex}.

The pressure, bulk modulus, and thermal expansion predicted by the UEOS are in very good agreement with experimental data when describing metallic or covalent systems which makes it a perfect candidate to describe metal/metal hydride systems [122, 124]. Using the UEOS, we showed that the presence of excess volume could reduce the enthalpy of formation of certain metal hydrides [121] at zero temperature. Since the hydrogen release of most metal hydrides usually takes place at a temperature higher than room temperature [119, 127, 128], this chapter determines under which conditions the enthalpy of formation of a metal hydride would be further reduced by a temperature increase. Results are derived for the UEOS but could be generalized to other EOSs such as the BMEOS [121, 123, 124].

The thermodynamic potentials (internal energy E, enthalpy H, and free energy G) of any material can be obtained for any temperature, pressure and volume if one knows how these potentials vary with the relevant intensive and extensive variables. In the formulation that we proposed [121], we characterized the energy and the enthalpy of metal hydrides as a function of the excess volume present in the material as a result of mechanical treatments such as ball milling. It is thus convenient to use the volume and temperature as our independent variables when describing the thermodynamic properties of regions characterized by an excess volume.

Let us assume that the molar internal energy $E(T_o, v_o)$ of a material is known at a reference temperature T_o and for a molar volume v_o. One can then determine the effect of a temperature increase on the energy content of a material by integrating over the change of temperature and volume. Then, if the pressure is known, one can calculate the change in the enthalpy content

associated with a temperature change. Knowing the enthalpy content of both the metal and the metal hydride at high temperature, the enthalpy of formation can be directly obtained by subtracting the enthalpy of the metal from that for the metal hydride. From [129], we find that the energy difference between a solid taken from a state of pressure P_o and temperature T_o to a state of pressure P and temperature T is given by:

$$E(T,\upsilon) - E(T_o,\upsilon_o) = \int\limits_{T_o,\upsilon_o}^{T,\upsilon_o} C_V dT + \int\limits_{T,\upsilon_o}^{T,\upsilon} \left[T\left(\frac{\partial P}{\partial T}\right)_\upsilon - P \right] d\upsilon \qquad (4\text{-}1)$$

where C_V is the molar heat capacity and P is the pressure in the deformed regions of the solid. In Eq. 4-1 the first integral on temperature is performed at constant volume while the second integral on volume is performed at constant temperature T. The second integral, performed last, corresponds to the energy change arising from the volume increase associated with the thermal expansion of the solid. It is related to the entropy increase and the work done by the solid during the volume increase at temperature T. From the molar energy content, the molar enthalpy content at temperature T and pressure P is then be calculated by

$$H(T,\upsilon) = E(T,\upsilon) + |P(T,\upsilon)|\upsilon \qquad (4\text{-}2)$$

As discussed before, we take the absolute value of the pressure in Eq. 4-2 to account for the fact that for a negative hydrostatic pressure as well as for a positive one, the enthalpy content of the material will be increased. Computing Eq. 4-1 and Eq. 4-2 is a simple task when the energy content $E(T_o,\upsilon_o)$ of the material and the dependence of C_V and P on T and υ are known above a

certain reference temperature T_o. Finding an EOS that accurately describes P as a function of temperature and volume is the most important aspect in describing how the enthalpy of formation of metal hydrides is affected by temperature when regions with excess volume are present. The accuracy of the pressure function will determine the accuracy of our excess enthalpy calculations. We use the results developed [130] for the UEOS and show that the enthalpy of formation of metal hydrides above their Debye temperature Θ_D can be determined by only the bulk modulus, its first pressure derivative, and the coefficient of thermal expansion at a reference temperature $T_o > \Theta_D$. The results come from experimental evidence that above Θ_D, the pressure $P(v,T)$ is a linear function of temperature [131, 132]:

$$P(T,v) = P(T_o,v) + \alpha_o B_o (T - T_o) \tag{4-3}$$

where α_o and B_o are, respectively, the coefficient of thermal expansion and the bulk modulus at the reference temperature $T_o > \Theta_D$. In Eq. 4-3, the first pressure term on the right hand side corresponds to the reference isotherm while the second term is the thermal pressure term that comes directly from the observation that the pressure depends linearly on the temperature above Θ_D and from the definition of the first pressure derivative with respect to temperature:

$$\left(\frac{\partial P}{\partial T}\right)_{v,T=T_o} = -\left(\frac{\partial P}{\partial v}\right)_{T_o}\left(\frac{\partial v}{\partial T}\right)_{P,T=T_o} = \alpha_o B_o \tag{4-4}$$

The reference isotherm is found by using an EOS that correctly describes the behavior of the solid under consideration at the reference temperature T_o. In chapter 3, we have used the Birch-

153

Murnaghan 3rd order EOS and the UEOS to describe the relation between the excess energy and excess enthalpy present in a material subject to an excess volume [121]. Because the UEOS is in better agreement with experiments at higher excess volume [130], it will be used as the reference isotherm for the rest of this chapter [130]:

$$P(T_o, v) = \frac{3B_o}{\overline{V}^{2/3}}(1 - \overline{V}^{1/3}) \exp\left[\overline{\varepsilon}(T_o)(1 - \overline{V}^{1/3})\right]$$

(4-5)

where $\overline{V}$, the ratio of the molar volume v to the standard molar volume v_o at T_o is represented by

$$\overline{V} = \frac{v}{v_o(T = T_o, P = 0)} = \frac{vV_T}{v_o(T, P = 0)} = V_T V_R$$

(4-6)

where, the dimensionless thermal expansion ratio V_T is the ratio of the standard molar volume v_o at a temperature T and at the reference temperature T_o:

$$V_T = \frac{v_o(T, P = 0)}{v_o(T_o, P = 0)}$$

(4-7)

In Eq. 4-5 the parameter in the exponential depends on the first pressure derivative of the bulk modulus at standard temperature and zero pressure through

$$\bar{\varepsilon}(T_o) = \frac{3}{2}\left[\frac{\partial B}{\partial P}\bigg|_{P=0,T_o} - 1\right]$$ (4-8)

Our model is developed for temperatures above the Debye temperature where C_V is independent of an increase in temperature [133]. Moreover, from Eq. 4-3, because of the linear dependence of pressure on temperature, one can see that C_V is also independent of volume above Θ_D since [129]:

$$\left(\frac{\partial C_V}{\partial v}\right)_T = T\left(\frac{\partial^2 P}{\partial T^2}\right)_v$$ (4-9)

The last element needed to complete the model is the molar internal energy $E(T_o, v_o)$ of the material at the reference temperature T_o. Since we are interested in the excess energy and the excess enthalpy at high temperatures, it is more convenient to define and work with the excess molar internal energy $E_{ex}(T_o, v_o V_R)$ present in a material at the reference temperature due to the presence of excess volume:

$$E_{ex}(T_o, v_o V_R) = \int_{T_o, v_o}^{T_o, v_o V_R} \frac{3B_o}{\bar{V}^{2/3}}(1-\bar{V}^{-1/3})\exp\left[\bar{\varepsilon}(T_o)(1-\bar{V}^{-1/3})\right]dv$$ (4-10)

The above equations can now be combined to obtain the final expression that gives the excess enthalpy H_{ex} with respect to the standard state of a material at the reference temperature as a function of the relative volume V_R and the temperature T:

155

$$H_{ex}(T, \upsilon_o V_R V_T) = E_{ex}(T_o, \upsilon_o V_R) + |P(T, \upsilon_o V_R V_T)| \upsilon_o V_R V_T$$

$$+ \int_{T_o, \upsilon_o V_R}^{T, \upsilon_o V_R} C_V dT + \int_{T, \upsilon_o V_R}^{T, \upsilon_o V_R V_T} \left[T \left(\frac{\partial P}{\partial T} \right)_\upsilon - P(T, \upsilon) \right] d\upsilon \qquad (4\text{-}11)$$

The molar volume will be affected by both the thermal expansion and the excess volume. Because it is of interest to study the effect of the excess volume and the temperature independently, the total molar volume is represented as a product of the molar volume at the reference temperature and zero pressure υ_o, the dimensionless relative volume V_R, and the dimensionless thermal expansion ratio V_T. This allows us to study the independent impact of those variables even if the molar volume represents the thermodynamic variable of choice for the calculations of the different thermodynamic potentials. In Eq. 4-11, we first integrate over temperature at constant volume from the reference temperature T_o to T. Then we integrate at constant temperature over the volume change corresponding to the thermal expansion of the material. The volume expansion corresponding to a temperature increase in the deformed regions is approximated, as is done in [130], by the zero pressure thermal expansion through Eq. 4-3 and Eq. 4-5 by solving for V_T in :

$$\frac{3B_o}{\left(V_T \right)^{2/3}} (1 - \left(V_T \right)^{1/3}) \exp \left[\overline{\varepsilon}(T_o)(1 - \left(V_T \right)^{1/3}) \right] = -\alpha_o B_o (T - T_o) \qquad (4\text{-}12)$$

From the above equations, the total enthalpy content due to excess volume at a temperature T in any material can be found provided that an accurate reference isotherm for the pressure is known. To examine only the temperature dependence of the enthalpy of formation, the excess enthalpy contribution from the excess volume at the reference temperature is removed. The

excess enthalpy caused by an increase of temperature from T_o to T in a material with a relative

volume V_R then becomes:

$$
\begin{aligned}
H_{ex}^T(T, v_o V_R V_T) = v_o V_R \left(\left| P(T, v_o V_R V_T) \right| V_T - \left| P(T_o, v_o V_R) \right| \right) \\
+ \int_{T_o, v_o V_R}^{T, v_o V_R} C_V dT + \int_{T, v_o V_R}^{T, v_o V_R V_T} \left[T \left(\frac{\partial P}{\partial T} \right)_v - P(T, v) \right] dv
\end{aligned}
\tag{4-13}
$$

The right hand side of Eq. 4-13 highlights the 4 different contributions that change the

excess enthalpy of a material when the temperature is increased without including the excess

enthalpy that was already present in the sample due to excess volume at the reference

temperature. The first term outside of the integrals represents the change in the PV term arising

from the enthalpy definition (see Eq. 4-2) that is caused by the thermal pressure (see Eq. 4-3) and

the thermal expansion. The integral over the temperature gives the heat capacity contribution

while the first and second terms in the integral over the volume are, respectively, the entropy and

work contributions associated with the thermal expansion. As will be demonstrated in the

following sections, the relative importance of those terms for the metal and the metal hydride

will determine if an increase in temperature will lead to further destabilization of the metal

hydride with respect to the metal. It should finally be pointed out that since the reference

isotherm is derived at a temperature above Θ_D, the above approach will only be of interest for

hydrogen storage materials in which Θ_D is smaller than the hydrogen release temperature.

4.2 Condition for Destabilization

A metal hydride characterized by an excess volume V_{ex} and temperature T will be destabilized with respect to the metal state if the enthalpy of formation is reduced compared to that of the reference state:

$$\left[H_{MgH_2} - H_{Mg} - H_{H_2} \right]_{T=T,V_{ex}} \leq \left[H_{MgH_2} - H_{Mg} - H_{H_2} \right]_{T=T_o,V_{ex}=0} \qquad (4\text{-}14)$$

In [121], we demonstrated that the presence of deformed regions characterized by an excess volume would lead to a destabilization of the metal hydride with respect to the metal phase at zero temperature if the destabilization constant η is positive:

$$\eta = \left[v_o B_o \right]_{MH} - \left[v_o B_o \right]_M > 0 \quad \text{for } V_R \approx 1 \qquad (4\text{-}15)$$

A large positive η is favorable for hydrogen storage applications since it means that the enthalpy of formation between the metal and the hydride is reduced by the introduction of excess volume. A negative η, however, indicates that the presence of highly deformed regions in the sample should be avoided for hydrogen storage applications because it renders the metal hydride phase more stable with respect to the metal phase.

In the following section, the 4 temperature dependent contributions to the enthalpy in Eq. 4-13 will be reviewed and their sign as well as magnitude will be discussed to see if they could have a major impact on the enthalpy of formation of metal hydrides. The impact of temperature

will greatly depend on the metal and its related metal hydride properties. For non-zero temperatures, the impact of temperature on the enthalpy content of the hydrogen gas must also be evaluated in order to determine the exact enthalpy of formation of a metal hydride. We aim at providing a set of simple tools that can predict under which conditions an increase in temperature will have a positive influence, i.e. reduce the enthalpy of formation. The four temperature dependent contributions to the enthalpy of formation of metal hydrides as well as the contribution to the enthalpy of formation from the hydrogen gas will be calculated.

4.3 Temperature Impact on the Enthalpy of Formation of Magnesium Hydride

The following sections presents the four leading contributions to the enthalpy content of a material as temperature is increased. The impact of each of those contributions to the enthalpy of formation of MgH_2 is also discussed.

4.3.1 PV Contribution to the Enthalpy of Formation

The *PV* contribution to the enthalpy content of a material comes directly from the definition of the enthalpy (see Eq. 4-2), and the fact that both the pressure and the volume are temperature dependent. Here, one should remember that the pressure refers to the hydrostatic pressure within the deformed regions and not the outside pressure of the hydrogen gas. Of the four temperature

dependent enthalpy terms, the *PV* contribution is the only one that tends to reduce the enthalpy content of a solid material as the temperature increases. This is because a temperature increase reduces the internal pressure corresponding to a given V_{ex} faster than it increases the volume through thermal expansion, as seen in Fig. 4-1 which plots: (left) the relative pressure (defined as the ratio of the actual pressure to the pressure at standard temperature), and (right) the dimensionless thermal expansion as a function of temperature. Figure 4-1 shows that the pressure drops much faster with temperature than the volume increases.
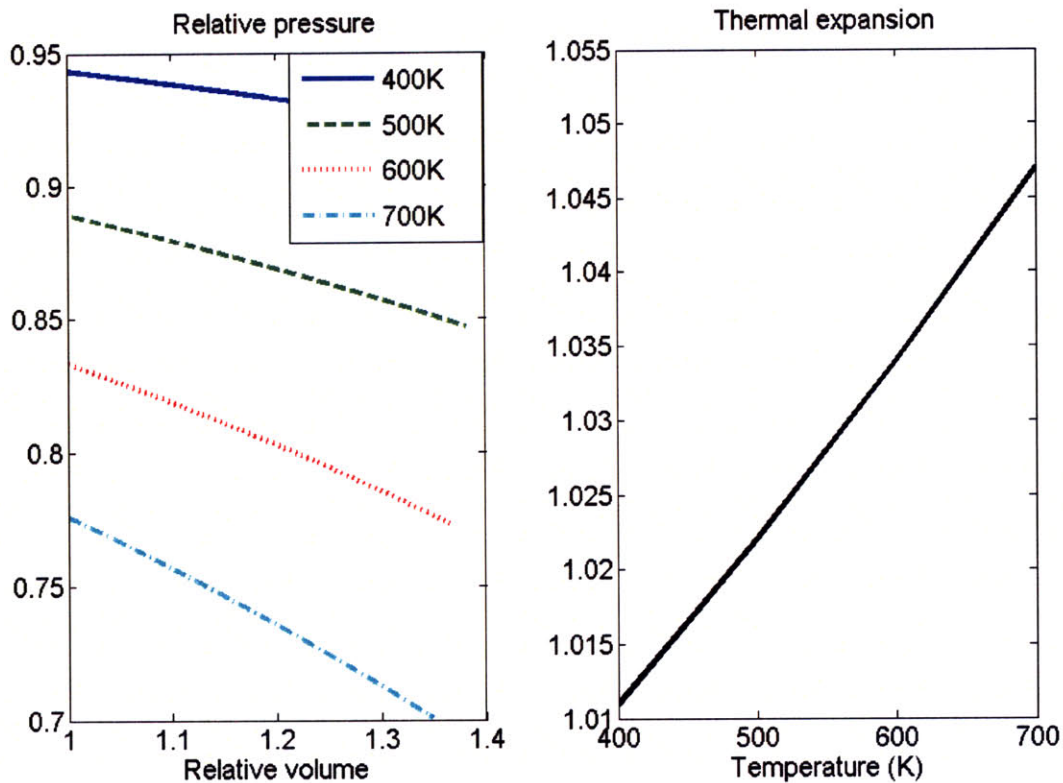
Figure 4-1. Relative pressure dependence on the relative volume at various temperatures (left), and thermal expansion ratio dependence on temperature (right).

By approximating the thermal expansion as linearly dependent on temperature by

160

$$v_o(T) \approx v_o(1 + \alpha_o \Delta T) = v_o V_T \qquad (4\text{-}16)$$

we can approximate the temperature dependent enthalpy contribution of the *PV* term to any material by:

$$H_{ex}^{PV}(T, v_o V_R V_T) = \left| P(T, v_o V_R V_T) \right| v_o V_R V_T - \left| P(T_o, v_o V_R) \right| v_o V_R$$
$$\approx v_o B_o V_R (-\alpha_o V_T \Delta T + \overline{P}(v_o V_R) - \overline{P}(v_o V_R V_T) V_T) \qquad (4\text{-}17)$$

where

$$\overline{P}(v) = \frac{P(T_o, v)}{B_o} \qquad (4\text{-}18)$$

is a universal dimensionless pressure function that depends on the material's properties only through the first pressure derivative of the bulk modulus (see Eq. 4-5 and Eq. 4-8). Note that Eq. 4-16 becomes less accurate as the temperature increases and that Eq. 4-12 should be used at elevated temperatures to determine the thermal expansion. The first term in Eq. 4-17 has a negative contribution and tends to reduce the enthalpy content of the material while the last two terms have a combined positive contribution and increase the enthalpy content. As the excess volume increases, the last two terms converge to the same value and cancel each other out for the temperature range of interest to metal hydrides and the first term that corresponds to the thermal pressure becomes dominant. The global effect is to reduce the enthalpy of the material when the temperature is increased.

161

To estimate the impact of a temperature increase on the enthalpy of formation of a metal hydride, one must calculate the difference between the PV contribution to the metal (M) and its respective metal hydride (MH). To destabilize the hydride, we need the following condition to hold true

$$\Delta H_{ex}^{PV}(T, \upsilon_o V_R V_T) = \left[H_{ex}^{PV}(T, \upsilon_o V_R V_T) \right]_{MH} - \left[H_{ex}^{PV}(T, \upsilon_o V_R V_T) \right]_M > 0 \qquad (4\text{-}19)$$

Looking at the dominant term in Eq. 4-17, an approximate condition under which the PV contribution will reduce the enthalpy of formation of the metal hydride can be written as:

$$\eta_{PV} = \left[\upsilon_o B_o \alpha_o \right]_{MH} - \left[\upsilon_o B_o \alpha_o \right]_M < 0 \qquad (4\text{-}20)$$

By comparing Eq. 4-15 and Eq. 4-20 we can see that as the temperature increases, the PV term will have an effect opposite to that of the excess volume. If the excess volume had a destabilizing effect on the metal hydride with respect to the metal for example, then the PV term would tend to stabilize the metal hydride. This happens because the temperature increase reduces the strain present in the deformed region more in the hydride than in the metal. Note that for materials where η_{PV} is almost equal to 0, then one should use the exact equations (see Eq. 4-17 and Eq. 4-19) to determine if the metal hydride is destabilized or not.

4.3.2 Heat Capacity contribution to the Enthalpy of Formation

The molar heat capacity C_V of a material is the measure of the heat energy required to increase the temperature of one mole of that material by a certain temperature interval at constant volume. Because the heat capacity of a metal and its associated hydride will generally not be the same, one can expect the enthalpy difference between the two materials to differ. Since the heat capacity is not a function of temperature above Θ_D (see section 4.1), Eq. 4-12 and a generalization of Eq. 4-19 tell us that if the temperature is increased, the enthalpy of formation of a metal hydride will be reduced by the heat capacity contribution to the enthalpy of the metal and the metal hydride, if

$$\eta_{C_V} = \left[C_V\right]_{MH} - \left[C_V\right]_M > 0 \qquad (4\text{-}21)$$

A metal hydride molecule will possess additional degrees of freedom compared to the metal atom alone on a molar basis and one can expect that the heat capacity of the hydride would surpass that of the metal, provided that those extra normal modes are not frozen out. Thus, the enthalpy of formation of the metal hydride should be further reduced by an increase of temperature to reflect the different amount of heat absorbed by the two materials to generate a temperature change. It should be emphasized that the contribution coming from the heat capacity is independent of the state of excess volume of the system above Θ_D. The large benefit gained from the heat capacity contribution thus cannot be attributed to the excess volume and should be considered as a basic property of the metal/metal hydride system.

163

4.3.3 Entropy Contribution to the Enthalpy of Formation

From Eq. 4-3, Eq. 4-13, and Eq. 4-16, it is shown that the excess enthalpy in a material that can be attributed to a change in the entropy accompanying the thermal expansion is approximated by

$$H_{ex}^{S}(T, \upsilon_{o}V_{R}V_{T}) = \int_{T, \upsilon_{o}V_{R}}^{T, \upsilon_{o}V_{R}V_{T}} T \left(\frac{\partial P}{\partial T} \right)_{\upsilon} d\upsilon \approx T\alpha_{o}^{2}B_{o}\Delta T \upsilon_{o}V_{R} \tag{4-22}$$

The dual dependence on the temperature and the temperature increase of the entropy contribution simply comes from the observation that the entropy content of a material increases with the thermal expansion while the enthalpy contribution is the product of temperature with that increase of entropy. For any temperature increase, this contribution is always positive for a single material so that the condition for the reduction of the enthalpy of formation of a metal hydride with increasing temperature due to the entropy contribution becomes

$$\eta_{S} = \left[\upsilon_{o}B_{o}\alpha_{o}^{2}T \right]_{MH} - \left[\upsilon_{o}B_{o}\alpha_{o}^{2}T \right]_{M} > 0 \tag{4-23}$$

which is similar to the condition for the *PV* term but of opposite sign. We retained the temperature in Eq. 4-23 in order to keep η_S in units of J/mol-K. The entropy term tends to be very small compared to the *PV* term because it is proportional to $T\Delta T\alpha_{o}^{2}$ (quadratic dependence on the thermal expansion coefficient α_o which has a typical 10^{-5} to 10^{-6} order of magnitude) while the *PV* term is roughly proportional to $(1 + \Delta T\alpha_o) \Delta T\alpha_o$. The contribution of the entropy

164

term is nevertheless of a relative importance (especially at high temperature) for small excess volume values where the work associated with the thermal expansion and the *PV* contributions terms tend to be negligible.

4.3.4 Work Related to the Thermal Expansion Contribution to the Enthalpy of Formation

The last term to consider in Eq. 4-13 is the contribution to the enthalpy from both the metal and the metal hydride arising from the work associated with the thermal expansion:

$$H_{ex}^V(T,v_oV_RV_T) = \int\limits_{T,v_oV_R}^{T,v_oV_RV_T} -P(T,v)dv \qquad (4\text{-}24)$$

The hydrogen release from a metal hydride typically occurs at a temperature of the order of 400K-800K. For such a temperature range, the magnitude of the thermal expansion is small and the change in $\overline{P}(V)$, which is only dependent on the thermal expansion for a fixed excess volume, is relatively small as well. In Eq. 4-24 we thus treat the pressure change over the small thermal expansion as linear and the integral over the volume is approximated by:

$$H_{ex}^{V}(T, \upsilon_o V_R V_T) \approx \upsilon_o B_o V_R \alpha_o \Delta T \left[-\alpha_o \Delta T - \left(\frac{\overline{P}(\upsilon_o V_R V_T) + \overline{P}(\upsilon_o V_R)}{2} \right) \right] \qquad (4\text{-}25)$$

In Eq. 4-25 the first term is negative and tends to decrease the enthalpy content of a material, while the second term destabilizes the material by increasing its enthalpy (the hydrostatic pressure inside a region of excess volume is negative). The integral in Eq. 4-24 leading to the result of Eq. 4-25 corresponds to a volume expansion at fixed temperature that took place after an integral on temperature at fixed volume is calculated. This means that for small excess volume, the lower limit on the integral corresponds to a state of compression with respect to equilibrium. So for a small excess volume and high temperature, the first term in Eq. 4-25 will tend to dominate because it corresponds to the relaxation of a compressed state induced by the thermal expansion of the material. However, as the excess volume increases, the second term which corresponds to the isothermal expansion of the material toward a state of higher excess volume takes over and increases the enthalpy content of the material. The exact excess volume for which, at a given temperature, the work associated with the thermal expansion makes a transition from a stabilizing contribution to a destabilizing contribution will depend on the specific properties of the metal/metal hydride under study. In the case of Mg, given that the thermal expansion is relatively weak at the temperatures of interest (see Fig. 4-1), the first term will dominate only at an excess volume on the order of 0 to 0.05, depending on temperature.

At low excess volume where the thermal relaxation dominates, we can thus write an expression that gives the condition for further destabilization of a metal hydride as:

$$\eta_V = \left[v_o B_o \alpha_o^2 \Delta T \right]_{MH} - \left[v_o B_o \alpha_o^2 \Delta T \right]_M < 0 \qquad (4\text{-}26)$$

On the other hand, at high excess volume, if the first bulk modulus derivatives are of the same order of magnitude between the metal and the hydride, we can write the condition as:

$$\eta_V = \left[v_o B_o \alpha_o \right]_{MH} - \left[v_o B_o \alpha_o \right]_M > 0 \qquad (4\text{-}27)$$

This condition is the same as that of the *PV* contribution, but it has the opposite sign. In the *PV* term, the pressure reduction over the whole sample offsets the small volume increase due to the work associated with the thermal expansion and the total *PV* term is negative. For the work associated with the thermal expansion, we only calculate the increase in enthalpy resulting from adding a small volume element so that even if the thermal expansion reduces the pressure, the total contribution to increasing the volume will always be positive.

4.3.5 Impact of Temperature on the Enthalpy of Hydrogen

While the state of excess volume of the metal and the metal hydride does not affect the enthalpy content of the hydrogen gas, the temperature will have an effect that must be taken into consideration. For automotive applications, the hydrogen release from the metal hydride would be achieved by increasing the temperature of the reservoir as to keep the hydrogen pressure to the fuel cell constant. If one assumes that the hydrogen pressure is kept constant as the

temperature is increased, then excess enthalpy of the hydrogen gas relative to the standard state is given by:

$$H_{ex}^{H_2} = C_P \Delta T \qquad (4\text{-}28)$$

where the specific heat capacity C_P at constant pressure for the hydrogen is approximately constant at 28.8 J/mol-K over the temperature range of interest [134].

4.4 Results and Discussion

We used the results from section 4.1 to calculate the high temperature enthalpy contribution to Mg/MgH$_2$ and the temperature dependence of ΔH in MgH$_2$. For both Mg and MgH$_2$ we used room temperature (298K) as the reference temperature T_o. At room temperature, the only parameters needed for our model, namely the bulk modulus, the first derivative of the bulk modulus with respect to pressure, the molar heat capacity, and the coefficient of thermal expansion are available in the literature. It must be mentioned though that this value of the reference temperature is lower than Θ_D for both Mg (400K [133]) and MgH$_2$ (456K using Debye model for the density of states to estimate Θ_D [133]). As mentioned in section 4.1, our model is based on the assumption that the reference temperature is above the Debye temperature of the solids so that the thermal pressure has a linear dependence on the temperature. Nevertheless, results by [131, 132] actually suggest that the linear relationship between the thermal pressure and the temperature remains valid well below Θ_D so that selecting a reference temperature that is

25-35% lower than Θ_D is not expected to significantly affect the accuracy of our calculations. Moreover, at a temperature so close to Θ_D, one can still consider the heat capacity at constant volume to be independent of temperature [133].

Figure 4-2 plots the excess enthalpy in Mg for each of the four contributions in Eq. 4-13 as a function of the relative volume at various temperatures. As explained in Section 4.3, the entropy, heat capacity from the solids and the hydrogen and work associated with the thermal expansion contributions will tend to increase the enthalpy content of Mg while the PV term tends to reduce it. It is obvious from Fig. 4-2 that the PV and heat capacity terms dominate the heat dependent properties of the enthalpy contained in excess volume regions. The entropy term is much smaller than the other terms because of its quadratic dependence on the thermal expansion coefficient (from the pressure derivative and the thermal expansion) except at low V_{ex} where the PV term together with the work associated with the thermal expansion contributions are closer to 0. The work term also remains relatively small compared to the PV and C_V terms because of the weak thermal expansion that is observed for the temperature changes of a few hundred degrees that are relevant to hydrogen storage. The increase in the negative hydrostatic pressure characterizing deformed regions as the temperature is increased by a few hundred degrees is much more important than the thermal expansion that compensates the pressure drop which leads to the dominance of the PV term at high pressure and excess volume (see Fig. 4-1). At high excess volume and temperature, Fig. 4-2 shows that the PV term can lead to an enthalpy reduction of more than 20kJ/mol for Mg. This reduction, however, does not mean that the enthalpy of formation of MgH_2 would be reduced by that amount since the PV contribution to MgH_2 will be even larger at high excess volume and temperature.
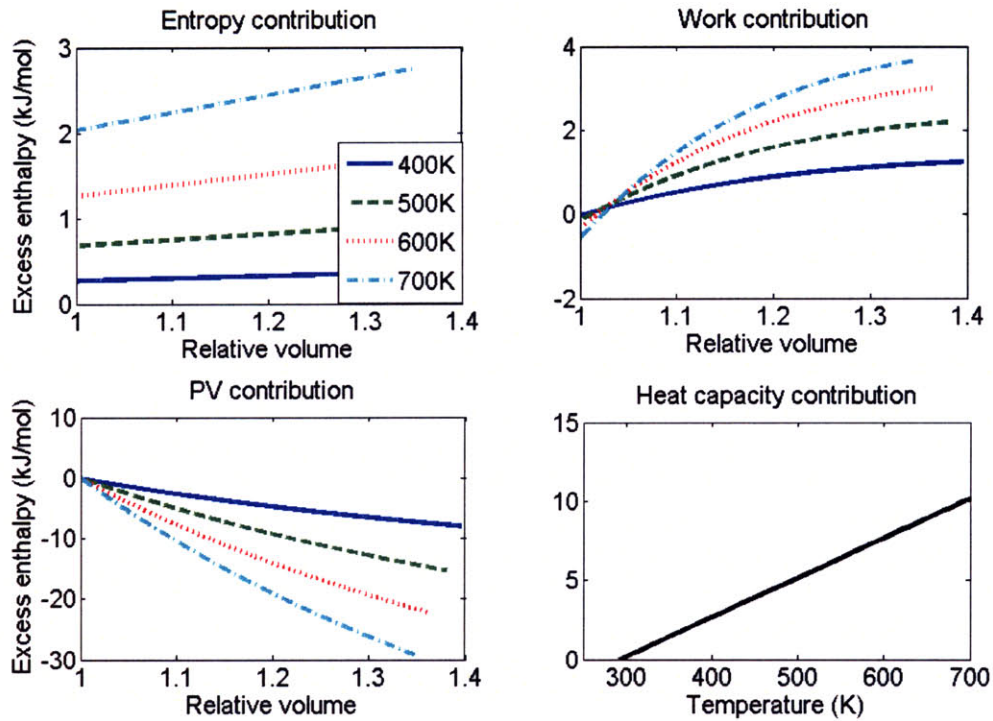
Figure 4-2. Excess enthalpy in Mg for each of the four contributions in Eq. 4-13 at various temperatures. The heat capacity term is independent of the relative volume above the Debye temperature.

The influence on the enthalpy of formation of MgH_2 is obtained by comparing the impact of temperature and excess volume on the enthalpy content of Mg and MgH_2. The change in the enthalpy content of the hydrogen gas must also be taken into account. Since we must take the difference between the Mg and MgH_2 temperature dependent enthalpy content, it is not obvious that the leading term for the enthalpy of formation will remain the *PV* term as in the case of the individual enthalpy contents of the metal and the metal hydride. There could be, for example, a situation where the *PV* contributions are about the same for both materials, while the entropy, the heat capacity, or the thermal expansion work terms would introduce significant differences between the metal and the metal hydride. The term for which the difference is the largest

170

between the metal and the metal hydride will ultimately dominate the high temperature enthalpy contribution. In the previous section we came up with general guidelines to determine whether or not an increase in temperature would benefit a reduction in ΔH and what would be the magnitude of the change in ΔH. Figure 4-3 plots the individual temperature dependent contributions to the enthalpy of formation of MgH_2, while Fig. 4-4 plots the total excess enthalpy of formation of the hydride as a function of the relative volume for various temperatures. Except at very low excess volume and high temperature, the excess enthalpy of formation is positive so that the total enthalpy of formation will be reduced in magnitude and the metal hydride will be destabilized with respect to the metallic phase. The destabilization will then make the hydrogen release easier by reducing the amount of heat that must be supplied to the metal hydride for the hydrogen release.

The first observation from Fig. 4-3 and Fig. 4-4 is that the contribution from the temperature increase tends to lower the excess enthalpy and is important compared to the room temperature excess volume only at small values of V_{ex}. For small V_{ex} and high temperature, the difference between the heat capacity terms of reactants (Mg and H_2) and the product (MgH_2) tends to dominate and the metal hydride is stabilized with respect to the metal phase. So an increase in temperature increases the enthalpy of formation for all excess volume.
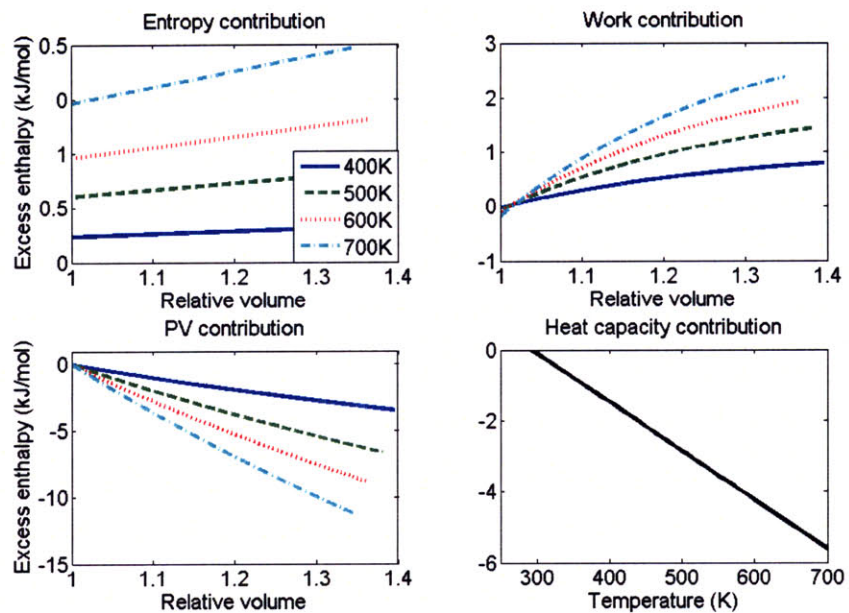
Figure 4-3. Excess enthalpy of formation in MgH$_2$ for each of the four contributions at various temperatures. The heat capacity term is independent of the relative volume above the Debye temperature.
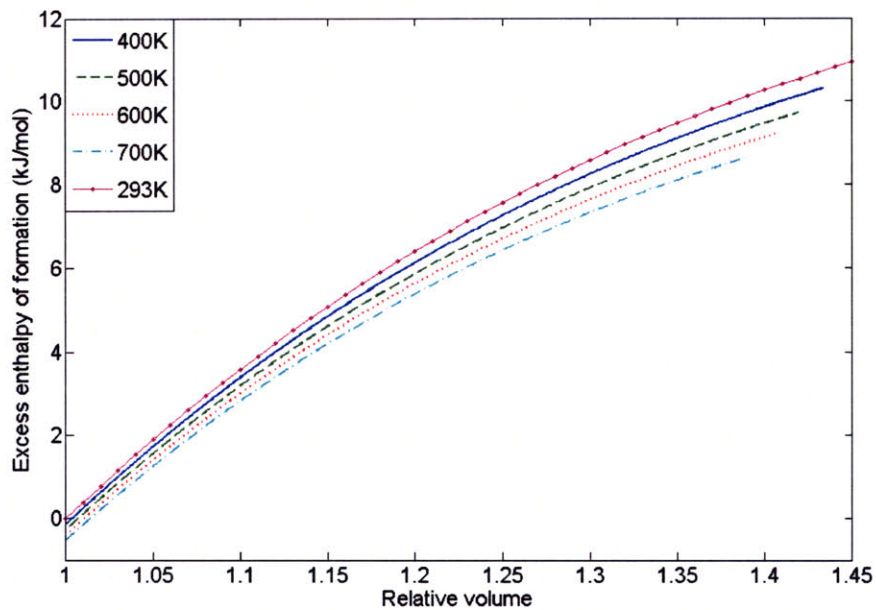
Figure 4-4. Total excess enthalpy of formation as a function of the relative volume at various temperatures for MgH$_2$.

172

To better understand the results though, it is helpful to ignore the heat capacity contribution of both the solids and the hydrogen gas when calculating the impact of temperature on the enthalpy content of the deformed regions because the C_V and C_P contributions are not a property of the excess volume regions but rather a property of the hydrogen/metal/metal hydride system. Without the contribution of the heat capacity, it becomes evident that the negative PV term dominates the high temperature behavior of the excess enthalpy of formation caused by deformed regions in the Mg/MgH$_2$ system (see Fig. 4-5). For a given excess volume, the higher the temperature is, the greater is the reduction of the internal pressure associated with deformed regions. Since the thermal expansion does not match this pressure reduction, the excess enthalpy present in deformed regions is reduced and part of the positive impacts of the excess volume is lost. From a physical perspective, as the temperature is increased, the bulk modulus associated with a given excess volume is reduced and it demands less energy to create a deformation [35] such that a given PV state has a lesser enthalpy at high temperature. For materials with high bulk modulus (such as MgH$_2$ compared to Mg), this effect is even more pronounced since the thermal pressure is proportional to the bulk modulus, which further reduces the internal pressure of the solid with temperature (see Eq. 4-3). This is why the thermal pressure tends to offset the impact of the hydrostatic pressure in the case of MgH$_2$.
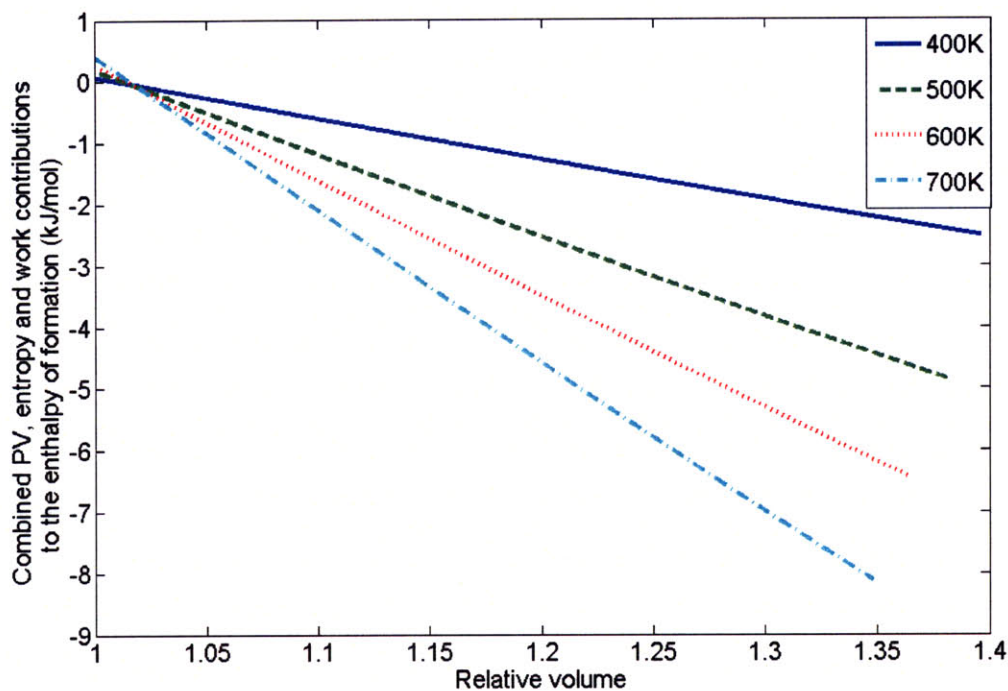
Figure 4-5. Total temperature dependent contribution to the enthalpy of formation of MgH$_2$ excluding the heat capacity contribution as a function of the relative volume at various temperatures.

Excluding the impact of the heat capacity, a temperature increase will not always increase the enthalpy of formation for all metal hydrides. The impact of temperature on ΔH will generally be dictated by the difference between the two *PV* contributions. Both Eq. 4-15 and Eq. 4-20 illustrate the fact that the thermal pressure (see third term in Eq. 4-3) will generally have an opposite impact on the enthalpy of formation than the excess volume has if the thermal expansion coefficients are not significantly different between the metal and the metal hydride. This is because B_o and V_o are the dominant terms that determine whether a metal/metal hydride system will be destabilized by the introduction of excess volume or by an increase in temperature [121]. In the case of the excess volume contribution, a metal hydride will be destabilized with

174

respect to a metal if the product of V_oB_o of the hydride is larger than that of a metal (see Eq. 4-15). This can be understood easily if one compares the solid to a 3D harmonic oscillator in which V_oB_o behaves as the potential energy stored in the atomic bonds. As the temperature is increased, the pressure inside the deformed regions of the material with the larger V_oB_o will decrease much faster than the pressure inside the material with the lower V_oB_o. The pressure drop reduces the PV contribution to the enthalpy because the thermal expansion cannot compensate for it. For materials like TiH_2 where excess volume is a source of stabilization [121], it is thus expected that temperature will decrease the enthalpy of formation at high excess volume and destabilize the material while in MgH_2 we have shown that the opposite behavior is expected.

In the case of MgH_2, it is interesting to look at the impact of temperature on the total enthalpy of formation of the material. In [121], we showed that a V_{ex} of 0.2 to be present over ~ 14% of the sample could reproduce the experimental results on the enthalpy of formation reduction in nanocrystalline MgH_2 [114], by providing up to 10kJ/mol (13.3%) additional reduction in the enthalpy of formation in addition to the surface and grain energy contributions (the impact of metastable phases such as γ-MgH_2 was found to be negligible). Excluding the heat capacity contribution, this value would go down to 9.3kJ/mol (12.4%) as the temperature is increased toward the release temperature of hydrogen (~700K) [114]. This shows that temperature has a very limited impact in the Mg/MgH_2 system. Figure 4-6 shows the relative change in the excess enthalpy of formation of MgH_2 present in deformed region as a function of the relative volume at various temperatures. The relative change is measured with respect to the reference temperature T_o. A positive percentage means that increasing the temperature reduces the enthalpy of formation by that percentage, while a negative value signifies that increasing the

temperature offsets the benefits of introducing excess volume. At very low excess volume, an increase in temperature reduces the magnitude of the enthalpy of formation (favorable contribution); while for larger excess volume the impact of temperature opposes the impact of excess volume. At all temperatures and excess volumes though, the relative contribution remains less than 10% of the total excess enthalpy of formation contained in the deformed regions. Thus we conclude that the thermodynamic gains made by mechanical deformation of the metal hydride would be retained as the release temperature is reached if relaxation could be prevented.
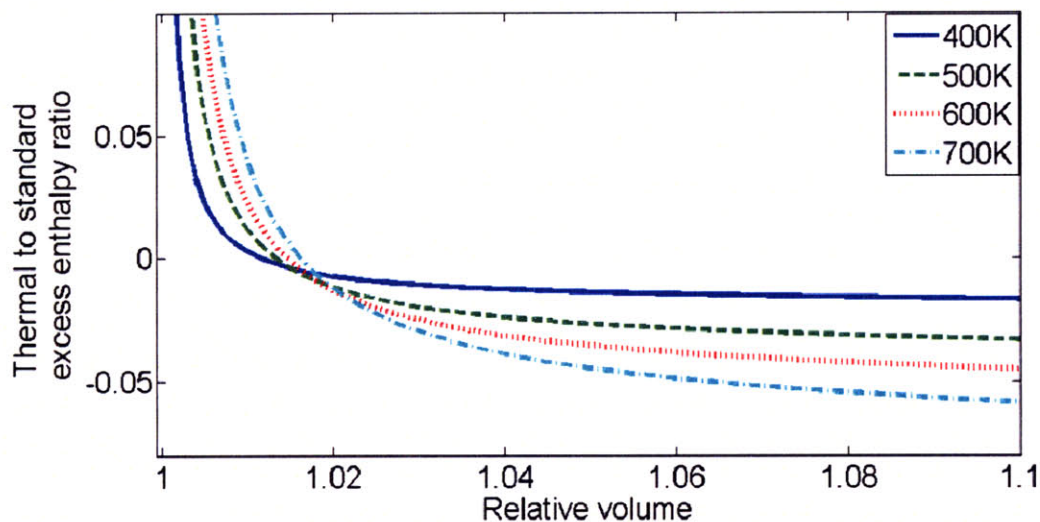
Figure 4-6. Ratio of the combined PV, entropy, and work excess enthalpy of formation of MgH$_2$ to the standard enthalpy of formation as a function of the relative volume for various temperatures.

In [121], it was shown that different volume fractions and excess volume values could reproduce the same experimental results on the reduction of the enthalpy of formation. From the above observations, we conclude that for a given reduction of the enthalpy of formation

attributed to the presence of regions characterized by an excess volume, it is more beneficial to have a large fraction of the material in a state of small excess volume instead of having a small fraction of the material in a state of large excess volume. This choice reduces the negative impact of a temperature increase on the enthalpy of formation of metal hydrides and can even further destabilize a metal hydride if it possesses large regions of sufficiently small excess volumes. It can also be concluded that each metal/metal hydride system would possess an optimal excess volume value and excess volume fraction for which the impact of temperature are the most advantageous without compromising on the destabilization potential provided by the deformation. Furthermore, it is likely that regions characterized by lower excess volume will be more stable to relaxation because of their lower free energy so that their advantageous thermodynamic properties could be maintained over many high temperature hydriding/dehydriding cycles. In general, a structure characterized by a high enthalpy will also be characterized by a high free energy which favors the relaxation toward more stable phases [121]. For high temperature and excess volume, however, the high entropy content of the grain boundary could lead to an entropy stabilization of the deformed regions. This phenomenon will be described in chapter 5.

4.5 Summary

In this chapter we established a high temperature generalization of our previous findings on the thermodynamic properties at $T = 0K$ of deformed regions produced by the ball milling of metal hydrides. As the temperature is increased, the enthalpy content of the metal and the metal

hydride change due to contributions from the heat capacity, the work associated with the thermal expansion, the expansion generated entropy and the temperature impact on the hydrostatic pressure inside the solid. At low excess volume, excluding the heat capacity terms, the entropy contribution dominates and further destabilizes the metal and the metal hydride with respect to their ground state. Since the C_V contribution is not a property of the deformed regions but rather a property of the metal/metal hydride system, it is convenient to exclude it when looking at the influence of temperature on the properties of the deformed regions. As the excess volume increases, the PV contribution becomes dominant at high temperature as the pressure drop within deformed regions reduces the excess enthalpy present in those regions. The reduction in the PV term with temperature is proportional to B_oV_o as is the case for the excess enthalpy present in a deformed region but is of the opposite sign. So excluding the C_V contribution, the impact of an increase of temperature on the enthalpy of formation will be opposite to the impact of the deformations occurring at the standard temperature, but of a much smaller magnitude. As the hydrogen release temperature is approached, part of the thermodynamic benefits gained from introducing deformed regions is thus lost. This effect is even more pronounced if the destabilization of the hydride is produced by a small volume fraction of the solid having a large excess volume compared to having a large volume fraction of the material in a state of small excess volume. It is expected that the deformed regions characterized by a high enthalpy will also be characterized by a high free energy which might favor the relaxation toward a more stable crystalline phase. For high temperature and excess volume however, the high entropy content of the grain boundary could lead to an entropy stabilization of the deformed regions. This phenomenon will be described in chapter 5.

5 Entropy Stabilization of Deformed Regions of Metals and Metal Hydrides Characterized by an Excess Volume

Reducing the high enthalpy of formation of metal hydrides by mechanically or chemically destabilizing the metal hydride with respect to the metal phase offers a potential way to address the challenges associated with storing hydrogen in metal hydrides [121, 135].

The excess enthalpy present in both the metal and the metal hydride as a result of deformations will result in an excess free energy. Because of the high temperatures at which the hydriding/dehydriding reaction takes place in metal hydrides [127, 128], the excess free energy could lead to the relaxation of the materials into their more stable crystalline phase over many high temperature hydriding/dehydriding cycles if no significant energy barriers to relaxation are present [120, 136]. If relaxation occurs, the benefits of the excess volume on the enthalpy of formation would be lost and the hydrogen storage system durability through repeated cycles would be compromised. It is thus important that the nanostructures responsible for the improved thermodynamic properties can be maintained over many hydriding/dehydriding cycles. One way to improve the durability of a high enthalpy state in a metal hydride is to generate a metastable

state in which a relatively high energy barrier prevents the high enthalpy state from relaxing into a more stable one. At the high temperature associated with hydrogen release from a metal hydride, the excess entropy present in the deformed regions containing excess volume can generate such a metastable state under certain conditions by reducing the excess free energy of the deformed regions [36, 37]. For instance, Fecht [36, 37] calculated that at 500K, the grain boundary in a Cr cluster could be stabilized in a state that has a 27kJ/mol excess enthalpy.

In this chapter, a framework to calculate the excess entropy content of the deformed regions of metal hydrides will be given. For the Mg/MgH_2 system, it will be shown that at high temperature, it is possible to improve the durability of a destabilized metal hydride by forcing the Mg and MgH_2 to oscillate between two metastable states.

5.1 Destabilization and Excess Volume

The relation between the excess energy/enthalpy in a solid containing excess volume due to mechanical deformations can be described by an equation of state (EOS) linking the energy, pressure, and enthalpy inside the material to its state of excess volume [34, 35, 124, 130].

In chapter 4 (the results were also published in [135]), we used the results developed by Vinet et al. [130] for the UEOS and showed that the enthalpy of formation of metal hydrides above their Debye temperature Θ_D can be determined by only the bulk modulus and its first pressure derivative, the molar volume, the heat capacity at constant volume, and the coefficient of thermal expansion at a reference temperature $T_o > \Theta_D$ as input variables. The universal EOS developed in chapter 4 is reproduced here:

$$P(T,\upsilon) = \frac{3B_o}{\overline{V}^{2/3}}(1-\overline{V}^{1/3})\exp\left[\overline{\varepsilon}(T_o)(1-\overline{V}^{1/3})\right] + \alpha_o B_o(T-T_o)$$ (5-1)

in which α is the coefficient of thermal expansion, B is the bulk modulus and the subscript 'o'

refers to values at a reference temperature T_o higher than Θ_D. Here, the ratio of the actual molar

volume υ to the standard molar volume υ_o at T_o is given by

$$\overline{V} = \frac{\upsilon}{\upsilon_o(T=T_o, P=0)} = \frac{\upsilon V_T}{\upsilon_o(T, P=0)} = V_T V_R$$ (5-2)

where, the dimensionless thermal expansion ratio V_T is the ratio of the standard molar volume υ_o

at a temperature T and at the reference temperature T_o:

$$V_T = \frac{\upsilon_o(T, P=0)}{\upsilon_o(T_o, P=0)}$$ (5-3)

Thus $\overline{V}$ accounts for the effect of both the dimensionless relative volume V_R and the

dimensionless thermal expansion ratio V_T of the material [135]. V_T corresponds to the ratio of the

equilibrium molar volume at temperature T to the equilibrium molar volume at T_o [135].

The excess molar internal energy and excess enthalpy of both the metal and the metal

hydride as a function of their state of excess volume and temperature can be obtained from the

following relations [129, 135] :

$$E_{ex}(T,\upsilon) = E(T,\upsilon) - E(T_o,\upsilon_o) = \int\limits_{T_o,\upsilon_o}^{T,\upsilon_o} C_V dT + \int\limits_{T,\upsilon_o}^{T,\upsilon} \left[T\left(\frac{\partial P}{\partial T}\right)_\upsilon - P \right] d\upsilon \qquad (5\text{-}4)$$

$$H(T,\upsilon) = E(T,\upsilon) + |P(T,\upsilon)|\,\upsilon \qquad (5\text{-}5)$$

$$\begin{aligned} H_{ex}(T,\upsilon_o V_R V_T) &= H(T,\upsilon_o V_R V_T) - H(T_o,\upsilon_o) = E_{ex}(T_o,\upsilon_o V_R) \\ &+ |P(T,\upsilon_o V_R V_T)|\,\upsilon_o V_R V_T + \int\limits_{T_o,\upsilon_o V_R}^{T,\upsilon_o V_R} C_V dT + \int\limits_{T,\upsilon_o V_R}^{T,\upsilon_o V_R V_T} \left[T\left(\frac{\partial P}{\partial T}\right)_\upsilon - P(T,\upsilon) \right] d\upsilon \end{aligned} \qquad (5\text{-}6)$$

where C_V is the molar heat capacity of the material.

The presence of deformed regions leads to an increase in the enthalpy and to the destabilization of both the metal and the metal hydride with regard to their equilibrium states. A reduction of the enthalpy of formation signifies that the transition from the metal hydride to the metallic state will be facilitated [93, 121, 135]. This can potentially reduce the release temperature, speed up the kinetics and limit the heat released during the hydriding reaction. The properties of the metal/metal hydride system could thus be improved in an essential way for hydrogen storage applications, if the system can maintain its excess volume over multiple cycles of hydriding/dehydriding. In the next section, the excess entropy present in regions of excess volume will be quantified and its impact on the relaxation rate of the deformed region will be evaluated by using a homogeneous nucleation theory.

5.2 Excess Entropy and Nanostructures Stabilization

Entropy is a measure of the randomness of molecules in a system or the system's degree of disorder. The entropy of a deformed region characterized by an excess volume is thus expected to increase compared to its orderly crystalline state. This increase in entropy will reduce the free energy of the deformed region by opposing the increase in the enthalpy and could help stabilize the deformed regions in a state of high enthalpy on the basis of Eq. 5-7

$$G_{ex} = H_{ex} - TS_{ex} \qquad (5\text{-}7).$$

To quantify the excess entropy present in a deformed region at any given temperature, one notes that an infinitesimal change in temperature or volume leads to a change in the entropy content of a system [129]:

$$dS = \left(\frac{\partial S}{\partial T}\right)_v dT + \left(\frac{\partial S}{\partial v}\right)_T dv = \frac{C_V}{T}dT + \left(\frac{\partial P}{\partial T}\right)_v dv \qquad (5\text{-}8)$$

From the standard entropy content of a system, one can obtain the high temperature and high excess volume entropy content of a material by integrating the partial derivatives of the entropy along a preferred path. We first integrate over the temperature at constant volume and then integrate over the volume at constant temperature.

$$S(T,v) = S(T_o, v_o) + \int\limits_{T_o, v_o}^{T, v_o} \frac{C_V}{T} dT + \int\limits_{T, v_o}^{T, v} \left(\frac{\partial P}{\partial T} \right)_v dv \qquad (5\text{-}9)$$

As mentioned above, the maximum value that the molar volume v can take in Eq. 5-9 is bounded by the maximum excess volume possible in a material before the Gibbs instability is reached [93]. The maximum excess volume corresponding to the Gibbs instability is denoted by V_{crit}.

The first term in Eq. 5-9 is a trivial integral over the specific heat at constant volume. Since the model is developed for temperatures above the Debye temperature Θ_D, C_V is independent of an increase in temperature [133]. The second integral in Eq. 5-9 is obtained using the Slater approximation for the dimensionless Grüneisen parameter γ_G [133]:

$$\left(\frac{\partial P}{\partial T} \right)_v = \alpha B = \frac{\gamma_G C_V}{v} = \left[\frac{1}{2} \left(\frac{\partial B}{\partial P} \right)_T - \frac{1}{6} \right] \frac{C_V}{v} \qquad (5\text{-}10)$$

where the pressure derivative of the bulk modulus is obtained from Eq. 5-1 as [130]:

$$\frac{\partial B(T, V_R(T_o))}{\partial P} = \frac{4 + \left[3\bar{\varepsilon}(T_o) - 1 \right] V_R^{1/3}(T_o) + \bar{\varepsilon}(T_o)[\varepsilon(T_o) - 1] V_R^{2/3}(T_o) - \bar{\varepsilon}^2(T_o) V_R(T_o)}{3 \left[2 + \left(\bar{\varepsilon}(T_o) - 1 \right) V_R^{1/3}(T_o) - \bar{\varepsilon}(T_o) V_R^{2/3}(T_o) \right]} \qquad (5\text{-}11)$$

The Grüneisen parameter γ_G (see Eq. 5-10) describes the alteration in the crystal lattice's vibration frequency of a material in a state of excess volume. The Grüneisen parameter diverges to infinity close to V_{crit} indicating a vibrational catastrophe as the Gibbs instability is approached.

184

At high excess volume, this term will make a major contribution to the excess entropy of the destabilized metal and the destabilized metal hydride. In Eq. 5-1, it is assumed that the first partial derivative of the pressure with respect to T is constant and equal to a_oB_o. Nevertheless this fails to reproduce the divergence of the Grüneisen parameter as the V_{crit} is approached. Since we are interested in the entropy catastrophe close to V_{crit}, we use the exact definition of the pressure derivative (see first term in Eq. 5-10) to describe the material's properties close to V_{crit}.

As V_{ex}/V_R is increased, Eq. 5-9, Eq. 5-10, and Eq. 5-11 predict that the entropy will exhibit a divergence and tend to infinity. From a physics point of view, the maximum entropy that a molecule or atom can have is that of a gas and there will thus be a limit on the excess entropy resulting from a deformation. This maximum excess molar entropy S_{max} corresponds to the entropy of sublimation of the material (see Eq. 5-12) [137] beyond which the material becomes unstable with respect to its gas phase. The maximum excess entropy with respect to the reference state is the difference between the entropy of a gas at the sublimation temperature T_s and the entropy of the reference state. It is calculated by adding the contributions from the heat of fusion, the heat of sublimation and the heat capacity of the material:

$$S_{\max} = \frac{L_f^h}{T_f} + \frac{L_s^h}{T_s} + \int_{T_o}^{T_s} \frac{C_V dT}{T}$$

(5-12)

in which L_f^h and L_s^h are, respectively, the molar heats of fusion and sublimation.

Even if this upper limit on the molar excess entropy is measured from the gas phase, it is applicable to the solid phase and has been observed experimentally in super-heated crystals where the high entropy stabilizes the crystals against melting [138]. A similar phenomenon was

also observed in nanoparticles of Pd which showed an increased resistance to sintering as a result of heavy deformations [139].
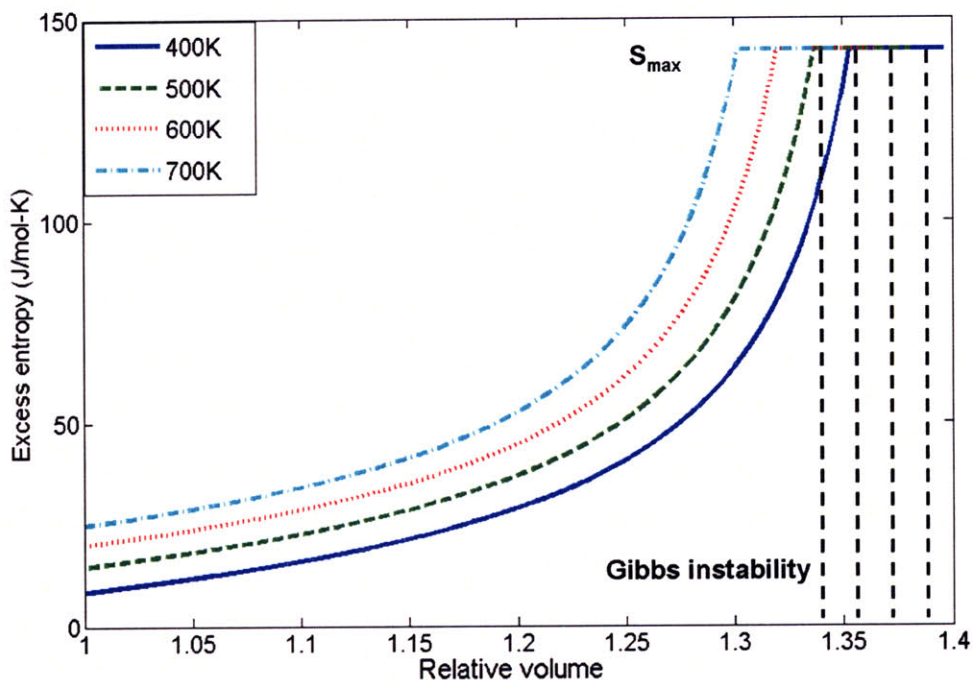
Figure 5-1. Excess entropy as a function of the relative volume in Mg at various temperatures.

That the maximum entropy is reached before the Gibbs instability sets in (see Fig. 5-1) is essential for the creation of a metastable state. If both the metal and metal hydride can be stabilized in such a fashion, it would provide a permanent way to reduce the enthalpy of formation of the hydride. For Mg, we calculated that this upper limit on the entropy occurs right before the critical volume V_{crit} is reached (see Fig. 5-1). In section 5.4, we will show how the upper bound to the excess entropy can lead to a local minimum in the free energy of a destabilized region that will make that region metastable with regard to a lower excess volume (lower enthalpy) region. Understanding how the excess entropy could lead to a stabilization of

the deformed regions also requires an understanding of the impact of the excess free energy on the recrystallization rate of the deformed region. This is discussed in the following section (section 5.3).

5.3 Relaxation of the Deformed Region

During the deformation of a crystalline material, the free energy is raised by the accumulation of grains and dislocations and the regions containing such defects are characterized by an excess volume and are thermodynamically unstable. Excluding energy barriers as well as physical and kinetic limitations, thermodynamics would suggest that the high free energy states would relax into their more stable crystalline state. As a result, the thermodynamic improvement gained from the presence of deformations would be lost upon cycling. This relaxation occurs because the excess enthalpy present in both the metal and the hydride will usually lead to an excess free energy G_{ex} at moderate temperatures and small values of excess volume. That material therefore tends to spontaneously relax to states of lower free energy [129, 136].

The exact mechanism through which nanostructures relax depends on their nature as well as the intrinsic properties of the material. For example, in a deformed material, relaxation can start through a subgrain growth process called recovery, whereby the dislocation structure changes [120]. Then, the nucleation of crystalline grains takes place and further relaxation can occur through grain growth [120, 136]. As stated earlier, it is believed that the accumulation of defects around a crystalline nucleus, in heavily deformed materials, can lead to extended grain boundaries characterized by an excess volume. The regions of excess volume can in turn explain

the reduction of the enthalpy of formation of metal hydrides observed in experiments [93, 114].

The reduction of the enthalpy of formation is beneficial to the properties of hydrogen storage in metal hydrides and it is thus of primary importance to understand the relaxation process that removes the excess volume regions in the metal and metal hydrides over several hydriding/dehydriding cycles. In the next section, the parameters driving the nucleation of new grains and the growth of existing as well as new grains will be examined.

5.3.1 Nucleation of New Grains

In severely deformed materials, the recrystallization can be described as a nucleation and growth process [136]. We define nucleation as the formation of a crystallite of low internal energy growing inside or into a deformed material from which it is separated by a high angle grain boundary [136]. Growth is the process whereby a newly formed or preexisting crystalline grain increases its size by extending its boundary into the deformed region. Nucleation and growth are very complex phenomena and multiple attempts at describing them have been proposed in the literature [120, 136].

Because the kinetics of grain nucleation and grain growth are similar to that of a phase change at constant composition [136], we use a simple model for which the recrystallization associated with the excess volume is treated as a phase transition in a material between two phases having the same composition but different structures. The phase transition is described as a homogeneous nucleation followed by a diffusion-like growth occurring at the grain interface [59]. It must be mentioned that homogenous nucleation related to thermal fluctuations are considered unlikely by some people due to the energetics of the surface energy associated with

188

the formation of a small grain. More complex theories propose that grains are initially present in the sample as a result of early recovery in the material or that grains form on heterogeneous sites outside of the deformed region. Those early grains will be the center for primary recrystallization. This would not affect the outcome of the growth process though even if the density of critical nuclei could be affected. Nevertheless, the simplicity of a homogeneous nucleation model provides an idea about the energetics at play and how the excess free energy and entropy of the deformed regions can influence the formation of crystalline cores as well as their growth [136].

Let's assume that there is a molar excess free energy G_{ex} between the deformed region and the crystalline region and that the formation of a crystalline core within the deformed region generates an interface energy σ. At small radius for the crystalline core, the surface energy acts as an energy barrier that prevents the formation of the crystalline core because an increase in radius size leads to an increase in the free energy of the system. At larger radius though, the surface to volume ratio diminishes and the growth of the particles is favored by the large G_{ex} present in the deformed regions. The radius for which an infinitesimal increase in the nucleus size does not change the free energy is called the critical radius and it corresponds to the minimum size that a nucleus must have to be stable. The relative importance of σ and G_{ex} determines the critical radius and it leads to a temperature dependent steady state where the number of nuclei being formed per unit time equals the number of nuclei of critical size disappearing through growth or shrinkage [59]. Accordingly, the number of nuclei of critical size becomes:

$$N_{eq} = n_o \exp\left(-\frac{\overline{\Delta G}}{RT}\right) \qquad (5\text{-}13)$$

where n_o is the number of atoms per unit volume in the deformed phase and the molar nucleation critical free energy $\overline{\Delta G}$ that corresponds to the free energy needed to create a nucleus of critical radius is:

$$\overline{\Delta G} = \frac{16\pi\sigma^3 v^2}{3(G_{ex})^2} \qquad (5\text{-}14)$$

Here, v is the molar volume of the crystalline phase.

The energy barrier or activation energy ΔG_a for an atom or molecule to jump from the excess volume side to the crystalline side determines the rate at which a critical nucleus grows through the diffusion of atoms or molecules from the deformed region to the crystalline nucleus. The rate of crystallite nucleation with a radius of critical size is thus obtained by multiplying the number of nuclei of critical size by the rate of growth of such critical nuclei [59]:

$$I = K_N \exp\left(-\frac{\left(\overline{\Delta G} + \Delta G_a\right)}{RT}\right) \qquad (5\text{-}15)$$

In Eq. 5-15, K_N is a rate constant. In the above expression, the rate at which the crystalline nuclei disappear due to atoms in the crystalline state leaving for the deformed state is neglected for simplicity [59].

5.3.2 Crystal Growth of Grains

A similar approach can be used to determine the growth rate of crystalline cores within a deformed matrix. This will be used in the next section to determine how the excess entropy present in heavily deformed material could help slow down the relaxation process. Again, we look at the interface of a single crystalline core and analyze the atom transfer between the deformed state and the crystalline one. This time, the reverse reaction where an atom can leave the crystalline surface and return to the deformed region is accounted for. So the net rate transfer of atoms from the deformed region to the crystalline core per unit time becomes [129]:

$$\bar{r} = s v_o \exp\left(-\frac{\Delta G_a}{RT}\right)\left(1-\exp\left(-\frac{G_{ex}}{RT}\right)\right) \tag{5-16}$$

where s is the number of atoms at the surface of the crystalline nucleus and v_o is the rate at which an atom attempts to jump from one state to the other. If the distance ι between the crystalline core's outer layer and the first atomic layer of the amorphous region is known, the rate u of growth (m/s) becomes:

$$u = \iota v_o \exp\left(-\frac{\Delta G_a}{RT}\right)\left(1-\exp\left(-\frac{G_{ex}}{RT}\right)\right) \tag{5-17}$$

5.4 Results and Discussion

To maintain the metal and metal hydride in this destabilized state of high free energy/high enthalpy, their relaxation into a more stable crystalline state must be avoided over multiple hydriding cycles. This can be achieved if the metal/metal hydrides are both in a metastable state (local minimum in the free energy). If the two metastable phases are characterized by a similar excess volume, it could lead to multiple high temperature transitions between the metal and the metal hydride with a reduced probability of relaxation into the standard states. In this section, it will be shown that the conditions for stabilizing high enthalpy states can be obtained at high temperatures and high excess volume where the entropy contribution to the excess free energy can create a local minimum in both the metal and the metal hydride.

The molar excess free energy of Mg and MgH_2 is calculated at various temperatures using the guidelines presented in the previous sections. As in [135], the reference temperature is taken at room temperature where the experimental values of the bulk modulus and its first derivative with respect to pressure, the molar volume, the coefficient of thermal expansion, the heat capacity and other relevant parameters are all known for both the metal and its respective hydride (Table 5-1). For our calculations, the coefficients of thermal expansion were calculated using Eq. 5-10 which reduces the number of independent parameters that must be known. The results for the Mg/MgH_2 system are presented in Fig. 5-2. It is noted that in Fig. 5-2, the enthalpy contribution from the heat capacity is not included in the calculation of the excess free energy since it is a property that is independent of the state of excess volume. Thus, the contribution from the heat capacity to the enthalpy will not impact the relaxation rate of the

excess volume regions and should not be considered. In Fig. 5-2, $(\Delta G_a^{ex})_{Mg}$ represents the

energy barrier created by the entropy when Mg is in its metastable state at 700K.

Table 5-1. Parameters and constants used in the model.

Parameter	Value for Mg	Value for MgH$_2$
B_o	45 GPa [92]	55 GPa [140]
$(\partial B / \partial P)_o$	4.3 [141]	4.9 [140]
υ_0	1.38E-5 mol/m^3 [30]	1.81 E-5 mol/m^3 [30]
ΔG_a^o	92 kJ/mol [142]	
σ	0.46 J/m^2 [88] †	
L_f	8.48 kJ/mol [92]	&
L_s	128 kJ/mol [92]	&
C_v	25 J/mol-K [92]	40 J/mol-K [143]

† The interface energy between the amorphous region and the crystalline region is taken to be the same as the interface energy between two lattices that are out of registry.
& Because the decomposition of MgH$_2$ occurs below the melting point, we calculate its maximum entropy from that of Mg to which we add the entropy of the hydrogen gas.

As expected, the entropy associated with the large degree of disorder in the deformed regions

creates a local minimum in the free energy of both Mg and MgH$_2$ as the excess volume

approaches V_{crit}. In Fig. 5-2, the excess free energy for both Mg and MgH$_2$ at various

temperatures increases with excess volume because of the increasing excess enthalpy with excess

volume. As the excess volume increases, the negative entropy contribution to the free energy

eventually starts to dominate the positive enthalpy contribution and a maximum in the excess

free energy is reached. As the excess volume keeps increasing, the maximum excess entropy is

eventually reached and the enthalpy contribution to the free energy starts to dominate again until

the Gibbs instability is reached. This interaction between the enthalpy and entropy creates a

local minimum in the excess free energy of both the metal and the metal hydride. The minima

could render both materials metastable with respect to the crystalline phase if the energy barrier

created by the entropy is large enough to prevent nucleation and crystal growth in the deformed

regions (see Fig. 5-2).   When the excess volume is larger than the one corresponding to the excess free energy maximum, the entropy-generated energy barrier for a given excess volume and temperature is calculated by taking the difference between the excess free energy maximum and the excess free energy at a given excess volume.
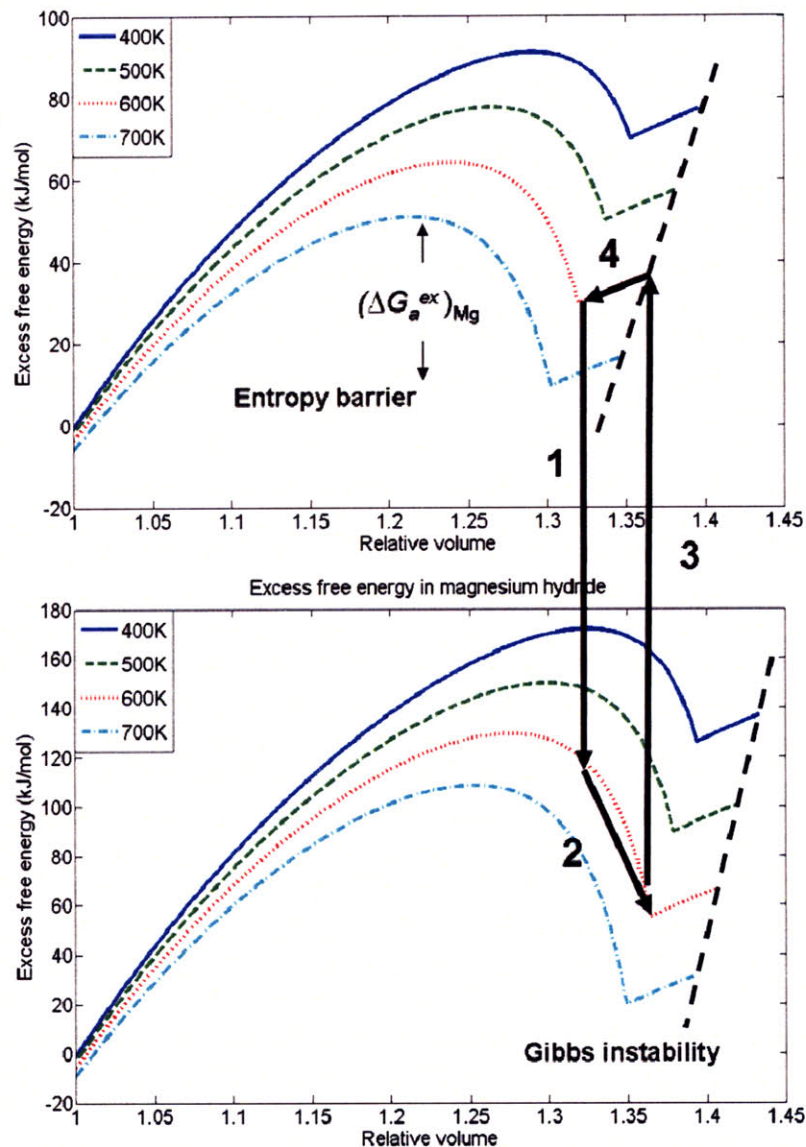
Figure 5-2. Top: excess free energy in Mg as a function of the relative volume at various temperatures. Bottom: excess free energy in MgH$_2$ as a function of the relative volume at various temperatures.

If both the metal and the metal hydride are stuck in a metastable state characterized by roughly the same excess volume, then Fig. 5-2 shows how it could become possible for the system to retain its destabilized state over repeated cycling by transitioning between the metal and the metal hydrides while maintaining a state of high excess volume. In Fig. 5-2, the black arrows show such a possible hydriding/dehydriding cycle in the Mg/MgH_2 system: 1) Starting from the lowest metastable Mg state at high excess volume, Mg hydrides into MgH_2 at constant excess volume. 2) Since the exact values of the excess volumes corresponding to the metastable state differ slightly in Mg and MgH_2, the metal hydride would then relax toward its true metastable state as a result of thermal fluctuations and remain in that state. 3) Heating up the hydride would lead to the release of hydrogen at constant excess volume and bring the system close to the Mg metastable state at high excess volume. 4) The Mg would finally relax toward its metastable state and the cycle can start over.

This illustrates how the entropy-generated energy barriers in any metal/metal hydride system could allow a destabilized system with a lower enthalpy of formation to maintain its improved thermodynamic properties by preventing both the metal and the hydride from relaxing into their more stable crystalline state. Such a transition between metastable states remains possible as long as the entropy-generated energy barriers are high enough and the excess volumes corresponding to the metastable metal and the metastable metal hydride are close to overlapping. The overlapping ensures that the transitions between the metal and the metal hydride during the hydriding/dehydriding reactions do not bring either material over or to close to the energy barrier maximum which would allow either material to relax toward its crystalline state. It is also important that the excess volume corresponding to the metastable state of either the metal or the

hydride be smaller than the critical volume of the other material. This ensures that the transition at constant excess volume between the two materials is physically possible. In Fig. 5-2, we see that this condition is barely satisfied for the Mg/MgH_2 system.

The location of the minimum in the free energy associated with the entropy content and the energy barrier preventing the relaxation of the deformed regions is very sensitive to the value of the maximum entropy. For a given material, if the maximum entropy is too small, then the free energy barrier associated with it will be very shallow and thermal fluctuations could more easily push the material over the energy barrier and back toward its crystalline state. On the other hand, if the maximum entropy of a material is too big, then the free energy barrier will be extremely deep but its minimum will be too close to the Gibb's instability. This could render oscillations between the metastable states of the metal and the metal hydride impossible if the minimum in the free energy of the hydride has a larger V_{ex} than the critical volume of the metal, or vice versa.

To better understand how an entropy-generated free energy barrier can affect the stability of a deformed region characterized by an excess volume, we looked at the relaxation process between the deformed regions and their crystalline state. The recrystallization rate of deformed regions is quantified by comparing the nucleation rate (see Eq. 5-15) and growth rate (see Eq. 5-17) of the critical nucleus subject to an excess volume at various temperatures (see Fig. 5-3 and Fig. 5-4).
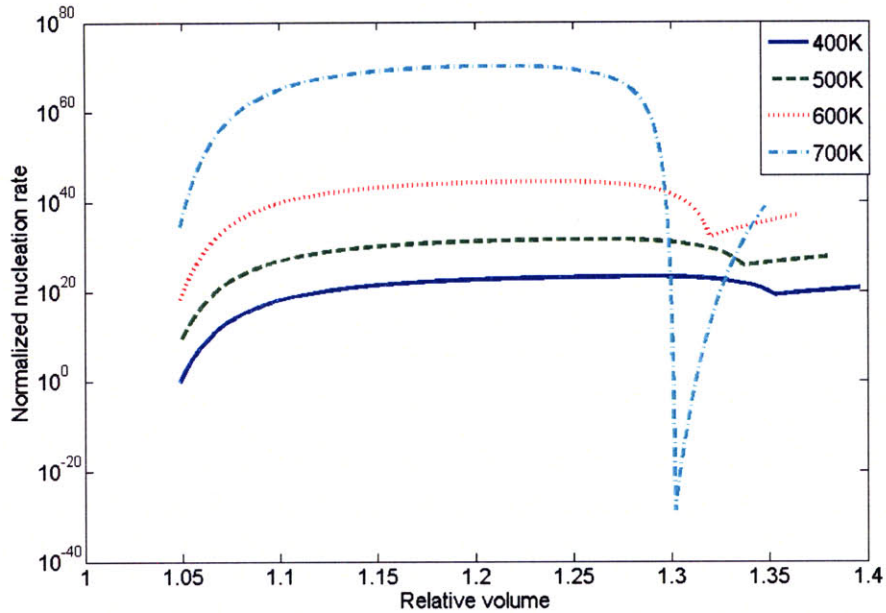
Figure 5-3. Normalized nucleation rate for Mg at various temperatures.

Figure 5-3 shows the ratio of the nucleation rate for various temperatures to the nucleation rate at $V_R = 1.05$ ($V_{ex} = 0.05$) and $T = 400$K as a function of the relative volume in the case of Mg. We chose $V_R = 1.05$ as the reference excess volume since the nucleation rate is not defined for $V_R = 1$ and we are interested to see how an increase in excess volume affects the nucleation rate. For the calculations, the activation energy ΔG_a (see Eq. 5-15) is modified to take into account the entropy related energy barrier ΔG_a^{ex} that the atoms must cross to move from a state of high excess volume to the crystalline state (see Fig. 5-2). The activation energy ΔG_a will thus have a component ΔG_a^o related to the activation energy for grain boundary migration in crystalline Mg (92kJ/mol [142]) to which the entropy-generated free energy barrier ΔG_a^{ex} is added (see Fig. 5-2):

$$\Delta G_a = \Delta G_a^o + \Delta G_a^{ex} \qquad\qquad (5\text{-}18)$$
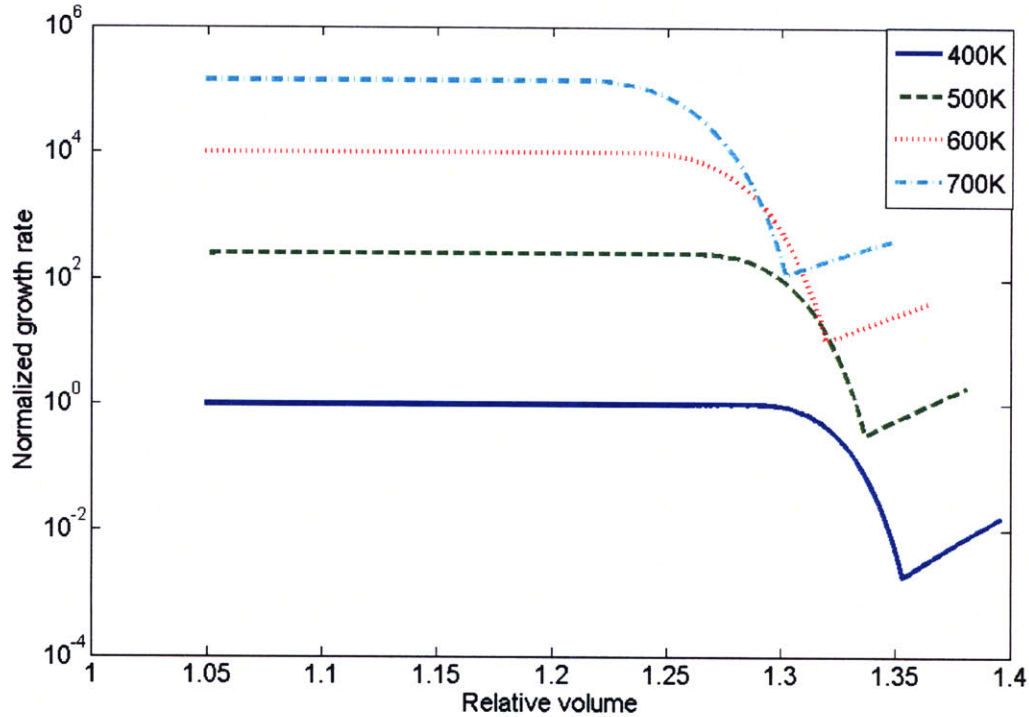
Figure 5-4. Normalized growth rate of a Mg crystalline nucleus at various temperatures.

The impact of the entropy is also incorporated into Eq. 5-15 through its impact on $\overline{\Delta G}$ (see Eq. 5-14). It must be mentioned that exact calculations of the nucleation rate would require a better knowledge of the dependence of ΔG_a^o and σ on V_{ex} and T. For the present calculations, it is assumed for simplicity that the activation energy ΔG_a^o and the interface energy σ are independent of excess volume and temperature. From Fig. 5-3, one can see that for small to moderate excess/relative volumes, a higher temperature will lead to a higher nucleation rate since thermal fluctuations will help overcome the energy barriers. For high excess volumes though, the energy barrier associated with the excess entropy becomes more important and the nucleation rate is reduced by several orders of magnitude. At high temperatures, the entropy barrier

198

becomes so large (see Fig. 5-5) that the nucleation drops dramatically to a point where nucleation could become highly improbable. Figure 5-5 shows the relative importance of the different energy terms at play for recrystallization in the case of Mg. At low excess volumes, the grain boundary migration energy barrier dominates and the nucleation rate tends to be fairly constant for a given temperature. As the excess volume increases, the entropy related energy barrier rapidly increases and the nucleation rate drops for all temperatures. Figure 5-4 shows the ratio of the growth rate of a crystalline nucleus to the growth rate at $V_R = 1.05$ and $T = 400K$ as a function of the relative volume for various temperatures in the case of Mg. The growth rate of a nucleus of size larger than the critical size is governed by Eq. 5-17. The first term in Eq. 5-17 tends to reduce the reaction rate and is related to the energy barrier associated with the transfer of one atom from the deformed region to the crystalline region. The second term in Eq. 5-17 expresses the tendency of the deformed regions to recrystalize and its magnitude is driven by the excess free energy present in the deformed region. Because of the large values of excess free energy involved in regions containing excess volume, the second term in Eq. 5-17 is almost equal to 1 for all values of relative volume greater than 1.05. So at low excess volume, the growth rate is fairly constant because it is dominated by the fixed grain boundary diffusion energy barrier (see first term of Eq. 5-17). As the entropy energy barrier increases, its contribution is added to the energy barrier associated with the grain boundary migration and the growth rate drops significantly. This shows that regions constraining large excess volume are much more stable to crystal growth than the regions with lower excess volume as was the case for the nucleation rate.
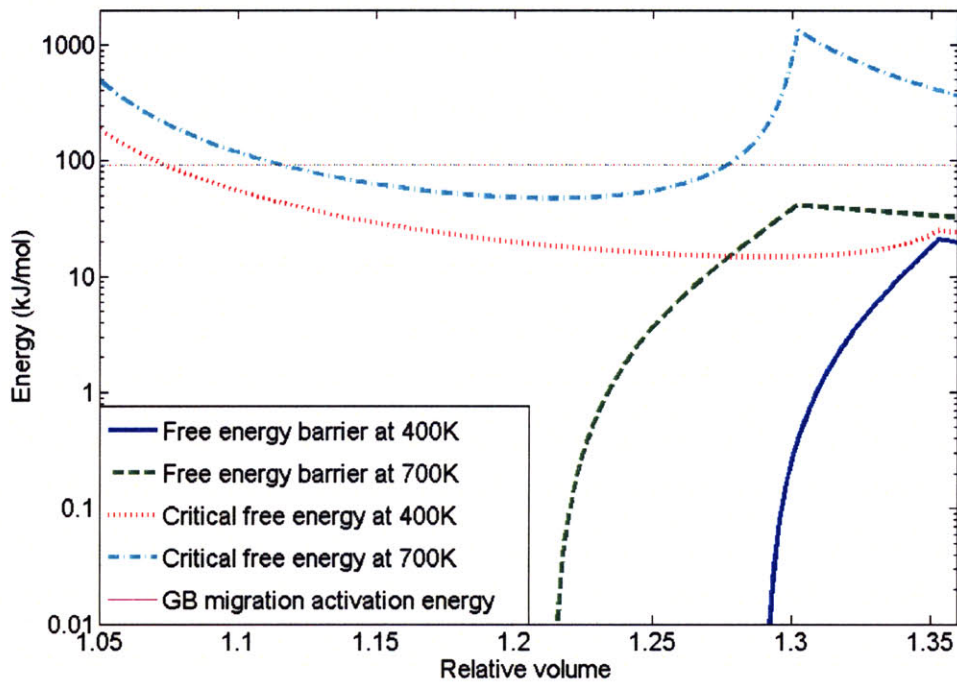
Figure 5-5. Different activation energies involved in the recrystallization process as a function of the relative volume at various temperatures.

In [93], it was shown that different volume fractions and excess volume values could reproduce the same experimental results on the reduction of the enthalpy of formation. In [135], we concluded that for a given reduction of the enthalpy of formation attributed to the presence of regions characterized by an excess volume, it is more beneficial to have a large fraction of the material in a state of small excess volume instead of having a small fraction of the material in a state of large excess volume. This choice reduces the negative impact of a temperature increase on the enthalpy of formation of metal hydrides and can even further destabilize a metal hydride if it possesses large regions of sufficiently small excess volumes. From a stability perspective, we have seen in chapter 5 that regions containing larger deformations could be several orders of magnitude more stable to nucleation and relaxation than regions of small excess volume, even at

high temperature. This larger stability of regions of high V_{ex} means that for a given reduction in the enthalpy of formation associated with an excess volume in the metal and the metal hydride, it is favorable to have a smaller fraction of the material in a large state of excess volume since this would allow the system to retain its reduced enthalpy of formation through more hydriding cycles. There is thus a compromise that would need to be made between higher stability and lower enthalpy of formation. Nevertheless, results in [135] suggest that even at high temperature, the reduction of the enthalpy of formation is still considerable compared to the standard enthalpy of formation. The smaller reduction in the enthalpy of formation thus seems to be an acceptable price to pay for the increased stability of the deformed regions responsible for the destabilization. This situation is another great example that compromises need to be made between the different properties needed for a material to meet the DOE's targets for hydrogen storage for automotive applications. Our results also show that a better understanding of the properties of nanomaterials is essential if one wants to design a system with properties that are optimal for commercial hydrogen storage applications.

5.5 Summary

The excess enthalpy present in both the metal and the metal hydride due to deformations results in an excess free energy that could lead to the relaxation of the materials into their more stable crystalline phase over many high temperature hydriding/dehydriding cycles. The relaxation would then result in the loss of the thermodynamic advantages associated with the nanostructuring of the material. However, at the high temperature associated with the hydrogen

release from the metal hydride, the excess entropy present in the deformed regions containing excess volume can generate a metastable state by reducing the excess free energy of the deformed region at high excess volume. The energy barrier at high excess volume created by the excess entropy inhibits the recrystallization rate in both the metal and the metal hydride by reducing the nucleation and growth rate of the crystalline core by several orders of magnitude. If the excess volume corresponding to the metastable state is approximately the same for the metal and the metal hydride, it thus becomes possible for the metal/metal hydride system to remain in its destabilized state over multiple hydriding/dehydriding cycles. Such a transition between the metastable states maintains the metal/metal hydride system in the favorable state of low enthalpy of formation that can improve the sorption/desorption kinetics of hydrogen, lower the hydrogen release temperature, and improve the system's energy efficiency by facilitating heat management.

The larger stability of regions of high V_{ex} also means that for a given reduction in the enthalpy of formation associated with an excess volume in the metal and the metal hydride, it is favorable to have a smaller fraction of the material in a large state of excess volume since this would allow the system to retain its reduced enthalpy of formation through more hydriding cycles. Although regions containing excess volume have been observed experimentally, a good understanding of how to generate those regions using mechanical or chemical treatments is still elusive. Strong control of the excess volume and the excess volume fraction that could be generated in a given material by a given mechanical treatment would allow us to design materials with controlled thermodynamic and kinetic properties. It would also be of interest to study experimentally the thermodynamic properties of deformed regions in order to better understand how to best model them using accurate EOSs. To reach these goals, methods that can

better characterize the excess volume and excess volume fraction present in a deformed sample must be developed. Such characterization methods would open the door to a much advanced understanding of the impact of nanostructuring on the properties of metals and metal hydrides and would pave the way to the design of optimized nanostructures that meet the DOE's objectives for hydrogen storage for automotive applications. Experimental results using two characterization tools that can be used to study metal hydrides are given in chapter 6 of this thesis.

6 Characterization of the Properties of Ball Milled Metal Hydrides

We have shown that the presence of deformations and defects including excess volume can lead to significant changes in the storage properties and thermodynamic properties of metal hydrides. The exact nature of the deformation, particularly in the case of excess volume can have a dramatic impact on some properties such as the enthalpy of formation of the metal hydrides. To determine whether the presence of excess volume will have a positive or negative impact on the thermodynamic properties of a metal hydride, the exact distribution of excess volumes and their corresponding volumetric fraction must be known. For the case of Mg/MgH_2, we have seen that for a given reduction in the enthalpy of formation, a large fraction of a metal hydride in a state of small excess volume would exhibit a further reduction of the enthalpy of formation as the temperature is increased but would not be overly stable against recrystallization. On the other hand, a material for which a small fraction is in a state of high excess volume would have increased stability against recrystallization while exhibiting an increase in its enthalpy of formation as the temperature is increased. The analysis would be opposite for a system such as Ti/TiH_2.

To build hydrogen storage systems with the desired properties, it is thus important to develop ways to nanostructure certain materials in a controlled fashion so that the desired structures can be generated in the required concentration. As mentioned before, a popular way to generate nanomaterials is through the use of ball milling. While it is known that milling parameters such as the specific rotation used, the size and types of balls used and the milling period can have a dramatic impact on the nanostructures type and size distribution, an exact understanding of how to generate the desired nanostructure using this method is still unknown. To develop this expertise, scientists must work in parallel with engineers to better control the milling process and to develop characterization tools that can provide feedback on the types of nanostructures produced as well as their properties. In the following, we will present the work that has been done using a transmission electron microscope (TEM) and Raman spectroscopy as examples of ways to characterize the structure and thermodynamic properties of ball milled metal hydrides. The advances and main challenges associated with these methods will be given.

Our objective is to develop experimental methods that are best suited to explore the benefits of nanostructuring and to characterize the impact of certain mechanical treatments on representative samples. For automotive applications, it is important to develop materials that can maintain their properties over multiple hydriding/dehydriding cycles. We have here developed a method that can study the phase transition temperature of nanostructured hydrides and study the cycle properties.

We first subjected commercial MgH_2 samples to different ball milling treatments in order to obtain samples with different size distributions and defect distributions. The samples were then analyzed using Raman spectroscopy to determine the impact of the ball milling procedure on the release temperature. We developed a special chamber that allows for the study of low pressure,

high temperature dehydriding conditions and the high temperature high pressure hydriding reaction. The conditions can be reversed continuously in order to study the system over multiple cycles. To obtain a qualitative estimate of the size distribution, samples were studied under the TEM that is equipped with a temperature-controlled stage to allow real time study of the hydrogen release reaction.

6.1 Background

In the sections 6.1.1 and 6.1.2, respectively, the basics of Raman spectroscopy and TEM experimentation are given, our experimental setup is presented and the results are discussed

6.1.1 Raman Spectroscopy

The Raman effect occurs when light impinges upon a molecule and interacts with the electron cloud of the bonds of that molecule. The incident photon excites one of the electrons into a virtual state. Figure 6-1 shows the two types of Raman scattering effects that can take place in a sample. For the spontaneous Raman effect, the molecule will be excited from the ground state to a virtual energy state, and relax into a vibrational excited state, which generates Stokes Raman scattering. If the molecule was already in an elevated vibrational energy state, the Raman scattering is then called anti-Stokes Raman scattering. The difference in energy between the incident photon and the Raman scattered photon is equal to the energy of a vibration of the

scattering molecule. A plot of intensity of scattered light versus energy difference is called a Raman spectrum [144].
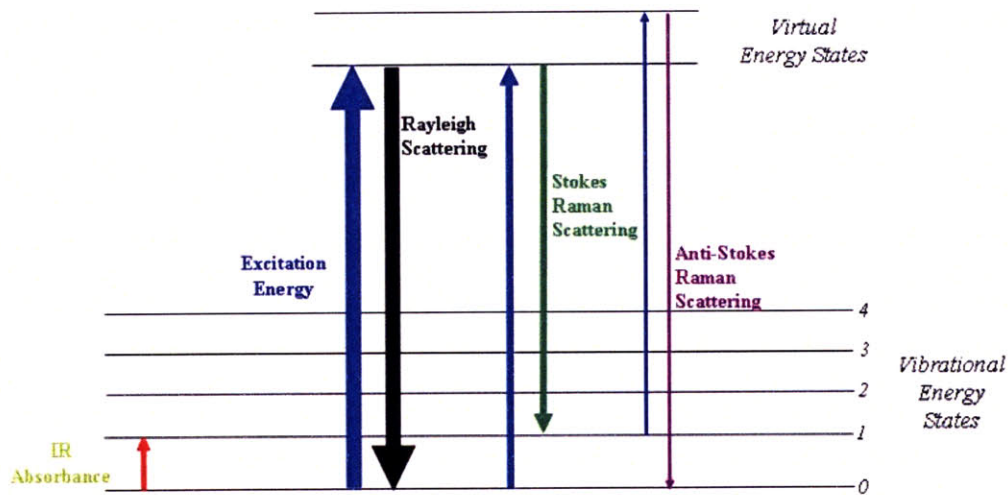
Figure 6-1. Simple representation of the Raman scattering process [144].

Numerically, the energy difference between the initial and final vibrational levels, $\bar{\nu}$, or Raman shift in wave numbers (cm^{-1}), is calculated through Eq. 6-1

$$\bar{\nu} = \frac{1}{\lambda_{inc}} - \frac{1}{\lambda_{sc}}$$

(6-1)

in which λ_{inc} and λ_{sc} are the wavelengths (in cm) of the incident and Raman scattered photons, respectively. The vibrational energy is ultimately dissipated as heat. Because of the low intensity of Raman scattering, the heat dissipation does not cause a measurable temperature rise in a

material but the absorbed incident light from the exciting laser can be as we will see in section 6.2.3.4.

At room temperature the thermal population of excited vibrational states is low, although not zero. Therefore, the initial state is the ground state, and the scattered photon will have lower energy (longer wavelength) than the exciting photon. This Stokes-shifted scattering process is what is usually observed in Raman spectroscopy.

A Raman spectrum is obtained for a material by measuring the multiple Raman shifts that a material exhibits for a given laser excitation energy. The different lines observed in the Raman spectrum give a signature for the material studied. The Raman spectrum is a function of the vibrational states of the material. The energy of a vibrational mode depends on the molecular structure and environment. Atomic mass, bond order, molecular constituents, molecular geometry and hydrogen bonding all affect the vibrational force constants which, in turn dictate the vibrational energy. Crystal lattice vibrations and other motions of extended solids can also be Raman-active. For that reason, spontaneous Raman spectroscopy is used, among other things, to characterize materials, measure temperature, and find the crystallographic orientation of a sample.

6.1.2 Transmission Electron Microscopy

Transmission electron microscopy (TEM) is a microscopy technique whereby a beam of electrons is transmitted through an ultra thin specimen, interacting with the specimen as it passes through it. An image is formed from the electrons transmitted through the specimen, magnified and focused by an objective lens and the image appears on an imaging screen.

Electrons have both wave and particle properties, and their wave-like properties mean that a beam of electrons can be made to behave like a beam of electromagnetic radiation. Electrons are usually generated in an electron microscope by a process known as thermionic emission from a filament, usually tungsten, or by field emission. The electrons are then accelerated by an electric potential and focused by electrostatic and electromagnetic lenses onto the sample. The transmitted beam contains information about electron density, phase and periodicity; this information is used to form an image.

Beam electrons are deflected by electrostatic interactions with the positive atomic nuclei and negative electron clouds of the sample. The scattered electrons are excluded from the transmitted beam by the objective aperture. Electron dense areas in the sample appear darker on the screen and on positive images.

Our TEM is equipped with an energy dispersive x-ray spectroscopy (EDS) system that can determine the elemental composition of the specimen by analyzing its X-ray spectrum or the energy-loss spectrum of the transmitted electrons. The TEM also has an integrated hot stage to control the temperature of the studied samples up to 1000°C. This is ideal to study in real time the dehydriding reaction in targeted nanostructures.

6.2 Characterization of the Metal Hydrides

This section presents results on the characterization of metal hydrides samples before and after ball milling.

6.2.1 Ball Milling

The commercial MgH_2 nanoparticles (Sample A) were obtained from Sigma-Aldrich (Product # 683043). To obtain different size distributions (that would be later characterized using Raman spectroscopy and the TEM), two separate samples were ball milled under separate conditions. A RETSCH PM100 commercial mill was used for the milling of the MgH_2 samples. In both cases, 10g of MgH_2 was placed in a 50cc sintered corundum jar (99% Al_2O_3) obtained from Glen Mills Inc (product number 1691-000238/1691-867002). Alumina balls of 0.5 inch in diameter were used as the grinding media to prevent contamination with the samples during the milling time.

Two separate samples were then generated. The first one (Sample B) was milled at 630rpm for 30 minutes with 2 minute breaks every 5 minutes interval to prevent local heating inside the jar that could have lead to unwanted dehydriding of the MgH_2. After each interval, the milling rotation was reversed to make the milling more uniform. The second sample (Sample C) was milled under the same conditions for a total of 150 minutes. In both cases, the samples were manipulated and processed inside a nitrogen-filled glove box to prevent contamination of the samples with oxygen and water. A portion of each of the three samples was placed in a sealed container filled with methanol having a purity exceeding 99.9% (Sigma Aldrich # 82762-10ML-F) to avoid contamination with water. The samples were later used to disperse nanoparticles on the TEM grid for size distribution analysis. The remaining samples were sealed and used for the Raman spectroscopy characterization.

6.2.2 TEM Characterization

Samples A, B and C were analyzed under the TEM to determine their approximate size distribution and the qualitative impact of ball milling the nanoparticles. Samples were prepared by diluting MgH_2 powders in methanol and sonicating the solutions for 25 minutes to separate the aggregated nanoparticles. A few drops of the sonicated samples were then deposited on TEM grids for observation. Energy dispersive x-ray spectroscopy was also performed for all three samples to determine whether the samples had been oxidized or contaminated. For all three samples, excluding the copper and carbon present in the TEM grid, the results show a maximum presence of 11.57% (atomic concentration) of oxygen and no other contaminants in concentrations exceeding 0.01%. This suggested that the samples were less than 12% oxidized for the worst sampling areas. Figure 6-2 shows typical images obtained for the 3 samples under the TEM: Top: Sample A; Middle: Sample B; Bottom: Sample C.

The size distribution was estimated using multiple images of a given sample (Fig. 6-2). While the exact distribution is hard to obtain from individual TEM frames, structural changes from one sample to the next as a result of milling can be readily observed. Table 6-1 shows a summary of the ball milling conditions and TEM results for these three samples.

Table 6-1. Results of the MgH$_2$ milling with alumina balls of 0.5 inch in diameter.

	Milling conditions	Size estimate	Comments
Sample A	As received	1-30μm	Mainly large particles
Sample B	30 minutes	0.2-5μm	Increased presence of fractures, smaller grains and sub-micron particles
Sample C	150 minutes	0.02-5μm	Abundance of particles smaller than 100 nm. Rare occurrence of large particles. Increased milling tends to aggregate the small ones into clusters.
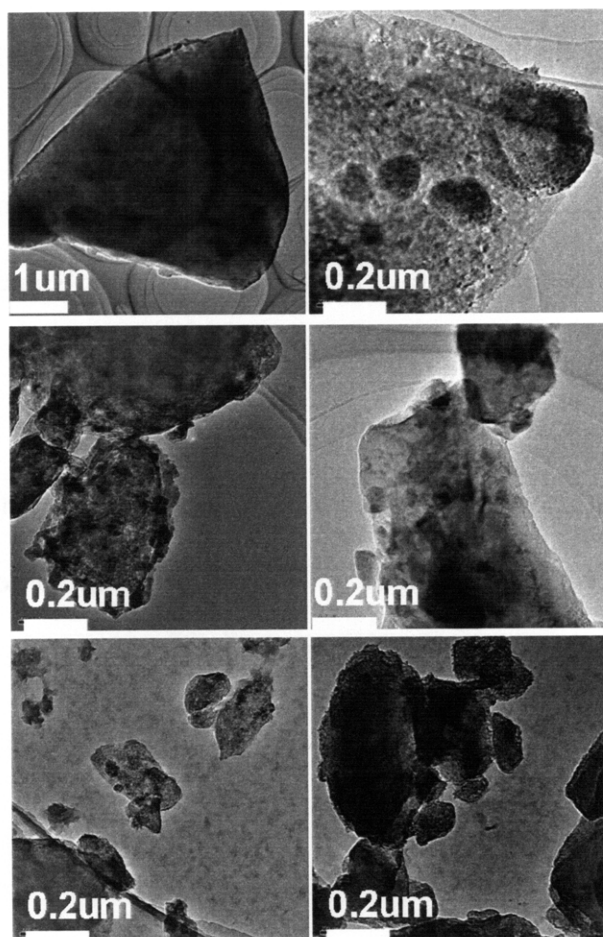
Figure 6-2. TEM images of Top: sample A; Middle: sample B; Bottom: Sample C.

The TEM can also be used to study in real time the hydrogen release from the sample. We equipped the TEM with a heating stage that allows for a control of its temperature to well above the hydrogen release temperature in MgH_2. The impact of certain defects on the release temperature can then be directly investigated by noting at which temperature the phase transition occurs in the metal around certain defects. The phase transition becomes visible because of the change from a rutile structure toward a hexagonal structure that is characteristic of Mg and a volume contraction on the order of 30% during the dehydrogenation.

In the case of MgH_2, the observation of the release temperature under the TEM poses significant challenges, the main one being the decomposition of the sample due to electron beam generated heating and oxidation. The oxidation problem was resolved by using a glove box and a carrier container for the sample holder between the glove box and the TEM chamber. A more significant problem that arises with the direct observation of MgH_2 under the TEM is the electron beam interaction with the sample that drives the decomposition of the hydride even at low temperatures. Prevention of an electron beam-driven decomposition reaction would demand the use of cryogenic temperatures which, in turn, would not allow us to investigate the high temperature phase transition. We believe that this issue could be resolved by the investigation of metal hydrides that are resistant to the electron beam.

6.2.3 Raman Spectroscopy Characterization

We designed an experimental Raman spectroscopy system to study the properties of metal hydrides. Raman spectroscopy was chosen for its sensitivity to the phase, the crystalline structure, the size distribution and the temperature of the samples studied. Raman measurements

thus provide us with different characterization options for metal hydrides. Our system is summarized in Fig. 6-3. We used the CCD of a Nikon D70S as our collector, and we collected the images using Camera Control Pro 1.0.0. To avoid contamination with ambient air and to allow for a temperature and pressure control around the samples, a Smart Collector (0031-9XX) equipped with a Temperature Controlled Environment Chamber (0019-037) (see Fig. 6-4) from Thermo Fisher Scientific was used. To allow for the focusing of the 532 nm laser excitation wavelength (2.33eV) on the sample inside the chamber, the sample chamber was modified to bring the sample closer to the emission-free window as shown in Fig. 6-4. The as-modified chamber can be pressurized or evacuated, and temperature control up to 800°C is provided by a USB Temperature Controller from Thermo Fisher Scientific (222-235400) in conjunction with temperature controlling software (TempSet V.1.2.2.2). This temperature and pressure control would allow us to study the hydriding/dehydriding reaction over multiple cycles by varying the hydrogen pressure and temperature conditions to induce the hydriding and dehydriding reactions alternatively.
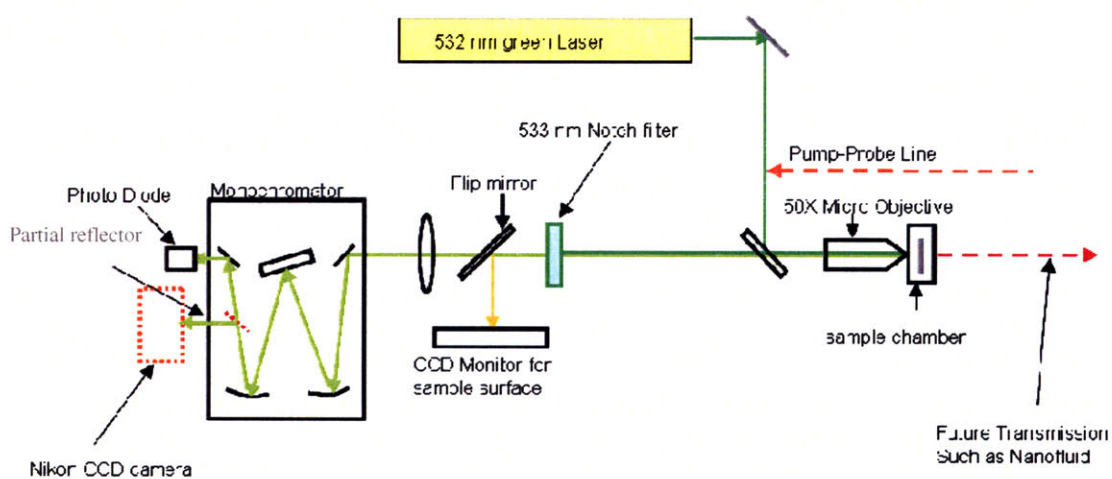
Figure 6-3. Set up for the Raman experiment. The sample chamber in the diagram represents the position of the Smart Collector.
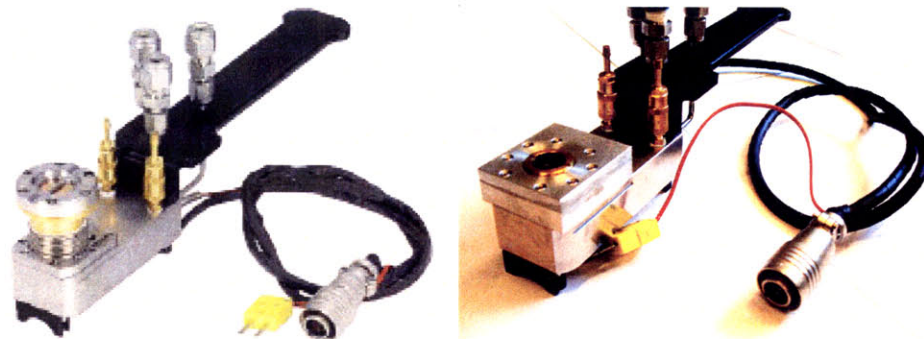
Figure 6-4. Smart collector. Left: as purchased. Right: as modified.

6.2.3.1   Results and Analysis

The Raman spectra of samples A, B and C were obtained using a laser intensity of 1000mW. The different optics in the laser path further reduced the laser power but the settings were kept constant between samples. The MgH_2 samples were taken out of the milling jar and placed in the sealed Raman chamber under a nitrogen environment in a glove box to prevent contamination and oxidation. The Raman spectra were then obtained using a 2 min exposure time at $10^{\circ}C$ temperature intervals to determine the release temperature profile of the hydrogen release. The samples were placed in a heating chamber under a constant 15psi environment of N_2 throughtout the entire length of the experiment to constantly flush the chamber from any moisture and oxygen and thus to prevent oxidation before the release temperature was reached.

Since the milled MgH_2 samples possess a wide binding site energy distribution for the hydrogen atoms, the release of hydrogen is expected to occur over a wide temperature range of $340-430^{\circ}C$, depending on the exact size distribution and structure of the hydride [93, 114]. A 5 min interval was also introduced every time the temperature reached a new plateau to allow for the reaction to take place. As discussed in [10] and chapter 2.3, a diffusion-limited desorption reaction in micron size particles takes place within 1 min. Consequently, time intervals of 5 min

215

were judged to be sufficient for nanoparticles to fully release their hydrogen after each new temperature increment.

6.2.3.2   Wavelength Calibration

The calibration of the CCD was obtained using a Si sample and by varying the central position of the monochromator between 532 nm (incident laser wavelength) and 562 nm. The relative positions of the laser beam on the obtained Raman spectra were than used to calibrate the range of wavelengths present in each Raman spectrum. In our experiments, we used a central position of the monochromator of 562 nm to fully show the two peaks present in the MgH_2 phonon spectra. When the obtained Raman spectrum were centered on 562 nm (in order to maximize the visibility of the Stoke part of the spectrum.), we found that each spectrum ranged from 501.5 nm to 580 nm.

6.2.3.3   Noise Reduction

To account for the background signal and noise generated by the optics in the laser path, the results were normalized to the Raman spectrum of Mg that was taken at all temperatures of interest. The normalization also removed the noise from the CCD window and also amplified the differences between the various spectral peaks that characterize the sample before and after the phase transition. Obtaining a clear difference in spectra before and after the phase transition is more important than obtaining an accurate spectrum for both phases because we are more interested in measuring a phase transition signature than measuring individual spectrum. The raw data was also filtered numerically using a low pass filter to remove unwanted fluctuations in the signal resulting from the pixels of the camera.

6.2.3.4   Temperature Calibration

The absorption of the laser light on the studied sample will create a local temperature increase on the sample. Since the thermocouple present in the sample holder is away from the laser spot, the laser generated temperature increase of the sample will not be recorded by the thermocouple and must be indirectly obtained. Moreover, the exact temperature increase resulting from a given laser power is highly dependent on the powder size distribution, porosity, grain size distribution and the presence of light-absorbing defects and impurities, all of which affect the effective thermal conductivity and the emissivity of the sample. For each sample spot that is analyzed, one must thus calibrate the exact influence of the laser beam.

From [145], we expect that the position of the Raman peaks characteristic of MgH_2 will shift linearly with temperature as a result of lattice softening caused by the thermal expansion. We also expect the width of the peak to increase linearly as a result of the relaxation of the Raman selection rules due to disorder and from quantum size effects. MgH_2 shows three characteristic peaks in its Raman spectrum. Two of them are noticeably strong (E_g = 113.6meV, A_{1g} = 158meV) [146] and can be used for temperature calibration (see Fig. 6-5). The third peak was too weak and could not be resolved reliably.

For each of the three samples, we recorded the Raman spectrum at constant laser power (1000mW) for various temperatures (see Fig. 6-5). The relative shift in the position of the E_g peak was noted as a function of the temperature indicated by the thermocouple. The linear regression results for the peak shift are presented in Fig. 6-6 where the temperature shift in the E_g peak is plotted as a function of temperature for the 3 samples of interest. Extrapolation to the temperature for which the shift in the Raman peak was predicted to disappear was then carried out and the laser contribution to the sample's temperature was taken as the difference between

the extrapolated value and room temperature (27°C). The results of the fit are listed in Table 6-2 and one can here see that the slope of the peak shifts as a function of temperature was constant between the samples. In Fig. 6-5, the indicated temperatures are as measured by the thermocouple and don't include the impact of laser heating. The data presented in Fig. 6-5 is that of sample C and the dotted vertical lines indicate the shift in the Raman peak position.
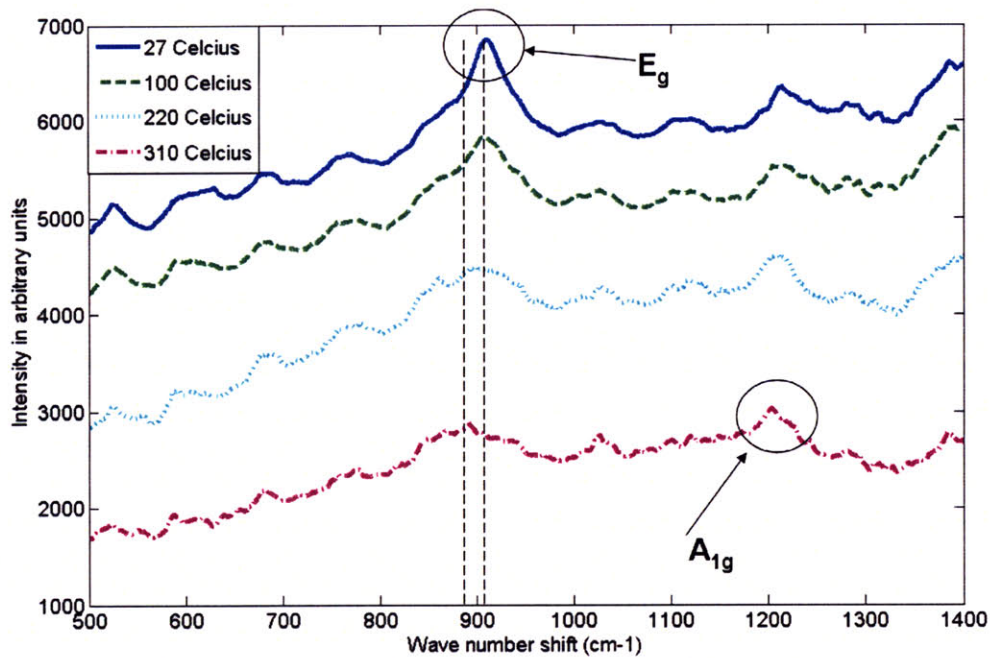
Figure 6-5. Temperature dependent shift in the Raman lines of MgH₂ for sample C. The dotted lines indicate the downshift of the peak frequency due to the laser heating of the sample by the laser.

The results from Table 6-2 show the importance of choosing the right laser power to excite the sample. The right power must be a compromise between minimizing the input power on the sample and obtaining a good signal-to-noise ratio. Since a laser power that is too high results in more local heating of the sample and a larger uncertainty about the release temperature, it is recommended to use a longer exposure time in combination with a lower power. Moreover, to

facilitate the comparison of results for the release temperature from different samples, the focusing microscope objective (see Fig. 6-3) should have a longer focal point to guarantee that the laser beam width will remain the same as the samples are changed and as the sample surface is moved due to thermal expansion. This guarantees that the impact of heating will be limited, but more importantly this guarantees a relatively constant heating for samples containing different particle size distributions that we need to compare.
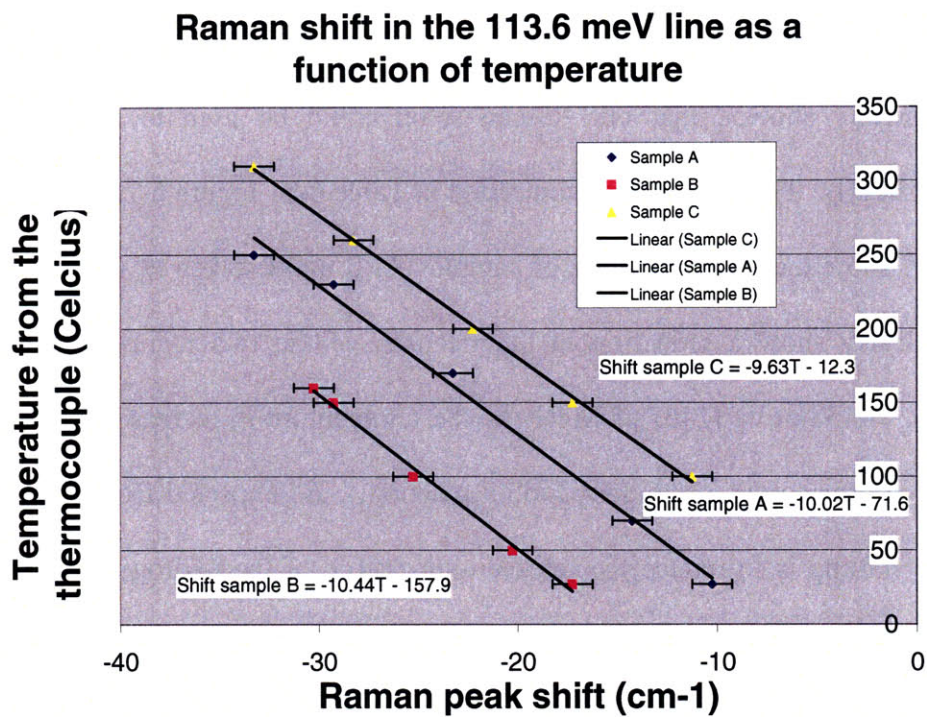
Figure 6-6. Peak shift as a function of temperature for samples A, B and C.

Table 6-2. Results of the temperature calibration and release temperature of hydrogen.

	Peak shift $(cm^{-1}/^{\circ}C)$	Laser induced temperature increase $(^{\circ}C)$	Thermocouple temperature range $(^{\circ}C)$	Adjusted release temperature $(^{\circ}C)$	Experimental [114] release temperature $(^{\circ}C)$
Sample A	-10±1	100±20	270-290	370-400 ±20	380-400
Sample B	-10±1	185±40	180-200	365-385 ±40	370-410
Sample C	-10±1	40±10	310-340	350-380 ±10	352-386

6.2.3.5   Observing the Hydrogen Release

We successfully showed that our Raman setup could be used to measure the release temperature of MgH_2. The results are summarized in Table 6-2. Figure 6-7, Fig. 6-8, and Fig. 6-9, respectively, show the Raman spectra of samples A, B and C taken at various temperatures. The spectra clearly show a reduction in the intensity of the two main Raman peaks ($E_g = 113.6meV$, $A_{1g} = 158meV$) [146] of MgH_2 as the temperature is increased. This decrease in signal intensity corresponds to the dehydriding reaction. As expected from [46, 93, 114], the impact of ball milling is to reduce the release temperature of the hydrogen. The onset of the hydrogen release was measured at $350^{\circ}C$ for sample C compared to $365\ ^{\circ}C$ for sample B and $370^{\circ}C$ for sample A. The reduction in release temperature is consequently more pronounced for sample C whose size distribution was significantly smaller than that of sample A and B. As mentioned in previous chapters, this temperature reduction is the result of the destabilization of the metal hydride caused by the introduction of grains, surfaces, interfaces, and potentially some γ-MgH_2 phase into the sample. The increased porosity and reduced particle size also help the release reaction by facilitating the diffusion of hydrogen in the solid and gas phases. In Table 6-2, the results for the release temperature are compared with experimental data from [114] for

comparable nanoparticle size distribution. While the uncertainty caused by the laser heating is high, the data show both a similar trend and a magnitude for the release temperature as a function of particle/grain size.
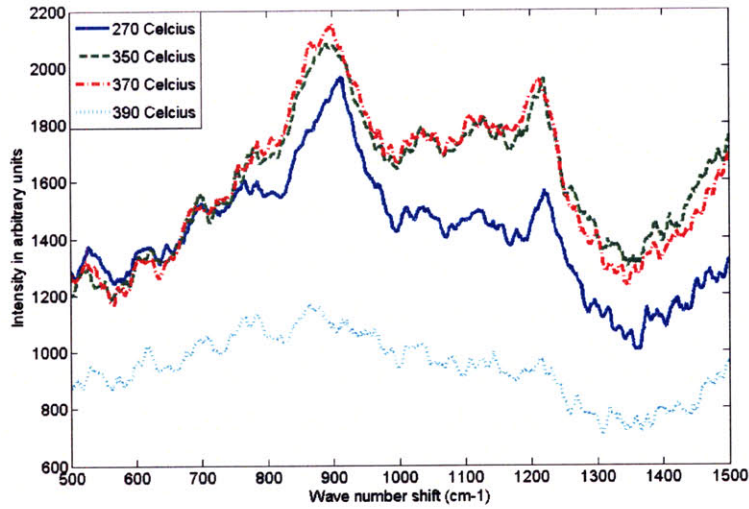
Figure 6-7. Raman spectra of sample A at various temperatures.
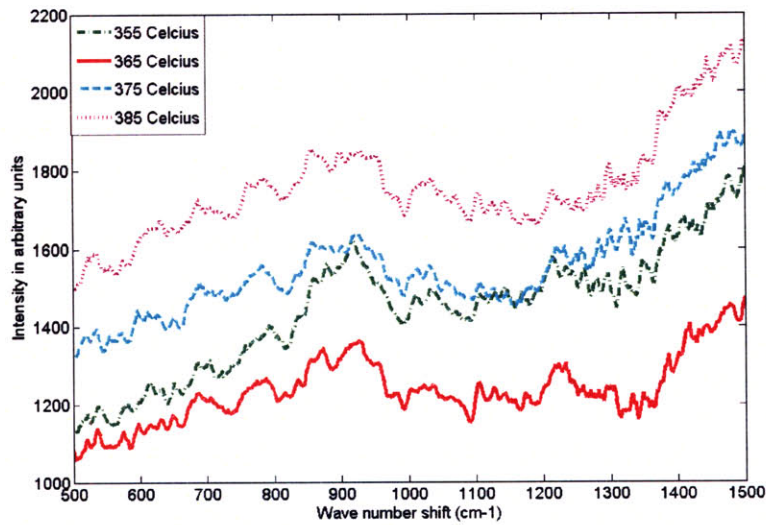
Figure 6-8. Raman spectra of sample B at various temperatures.
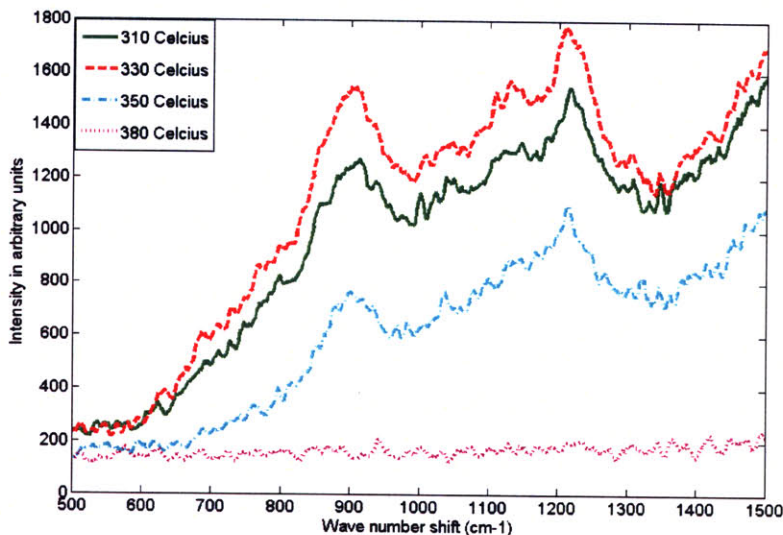
Figure 6-9. Raman spectra of sample C at various temperatures.

From the Raman spectra of all three samples, we can see that the clarity of the Raman peaks were much better in sample A and C than in sample B. We attribute the noisy signal in sample B to the laser heating that was much higher for sample B than for the other samples. This higher laser intensity could in turn have led to some non-uniform temperature distribution for this sample and a local triggering of the release reaction. For sample B, the noise in the signal also led to a larger uncertainty in the release temperature of the hydrogen because of the broadening of the peaks cause by the higher temperature of the sample. The broad peaks increase the uncertainty in the frequency shift of the Raman peaks with temperature which directly correlates to a larger uncertainty in the laser heating itself. These results exemplify the importance of minimizing the laser heating of the sample.

6.3 Conclusions

In this chapter we showed that the combination of TEM and Raman spectroscopy could be used to study the real time phase transition in metal hydrides and to evaluate the impact of nanostructuring on the release temperature. The pressurized chamber can be used to study the properties of metal hydrides over multiple hydriding/dehydriding cycles and to assess the stability of the generated nanostructures that are responsible for gains in the release properties of the hydrides. The simplicity and ease of use of the system makes it a perfect candidate for the fast screening of multiple samples and for the study of catalysts, doping agents, or specific nanostructures. The precise determination of the release temperature of hydrogen is directly related to the intensity of the local heating generated by the exciting laser. Minimizing the laser heating while maintaining a good signal-to-noise ratio is essential to increasing the accuracy of the system. Improvements in the calibration of the laser heating are also important to insure that the uncertainty in the temperature increase produced by the laser heating remains small compared to the absolute release temperature.

7 Summary and Future Work

The potential impacts of nanostructuring metal hydrides on their hydrogen storage properties (storage capacity, kinetics, and thermodynamic properties) were investigated. First, a simplified heat and mass transfer scale analysis was performed to predict practical system-level length scales that provide an adequate absorption rate to meet the DOE 2010 rate goals for hydrogen storage in metal hydrides. Modeling assumptions were compared to a one-dimensional hydrogen reactor simulation with good agreement.

Several potential mechanisms for the reduction of the enthalpy of formation observed in ball milled metal hydrides were identified. It was shown that the increased surface and grain boundary energy as well as the presence of metastable crystalline phase in milled hydrides could play a role in reducing the enthalpy of formation, but that the predicted magnitude is too small to account for experimental observations. Excess volume was identified as the key parameter to explain the reduction in the enthalpy of formation of nanostructured metal hydrides observed experimentally. Using three equations of state, the excess enthalpy present in the deformed regions characterized by an excess volume was calculated. The theory was applied to the Mg/MgH_2 system and the results suggest that the excess volume provides a plausible explanation for the experimentally observed change in thermodynamic properties.

Then, the temperature dependence of the excess enthalpy present in regions characterized by an excess volume was calculated for metals and metal hydrides. At high temperatures, the different contributions from the pressure-volume, heat capacity, entropy and work associated with the thermal expansion were studied separately and their magnitudes and signs were compared. It was found that the pressure-volume contribution opposes and dominates the other three contributions at both high temperature and excess volume, and that this contribution becomes the leading temperature dependent contribution to the enthalpy of a material. The conditions under which a temperature change will reduce the enthalpy of formation of metal hydrides were also given and the Mg/MgH_2 system was studied as an example. It was also demonstrated that the impact of temperature will be more favorable to a reduction of the enthalpy of formation if a large fraction of the metal hydride is in a state of small excess volume compared to a small fraction of the hydride in a state of high excess volume.

The excess entropy present in deformed regions of metals and metal hydrides characterized by an excess volume was also quantified using the equations of state. At high temperatures and high excess volumes, the excess entropy leads to a stabilization of the deformed regions with respect to multiple hydriding/dehydriding cycles. The impact of the energy barrier created by the excess entropy on the recrystallization rate of the deformed regions was quantified using a homogeneous nucleation and crystal growth model. At high temperatures and high excess volumes, due to the entropy generated energy barrier, metal hydride systems containing a large excess volume can have a recrystallization rate that is several orders of magnitude smaller than the recrystallization rates of regions containing low excess volume. This entropy stabilization can create a regime where the reduced enthalpy of formation of the metal hydride could be

maintained over multiple cycles because of the increased stability of the nanostructures responsible for the reduction in the enthalpy of formation.

Finally, an experiment to study the cycling properties of metal hydrides was designed using Raman spectroscopy and a transmission electron microscope (TEM). It was demonstrated that the release temperature of hydrogen could be accurately measured using the Raman spectroscopy and that the hydrogenation reaction could be observed as well. The possibility to study the impact of size distribution and milling method on the release properties of the hydride was also demonstrated using MgH_2 samples that were subject to different ball milling conditions. The size distributions of the nanoparticle samples were determined using the TEM and their composition was obtained from energy dispersive X-ray spectroscopy.

Controlled deformations leading to an excess volume in metal hydrides offer an attractive way to improve the hydrogen release temperature of metal hydrides by reducing their enthalpy of formation. At high excess volumes, the excess entropy present in the deformed region offers a way to stabilize the nanostructure against the recrystallization that occurs during the numerous hydriding/dehydriding cycles that would be needed for automotive applications. The degree to which each metal hydride is impacted by deformed regions is strongly dependent on its physical properties, and more research is needed to determine which type of metal or complex hydride would be better suited for this type of treatment. Density functional theory (DFT) would offer a good testing ground to first verify the accuracy of the UEOS for numerous types of hydrides having different chemical properties. DFT could provide an accessible way to determine if other EOSs would be more suited to predict the impact of excess volume on the thermodynamic properties, while a Car Parinello-based calculation could help understand the degree to which the

excess entropy could prevent relaxation toward a crystalline structure at the high temperature needed for the hydrogen release.

It would also be important to investigate the impact of heavy deformation on other important hydrogen storage properties, such as heat transfer, reaction kinetics and storage capacity. As the crystalline structure of the metal is compromised and numerous interfaces and defects are introduced, one should expect a significant decrease in thermal conductivity due to increased phonon scattering. Because a poor heat transfer puts an additional cooling load on the storage system, which ultimately reduces storage capacity and energy efficiency, it is important to understand the compromises between a lower enthalpy of formation and a reduced thermal conductivity in deformed metal hydrides. Moreover, heavy deformation will change the energy landscape of the metal hydride and broaden the hydrogen binding energy distribution within a metal. This will affect the storage capacity and release and a better understanding of this effect will be needed in practice to build an effective storage system. Desorption scanning calorimetry would offer a most convenient way to investigate the impact of the binding site distribution, since the broadening of the binding energy distribution would ultimately lead to a broadening in the hydrogen release temperature range.

Although regions containing excess volume have been observed experimentally, a good understanding of how to generate those regions using mechanical or chemical treatments is still elusive. Strong control of the excess volume and the excess volume fraction that could be generated in a given material by a given mechanical treatment would allow us to design materials with controlled thermodynamic and kinetic properties. It would also be of interest to study experimentally the thermodynamic properties of deformed regions in order to better understand how to best model them using accurate EOSs. To reach these goals, methods that can

better characterize the excess volume and excess volume fraction present in a deformed sample must be developed. Such characterization methods would open the door to a much advanced understanding of the impact of nanostructuring on the properties of metals and metal hydrides and would pave the way to the design of optimized nanostructures that meet the DOE's objectives for hydrogen storage for automotive applications.

Because of the additional research needed to fully understand the thermodynamic improvements suggested by this thesis work, one can hardly expect to see an immediate impact of this work on hydrogen storage in the automobile industry. As mentioned, a better control over the generation of the different nanostructures presented in this work is necessary to use them as the building blocks for the next metal hydride based hydrogen storage system. Nevertheless, this research shows a potential direction where scientists could look in order to find a major improvement in the storage properties of metal hydrides.

The research in the hydrogen storage field has remained mostly incremental over the last few years and revolutionary breakthroughs are still needed to meet the DOE's goals for hydrogen storage. This thesis, even if mostly theoretical, thus has the merit of proposing a brand new type of nanostructure that could help control the storage properties of metal hydrides. It also introduces the new concept of a structure-based stabilization of the nanostructures responsible for an improvement in the key metal hydride properties. This type of new paradigm is what is currently needed in the metal hydride research field to bring a second breadth to the developemt of the metal hydrides that we need for automotive applications.

In addition to potential improvements for hydrogen storage in metal hydrides, the key concepts of this work could benefit other areas of research. Many research areas of interest in nanotechnology are plagued by similar issues as those hindering metal hydrides. Those issues

are fundamentally related to the very nature of nanostructures. For example, a nanostructuring of the active components of fuel cells, batteries, and thermoelectric devices has been introduced in recent years to take advantage of the new physical and chemical properties that are typical of nanostructures. The improved chemical reactivity, better phonon scattering properties, or larger surface to volume ratios are all properties of nanostructures that are directily responsible for the recent improvements in the properties of thermoelectric devices, fuels cells and batteries. Unfortunatly, those improvements tend to rapidly disappear over time as the high operating temperatures of those devices forces the nanostructures to relax to a more stable bulk-like structure. Our research suggests that by chosing the right type of nanostructures and using them in an optimal regime, the relaxation rate of the nanostructures can be dramatically reduced so that the improved properties that are attributed to them can be maintained over a longer period of time. This also suggests that the exact nature of the nanostructures employed should be carefully examined since improvement in a material that results from its nanostructuring can come at the expense of some more fundamental properties. The key concepts that emerged as a result of this work thus can have a potential impact that reaches much further than the field of hydrogen storage. The new concepts developed in this thesis are at the core of maximizing the improvements that one can hope to extract out of nanoengineering based on materials optimization.

Many of the recent advances in hydrogen research are still at an early stage of developement with further progress in understanding and in materials performance expected in the near term. Applications to industrial products are expected to follow. Let us assume for the sake of discussion that this does occur. First, niche markets such as for small-scale electronics could be targeted and the experience gained from those ventures would facilitate the transition into other

large scale markets such as the automobile markets where most of the economic and environmental impact can be made. Then as the technologies become even more mature and better understood, other markets with higher security and performance requirements such as the airline industry could be penetrated. The transition from an oil-based industry to an economy where hydrogen will play a larger role must thus be approached strategically in a way where the technological and social advancements from each milestone can be used to reach the subsequent milestone. As the technologies needed for a large scale usage of hydrogen are developed, measures should be taken to promote the acceptance of a hydrogen economy by the general public. Recent studies amongst students, state officials, the general public, and the potential end users of hydrogen show that many misconceptions about the safety or about the physical properties of hydrogen are still common. Those studies also reveal that there exists an inverse correlation between the will of people to accept hydrogen as an energy carrier and the level of their knowledge about hydrogen [147]. As we transition to a hydrogen economy or as hydrogen starts penetrating small niche markets, it will thus be important to put in place programs to educate the different segments of the populations that will be exposed to hydrogen. A joint effort between private companies and the government is most likely to be the best approach to reaching such a goal.

Because of its special and unique attributes, hydrogen is likely to be one of a mix of future sustainable energy technologies. New materials and nanoscience are necessary for the development of the potential of this technology as they are for the future development of many of the other pertinent energy technologies. The strong interplay between basic and applied sciences, interdisciplinary approaches and the coupling between theory and experiment are all vital. Working closely with industry will be important for identifying research directions with

high potential impact. Finding niche markets for early hydrogen technology and bringing those technologies to market will further increase R&D investment from the private sector which will see the possibility for profit. The development of those niche markets would also help develop the infrastructure needed for a hydrogen economy and allow some of the cost to be carried by private investors. Attention to major advances in other key technologies is equally important for the identification of new priority directions for hydrogen R&D. Because of the highly complementary focus of energy research in different countries, based on their different climatic and cultural constraints, international cooperation and networking should be encouraged and supported. Linking to and coordinating between international groups promoting materials research for energy applications regionally and internationally would be important, so that policy makers worldwide get a clear message about progress in hydrogen research and its potential contribution to the larger picture of providing a sustainable energy supply world-wide.

Developing sustainable energy technologies that can have a major impact and implementing them will require much effort. The Lisbon declaration of the World Materials Summit [5] highlights key steps that must be addressed to ensure a smooth and successful transition to new energy technologies. It highlights the importance of

1. Strategic planning (roadmaps) in the development of new and improved materials and the products for future energy technologies.

2. Bringing together leading academic, public sector and industrial scientists to discuss important technical issues and to ensure that key problems are tackled in a swift and effective manner.

3. Identifying and training a new generation of young international leaders.

4. Promoting major new international collaborative materials research programs relevant to future energy technologies.

5. Providing information to global, regional and national policy makers, and to investment analysts in the energy sector.

6. Ensuring that manufacturers in the energy sector, especially small and medium enterprises, have the best possible access to information related to innovative materials developments.

7. Interfacing with other key international organizations relevant to the energy sector.

8. Stimulating public interest in, and awareness of, energy-related issues.

9. Attracting and nurturing the young generation of scientists and engineers to meet the mega challenge of clean energy sustainability and growth through providing a clear picture of the challenges, opportunities and career paths for energy-related research.

Implementing major changes in our energy consumption habits will demand much more than breakthrough technologies. It is a challenge that will take time and the systematic commitment over time of the academic, private, and public sectors. This is why communication between the different sectors is important for sharing specific needs and knowledge which will ultimately accelerate technology development and implementation.

As shown in Table 1-2, structural or chemical changes associated with nanoengineering can improve several performance requirements of metal hydrides for hydrogen storage but others show a reduction in performance. For example, small particle size and grain boundaries facilitate the absorption kinetics but impair heat transfer. Strain helps hydrogen diffusion in the α phase but it reduces the maximum hydrogen uptake and hinders the diffusion at the α-β boundaries. An integrated approach that addresses the main DOE goals simultaneously is

essential to develop hydrides for practical storage applications. A hydride with a somewhat reduced adsorption but faster kinetics and higher thermal conductivity may be more favorable than higher capacity hydrides with a slow desorption kinetics and high hydrogen desorption temperature. For on-board transportation applications therefore, trade-offs in performance involve a choice between sustainable power and sufficient range.

Table 1-1 and Table 1-2 show the advances achieved through nanotechnology for kinetics and release temperature, as well as the substantial progress required to meet the DOE goals. The improvement in kinetics, release temperature, and cyclability are clearly lagging behind the achievements in volumetric and gravimetric densities. Some change in research focus, therefore, may result in better overall performance with our present knowledge base. Although incremental progress may be achieved by pursuing well-established routes, new approaches and basic research are needed to produce the real breakthroughs required to meet the DOE goals.

Significant fundamental research remains to be performed to overcome the gap between present capabilities and hydrogen storage needs. Hydrogen diffusion and bonding in metals and interaction with catalysts need to be further investigated to explain the physical mechanisms underlying the currently observed enhancements and to predict the amount of improvement that might be possible at the nanoscale. The origin of the destabilization produced by alloying and doping must be understood at the electronic level in order to efficiently design compounds with desirable properties. Further developments in materials engineering are necessary to stabilize the high-energy structures (small particle, large grain boundaries, interfaces) that were shown to favor fast kinetics and low release temperatures. Incorporation of hydrides into functional frameworks or matrices with desired chemical and physical properties must also be investigated

more intensively. Such research is expected to generate new ideas and to lead to fundamental innovations in hydrogen storage technology.

BIBLIOGRAPHY

1. Dresselhaus M. *Basic research needs for the hydrogen economy.* Office of Basic Energy Sciences. US Department of Energy. http://www.sc.doe.gov/bes/hydrogen.pdf. Accessed: 8/1/06.
2. Dresselhaus M. 20006. Overview of the hydrogen initiative, Plenary talk, APS March 2006.
3. Bouza A, Read C J, Satyapal S, Milliken J. 2004. *Annual DOE Hydrogen Program Review.* Hydrogen, Fuel Cells & Infrastructure Technologies Program. US Department of Energy.
   http://www1.eere.energy.gov/hydrogenandfuelcells/pdfs/review04/st_1_miliken.pdf. Accessed: 8/1/06.
4. Koji Hashimoto, N. Kumagai, K. Izumiya, Z. Kato. 2007. Materials and technology for global carbon dioxide recycling for supply of renewable energy and prevention of global warming.
5. Declaration issued by the First World Materials Summit, Lisbon, Portugal 2007 http://www.spmateriais.pt/LISBON%202007%20DECLARATION.pdf.
6. G. W. Crabtree, M. S. Dresselhaus, and M. V. Buchanan. 2004. *Physics Today* 57(12), 39–44 . December.
7. Hoffmann P. 1981. *The Forever Fuel.* Westview Press: Boulder.
8. Bockris JO. 1999. Hydrogen economy in the future. *International Journal of Hydrogen Energy.* 24(1): 1-15. DOI: 10.1016/S0360-3199(98)00115-3.
9. Ogden JM. 1999. Prospects for building a hydrogen energy infrastructure. *Annual Review of Energy and the Environment.* 24: 227-279. DOI: 10.1146/annurev.energy.24.1.227.
10. Dornheim M, Eigen N, Barkhordarian G, Klassen T, Bormann R. 2006. Tailoring hydrogen storage materials towards application. *Advanced Engineering Materials.* 8(5): 377-385. DOI: 10.1002/adem.200600018.
11. Terzieva M, Khrussanova M, Peshev P, Radev D. 1995. Hydriding and dehydriding characteristics of mixtures with a high magnesium content obtained by sintering and mechanical alloying. *International Journal of Hydrogen Energy.* 20(1): 53-58. DOI: 10.1016/0360-3199(93)E0009-A.
12. Holtz RL, Imam MA. 1997. Hydrogen storage capacity of submicron magnesium-nickel alloys. *Journal of Materials Science.* 32(9): 2267-2274. DOI: 10.1023/A:1018572116447.
13. Gross KJ, Chartouni D, Leroy E, Zuttel A, Schlapbach L. 1998. Bulk and surface properties of crystalline and amorphous $Zr_{36}(V_{0.33}Ni_{0.66})_{64}$ alloy as active electrode material. *Journal of Alloys and Compounds.* 269(1-2): 321-326. DOI: 10.1016/S0925-8388(97)00476-3.

14. Liang G, Boily S, Huot J, VanNeste A, Schulz R. 1998. Hydrogen absorption properties of a mechanically milled Mg-50 wt.% $LaNi_5$ composite. *Journal of Alloys and Compounds*. **268**(1-2): 302-307. DOI: 10.1016/S0925-8388(97)00607-5.

15. Bououdina M, Fruchar D, Jacquet S, Pontonnier L, Soubeyroux JL. 1999. Effect of nickel alloying by using ball milling on the hydrogen absorption properties of TiFe. *International Journal of Hydrogen Energy*. **24**(9): 885-890. DOI: 10.1016/S0360-3199(98)00163-3.

16. Tessier P, Enoki H, Bououdina M, Akiba E. 1998. Ball-milling of Mg_2Ni under hydrogen. *Journal of Alloys and Compounds*. **268**(1-2): 285-289. DOI: 10.1016/S0925-8388(97)00585-9.

17. Abdellaoui M, Cracco D, Percheron-Guegan A. 1999. Structural investigation and solid-H_2 reaction of Mg_2Ni rich nanocomposite materials elaborated by mechanical alloying. *Journal of Alloys and Compounds*. **295**: 501-507. DOI: 10.1016/S0925-8388(99)00475-2.

18. Imamura H, Tabata S, Takesue Y, Sakata Y, Kamazaki S. 2000. Hydriding-dehydriding behavior of magnesium composites obtained by mechanical grinding with graphite carbon. *International Journal of Hydrogen Energy*. **25**(9): 837-843. DOI: 10.1016/S0360-3199(99)00105-6.

19. David E. 2005. An overview of advanced materials for hydrogen storage. *Journal of Materials Processing Technology*. **162-163**: 169-177. DOI: 10.1016/j.jmatprotec.2005.02.027.

20. Seayad AM, Antonelli M. 2004. Recent advances in hydrogen storage in metal-containing inorganic nanostructures and related materials. *Advanced Materials*. **16**(9-10): 765-777. DOI: 10.1002/adma.200306557.

21. Schlapbach L, Zuttel A. 2001. Hydrogen-storage materials for mobile applications. *Nature*. **414**(6861): 353-358. DOI: 10.1038/35104634.

22. Huot J. 2003. Nanocrystalline materials for hydrogen storage. In *Nanoclusters and nanocrystals*. Nalwa Hs (ed). American scientific publishers: California; 53-86.

23. Centrone A, Brambilla L, Zerbi G. 2005. Adsorption of H_2 on carbon-based materials: A Raman spectroscopy study. **71**:245406. DOI: 10.1103/PhysRevB.71.245406

24. Stan G, Cole MW. 1998. Hydrogen adsorption in nanotubes. *Journal of Low Temperature Physics*. **110**(1-2): 539-544. DOI: 10.1023/A:1022558800315.

25. Glasstone S. 1946. *Textbook of physical chemistry*, Van Nostrand Co: New York.

26. Defay R, Prigogine I. 1966. Surface tension and adsorption, Wiley: New York.

27. Vajo JJ, Mertens F, Ahn CC, Bowman RC, Fultz B. 2004. Altering hydrogen storage properties by hydride destabilization through alloy formation: LiH and MgH_2 destabilized with Si. *Journal of Physical Chemistry B*. **108**(37): 13977-13983. DOI: 10.1021/jp040060h.

28. Rusanov AI. 2006. On the material equilibrium of nanoparticles. *Nanotechnology*. **17**(2): 575-580. DOI: 10.1088/0957-4484/17/2/039.

29. Tolman RC. 1949. The effect of droplet size on surface tension. *Journal of Chemical Physics*. **17**(3): 333-337. DOI: 10.1063/1.1747247.

30. Wagemans RWP, Van Lenthe JH, De Jongh PE, Van Dillen AJ, De Jong KP. 2005. Hydrogen storage in magnesium clusters: Quantum chemical study. *Journal of the American Chemical Society*. **127**(47): 16675-16680. DOI: 10.1021/ja054569h.

31. Eckert J. 1995. Relationships governing the grain size of nanocrystalline metals and alloys. *Nanostructured Materials*. **6**(1-4): 413-416. DOI: 10.1016/0965-9773(95)00084-4.

32. Gialanella S, Lutterotti L. 2003. Nanocystalline metallic materials. In *Nanoclusters and nanocrystals*. Nalwa HS (ed). American scientific publishers: California; 1-52.

33. Wolf D. 1989. Correlation between the energy and structure of grain boundaries in b.c.c metals. I. Symmetrical boundaries on the (110) and (100) planes. *Philosophical Magazine B*. **59**(6): 667-680.

34. Rose JH, Smith JR, Guinea F, Ferrante J. 1984. Universal features of the equation of state of metals. *Physical Review B*. **29**: 2963-2969. DOI: 10.1103/PhysRevB.29.2963.

35. Ferrante J, Smith JR. 1985. Theory of the bimetallic interface. *Physical Review B*. **31**(6): 3427–3434. DOI: 10.1103/PhysRevB.31.3427.

36. Fecht HJ. 1990. Thermodynamic properties and stability of grain boundaries in metals based on the universal equation of state at negative pressure. *Acta Metallurgica et Materialia*. **38**(10): 1927-1932. DOI: 10.1016/0956-7151(90)90304-Y.

37. Fecht HJ. 1990. Intrinsic instability and entropy stabilization of grain boundaries. *Physical Review Letters*. **65**(5) 610–613 DOI: 10.1103/PhysRevLett.65.610.

38. Gertsman VY, Birringer R. 1994. On the room-temperature grain growth in nanocrystalline copper. *Scripta Metallurgica et Materialia*. **30**(5): 577-581. DOI: 10.1016/0956-716X(94)90432-4.

39. Porter DA, Easterling KE. 1992. *Phase transformations in metals and alloys*. Chapman & Hall: London; New York.

40. Benn RC, Mirchandani PK. 1989. Dispersion strengthening by mechanical alloying. In *New materials by mechanical alloying techniques*, Arzt E, Schultz L (ed.); Deutsche Gesellschaft für Metallkunde; 19-38.

41. Hondros ED, Seah MP. 1996. Interfacial and surface microchemistry. In *Physical metallurgy*, Cahn RW (ed), Haasen P (ed). Amsterdam ; New York : North-Holland. 1201–1289.

42. Valiev RZ, Islamgaliev RK, Alexandrov IV. 2000. Bulk nanostructured materials from severe plastic deformation. *Progress in Materials Science*. **45**(2): 103-189. DOI: 10.1016/S0079-6425(99)00007-9.

43. Doremus RH. 1985. *Rates of phase transformations*. Academic Press Inc.: New York; 149-157.

44. Zaluska A, Zaluski L, Ström-Olsen JO. 2001. Structure, catalysis and atomic reactions on the nano-scale: a systematic approach to metal hydrides for hydrogen storage. *Applied Physics A*. **72**(2): 157–165. DOI: 10.1007/s003390100783.

45. Zaluska A, Zaluski L, Strom-Olsen JO. 2000. Sodium alanates for reversible hydrogen storage. *Journal of Alloys and Compounds*. **298**(1-2): 125-134. DOI: 10.1016/S0925-8388(99)00666-0.

46. Zaluska A, Zaluski L, Strom-Olsen JO. 1999. Nanocrystalline magnesium for hydrogen storage. *Journal of Alloys and Compounds*. **288**(1-2): 217-225. DOI: 10.1016/S0925-8388(99)00073-0.

47. Zaluski L, Zaluska A, Strom-Olsen JO. 1999. Hydrogenation properties of complex alkali metal hydrides fabricated by mechano-chemical synthesis. *Journal of Alloys and Compounds*. **290**(1-2): 71-78. DOI: 10.1016/S0925-8388(99)00211-X.

48. Zaluski L, Zaluska A, Strom-Olsen JO. 1997. Nanocrystalline metal hydrides. *Journal of Alloys and Compounds*. **253-254**(1-2): 70-79. DOI: 10.1016/S0925-8388(96)02985-4.

49. Zaluski L, Zaluska A, Tessier P, Strom-Olsen JO, Schulz R. 1996. Nanocrystalline hydrogen absorbing alloys. *Materials Science Forum*. **225-227**(2): 853-858.

50. Zaluski L, Zaluska A, Tessier P, Strom-Olsen JO, Schulz R. 1995. Catalytic effect of Pd on hydrogen absorption in mechanically alloyed Mg_2Ni, $LaNi_5$ and FeTi. *Journal of Alloys and Compounds*. **217**(2): 295-300. DOI: 10.1016/0925-8388(94)01358-6.

51. Zaluski L, Hosatte S, Tessier P, Ryan DH, Ström-Olsen JO, Trudeau ML, Schulz R. 1992. *Metal–Hydrogen Systems*. M.R. Oldenbourg Verlag, Uppsala.

52. Aoyagi H, Aoki K, Masumoto T. 1995. Effect of ball milling on hydrogen absorption properties of FeTi, Mg_2Ni and $LaNi_5$. *Journal of Alloys and Compounds*. **231**(1-2): 804-809. DOI: 10.1016/0925-8388(95)01721-6.

53. Asakuma Y, Miyauchi S, Yamamoto T, Aoki H, Miura T. 2003. Numerical analysis of absorbing and desorbing mechanism for the metal hydride by homogenization method. *International Journal of Hydrogen Energy*. **28**(5): 529-536. DOI: 0.1016/S0360-3199(02)00136-2.

54. Mitchell PCH, Ramirez-Cuesta AJ, Parker SF, Tomkinson J, Thompsett D. 2003. Hydrogen Spillover on Carbon-Supported Metal Catalysts Studied by Inelastic Neutron Scattering. Surface Vibrational States and Hydrogen Riding Modes. *Journal of Physical Chemistry B*. **107**(28): 6838-6845. DOI: 10.1021/jp0277356.

55. Kirchheim R, Muetschele T, Kieninger W, Gleiter H, Birringer R, Koble TD. 1988. Hydrogen in amorphous and nanocrystalline metals. *Materials Science and Engineering*. **99**: 457-462. DOI: 10.1016/0025-5416(88)90377-1.

56. Stuhr U Wipf H, Udovic TJ, Weissmueller J, Gleiter H. 1995. Vibrational excitations and the position of hydrogen in nanocrystalline palladium. *Journal of Physics Condensed Matter*. **7**(2): 219-230. DOI: 10.1088/0953-8984/7/2/002.

57. Yang TH, Pyun SI. 1995. Hydrogen absorption and diffusion into and in palladium: ac-impedance analysis under impermeable boundary conditions. *Electrochimica Acta*. **41**(6): 843-848. DOI: 10.1016/0013-4686(95)00371-1.

58. Yang TH, Pyun SI, Yoon YG. 1997. Hydrogen transport through Pd electrode: current transient analysis. *Electrochimica Acta*. **42**(11): 1701-1708. DOI: 10.1016/S0013-4686(96)00369-6.

59. Fine ME. 1964. *Introduction to phase transformations in condensed systems*. The Macmillan company: New York; 33-42.

60. Cui N, Luo JL, Chuang KT. 2001. Study of hydrogen diffusion in α- and β-phase hydrides of Mg_2Ni alloy by microelectrode technique. *Journal of Electroanalytical Chemistry*. **503**(1-2): 92-98. DOI: 10.1016/S0022-0728(01)00381-3.

61. Cui N, Luan B, Liu HK, Zhao HJ, Dou SX. 1995. Characteristics of magnesium-based hydrogen-storage alloy electrodes. *Journal of Power Sources*. **55**(2): 263-267. DOI: 10.1016/0378-7753(95)02195-M.

62. Ye Z, Erickson LC, Hjorvarsson B. 1994. Hydride formation in Mg-ZrFe1.4Cr0.6 composite material. *Journal of Alloys and Compounds*. **209**(1-2): 117-124. DOI: 10.1016/0925-8388(94)91085-5.

63. Miyamoto M, Yajima K, Nakata Y. 1983. Reaction kinetics of $LaNi_5$. *Journal of the Less-Common Metals*. **89**(1): 111-116. DOI: 10.1016/0022-5088(83)90254-0.

64. Nahm KS, Kim WY, Hong SP, Lee WY. 1992. The reaction kinetics of hydrogen storage in LaNi$_5$. *International Journal of Hydrogen Energy*. **17**(5): 333-338. DOI: 10.1016/0360-3199(92)90169-W.

65. Belkbir L, Joly E, Gerard N, Achard JC, Percheron-Guegan A. 1980. Evolution of the kinetic properties in a family of substituted LaNi//5 hydrides during activating formation-decomposition cycling. *Journal of the Less-Common Metals*. **73**(1): 69-77. DOI: 10.1016/0022-5088(80)90344-6.

66. Wang XL, Suda S. 1990. Study of the hydriding kinetics of LaNi$_{4.7}$Al$_{0.3}$-H system by a step-wise method. *Journal of the Less-Common Metals*. **159**:109-119. DOI: 10.1016/0022-5088(90)90138-A.

67. Gao RG, Tu JP, Wang XL, Zhang XB, Chen CP. 2003. The absorption and desorption properties of nanocrystalline Mg$_2$Ni$_{0.75}$Cr$_{0.25}$ alloy containing TiO$_2$ nanoparticles. *Journal of Alloys and Compounds*. **356-357**: 649-653. DOI: 10.1016/S0925-8388(02)01287-2.

68. Bogdanovic B, Sandrock G. 2002. Catalyzed complex metal hydrides. *MRS Bulletin*. **27**(9): 712-716.

69. Huang ZG, Guo ZP, Calka A, Wexler D, Liu HK. 2006. Effects of carbon black, graphite and carbon nanotube additives on hydrogen storage properties of magnesium. *Journal of Alloys and Compounds*. In press. DOI: 10.1016/j.jallcom.2006.03.069.

70. Yang J, Ciureanu M, Roberge R. 2000. Hydrogen storage properties of nano-composites of Mg and Zr–Ni–Cr alloys. *Materials Letters*. **43**(5-6): 234-239. DOI: 10.1016/S0167-577X(99)00265-7.

71. Bobet JL, Grigorovab E, Khrussanovab M, Khristovb M, Radevb D, Peshevb P. 2002. Hydrogen sorption properties of the nanocomposites Mg–Mg$_2$Ni$_{1-x}$Fe$_x$. **345**(1-2): 280-285. DOI: 10.1016/S0925-8388(02)00435-8.

72. Meregalli V, Parrinello M. 2001. Review of theoretical calculations of hydrogen storage in carbon-based materials. *Applied Physics A*. **72**(2): 143-146. DOI: 10.1007/s003390100789.

73. Wong-Foy AG, Matzger AJ, Yaghi OM. 2006. Exceptional H$_2$ saturation uptake in microporous metal-organic frameworks. *Journal of the American Chemical Society*. **128**(11): 3494-3495. DOI: 10.1021/ja058213h.

74. Sachs C, Pundt A, Kirchheim R, Winter M, Reetz MT, Fritsch D. 2001. Solubility of hydrogen in single-sized palladium clusters. *Physical Review B*, **64**: 075408. DOI: 10.1103/PhysRevB.64.075408.

75. Cox DM, Fayet P, Brickman R, Hahn MY, Kaldor A. 1990. Abnormally large deuterium uptake on small transition metal clusters. *Catalysis Letters*. **4**(4-6): 271-278. DOI: 10.1007/BF00765311.

76. Kuji T, Uchidab H, Satob M, Cuib W. 1999. Thermodynamic properties of hydrogen in fine Pd powders. *Journal of Alloys and Compounds*. **293-295**: 19-22. DOI: 10.1016/S0925-8388(99)00387-4.

77. Jurczyka M, Okonskaa I, Iwasieczkob W, Jankowskac E, Drulisb H. 2006. Thermodynamic and electrochemical properties of nanocrystalline Mg$_2$Cu-type hydrogen storage materials. *Journal of Alloys and Compounds*. In press. DOI: 10.1016/j.jallcom.2006.04.024.

78. Johnston RL. 2002. *Atomic and molecular clusters*. Taylor & Francis: London; New York; 8, 87, 120-121.

79. Chou KC, Lia Q, Lina Q, Jiangc LJ, Xub KD. 2005. Kinetics of absorption and desorption of hydrogen in alloy powder. *International Journal of Hydrogen Energy.* **30**(3): 310-309. DOI: 10.1016/j.ijhydene.2004.04.006.

80. Martin M, Gommel C, Borkhart C, Fromm E. 1996. Absorption and desorption kinetics of hydrogen storage alloys. *Journal of Alloys and Compounds.* **238**(1-2): 193–201. DOI: 10.1016/0925-8388(96)02217-7.

81. Zhang J, Fisher TS, Ramachandran PV, Gore JP, Mudawar I. 2005. A review of heat transfer issues in hydrogen storage technologies. *Journal of Heat Transfer.* **127**(12): 1391-1399. DOI: 10.1115/1.2098875.

82. Sánchez AR, Klein HP, Groll M. 2003, Expanded graphite as heat transfer matrix in metal hydride beds, *International Journal of Hydrogen Energy.* **28**(5): 515-527. DOI: 10.1016/S0360-3199(02)00057-5.

83. Kim KJ, Montoya B, Razani A, Lee KH. 2001. Metal hydride compacts of improved thermal conductivity, *International Journal of Hydrogen Energy.* **26**(6): 609-613. DOI: 10.1016/S0360-3199(00)00115-4.

84. Chen G, Borca-Tasciuc D, Yang RG. 2004. Nanoscale heat transfer. In *Encyclopedia of Nanoscience and Nanotechnology,* Nalwa HS (ed.); American Scientific Publishers **7**, 429-459.

85. Gadre SA, Ebner AD, Al-Muhtaseb SA, Ritter JA. 2003. Practical modeling of metal hydride hydrogen storage systems. *Industrial and Engineering Chemistry Research.* **24**(8): 1713-1722. DOI: 10.1021/ie020839i.

86. Klein HP, Groll M. 2004. Heat transfer characteristics of expanded graphite matrices in metal hydride beds. *International Journal of Hydrogen Energy.* **29**(14): 609-613. DOI: 10.1016/j.ijhydene.2004.01.017.

87. Kuji T, Matsumurab Y, Uchidab H, Aizawac T. 2002. Hydrogen absorption of nanocrystalline palladium. *Journal of Alloys and Compounds.* **330-332**: 718-722. DOI: 10.1016/S0925-8388(01)01597-3.

88. Israelachvili J. 1991. *Intermolecular and surface forces.* London: Academic Press.

89. Chen G. 2005. *Nanoscale energy transport and conversion.* Oxford: New York; 438-443.

90. Zhao X, Johnson JK, Rasmussen CE. 2004. Surface tension of quantum fluids from molecular simulations. *Journal of Chemical Physics.* **120**(18): 8707-8715. DOI: 10.1063/1.1695317.

91. Nieh TG, Wadsworth J. 1991. Scripta. Metall. Mater. **25**:955.

92. http://en.wikipedia.org/wiki/Magnesium. Last accessed on 06/05/2008.

93. Bérubé V, Radtke G, Dresselhaus MS, Chen C. 2007. Size effects on the hydrogen storage properties of nanostructured metal hydrides: A review. *Int J Energy Research* .**31**(6-7):637-663.

94. Huot J, Liang G, Boily S, Van Neste A, Schulz R. 1999. Structural study and hydrogen sorption kinetics of ball-milled magnesium hydride. *J Alloys Compounds.*293-295:495-500.

95. Sakintuna B, Lamari-Darkrim F, Hirscher M. 2007. Metal hydride materials for solid hydrogen storage: A review. *Int J Hydrogen Energy.* **32**(9):1121-1140.

96. Mayer U, Groll M, Supper W. 1987. Heat and mass transfer in metal hydride reaction beds: Experimental and theoretical results. *J Less Common Metals.* **131**(1-2):235-244.

97. Askri F, Jemni A, Ben Nasrallah S. 2003. Study of two-dimensional and dynamic heat and mass transfer in a metal-hydrogen reactor. *Int J Hydrogen Energy.* **28**(5):537-557.

98. Marty P, Fourmigue JF, Rango PD, Fruchart D, Charbonnier J. 2006. Numerical simulation of heat and mass transfer during the absorption of hydrogen in a magnesium hydride. *Energy Conversion Management.* **47**(20):3632-3645.

99. Aldas K, Mat MD, Kaplan Y. 2002. A three-dimensional mathematical model for absorption in a metal hydride bed. *Int J Hydrogen Energy.* **27**(10):1049-1056.

100. Demircan A, Demiralp M, Kaplan Y, Mat MD, Veziroglu TN. 2005. Experimental and theoretical analysis of hydrogen absorption in LaNi5-H2 reactors. *Int J Hydrogen Energy.* **30**(13-14):1437-1446.

101. Gopal MR, Murthy SS. 1995. Studies on heat and mass transfer in metal hydride beds. *Int J Hydrogen Energy.* **20**(11):911-917.

102. Kaplan Y, Ilbas M, Mat MD, Demiralp M, Veziroglu TN. 2006. Investigation of thermal aspects of hydrogen storage in a LaNi5-H2 reactor. *Int J Energy Research.* **30**(6):447-458.

103. Martin M, Gommel C, Borkhart C, Fromm E. 1996. Absorption and desorption kinetics of hydrogen storage alloys. *J Alloys Compounds.* **238**(1-2):193-201.

104. Friedlmeier G, Groll M. 1997. Experimental analysis and modeling of the hydriding kinetics of Ni-doped and pure Mg. *J Alloys Compounds.* **253**-254:550-555.

105. Barkhordarian G, Klassen T, Bormann R. 2006. Kinetic investigation of the effect of milling time on the hydrogen sorption reaction of magnesium catalyzed with different Nb2O5 contents. *J Alloys Compounds.* **407**(1-2):249-255.

106. Mintz MH, Zeiri Y. Hydriding kinetics of powders. 1995. *J Alloys Compounds.* **216**(2):159-175.

107. Nasrallah SB, Jemni A. 1997. Heat and mass transfer models in metal-hydrogen reactor. *Int J Hydrogen Energy.* **22**(1):67-76.

108. Vigeholm B, Kjoller J, Larsen B, Pedersen AS. 1983. Formation and decomposition of magnesium hydride. *J Less Common Metals.* **89**(1):135-144.

109. Frederking THK, Hepler WA, Khandhar PK. 1988. Slip effects associated with Knudsen transport phenomena in porous media. *Cryogenics.* **28**(2):110-114.

110. Yagi S, Kunii D. 1957. Studies on effective thermal conductivities in packed beds. *AIChE Journal.* **3**(3):373-381.

111. Ishido Y, Kawamura M, Ono S. 1982. Thermal conductivity of magnesium-nickel hydride powder beds in a hydrogen atmosphere. *Int J Hydrogen Energy.* **7**(2):173-182.

112. Lasave J, Dominguez F, Koval S, Stachiotti MG, Migoni RL. 2005. Shell-model description of lattice dynamical properties of MgH2. *J Physics: Condensed Matter.* **17**(44):7133-7141.

113. Wolf U, Bohmhammel K, Wolf G. 1998. A simple adiabatic low-temperature calorimeter based on a helium refrigerator system. *Thermochimica Acta.* **310**(1-2):37-42.

114. Varin RA, Czujko T, Chiu CH and Wronski Z. 2006. Particle size effects on the desorption properties of nanostructured magnesium dihydride (MgH2) synthesized by controlled reactive mechanical milling. *Journal of Alloys and Compounds.* **424**(1-2):356-364.

115. Zeng K, Klassen Y, Oelerich W, Bormann R. 1999. Critical assessment and thermodynamic modeling of the Mg–H system. *International Journal of Hydrogen Energy.* **24**(10):989-1004.

116. Du AJ, Smith SC, Yao XD, Lu GQ. 2006. Ab initio studies of hydrogen desorption from low index magnesium hydride surface. *Surface Science.* **600**:1854-1859.

117.   Vajeeston P, Ravindran P, Kjekshus A and Fjellvag H. 2002. Pressure-Induced Structural Transitions in MgH₂. *Phys Rev Lett.* **89**:175506(1-4).

118.   Bastide J-P, Bonnetot B, Létoffé J-M, Claudy P. 1980. Polymorphisme de l'hydrude de magnésium sous haute pression.   *Materials Research Bulletin.* **15**(12):1779-1787.

119.   Gennari FC, Castro FJ, Urretavizcaya G. 2001. Hydrogen desorption behavior from magnesium hydrides synthesized by reactive mechanical alloying. *Journal of Alloys and Compounds.* **321**(1):46-53.

120.   Humphreys FJ, Hatherly M. 2004. Recrystallization and related annealing phenomena. *Elsevier.*

121.   Bérubé V, Chen G, Dresselhaus MS. 2008. Impact of nanostructuring on the enthalpy of formation of metal hydrides. *International Journal of Hydrogen Energy.* In press.

122.   Zharkov VN, Kalinin VA. 1971. Equations of state for solids at high pressures and temperatures. NewYork-London: *Consultants bureau.*

123.   Murnaghan FD. 1944. The Compressibility of Media under Extreme Pressures. *Proceedings of the National Academy of Sciences.* **30**:244-247.

124.   Birch F. 1938. The effect of pressure upon the elastic parameters of isotropic solids, according to Murnaghan's theory of finite strain. *Journal of applied physics.* **9**(4):279-288.

125.   Polanski M, Bystrzycki J, Plocinski T. 2008. The effect of milling conditions on microstructure and hydrogen absorption/desorption properties of magnesium hydride (MgH₂) without and with Cr₂O₃ nanoparticles. *International Journal of Hydrogen Energy.* In Press, Available online 17 March 2008.

126.   Singh BK, Shim G, Cho S-W. 2007. Effects of mechanical milling on hydrogen storage properties of Ti₀.₃₂Cr₀.₄₃V₀.₂₅ alloy. *International Journal of Hydrogen Energy.* **32**(18):4961-4965.

127.   Fátay D, Spassov T, Delchev P, Ribárik G, Révész Á. 2007. Microstructural development in nanocrystalline MgH₂ during H-absorption/desorption cycling. *International Journal of Hydrogen Energy.* **32**(14):2914-2919.

128.   Drozd V, Saxena S, Garimella SV, Durygin A. 2007. Hydrogen release from a mixture of NaBH₄ and Mg(OH)₂. *International Journal of Hydrogen Energy.* **32**(15): 3370-3375.

129.   Andrews FC. 1971. Thermodynamics: principles and applications. New York: *John Wiley & Sons, Inc.*

130.   Vinet P, Smith JR, Ferrante J, Rose JH. 1987. Temperature effects on the universal equation of states. *Physical Review B.* **35**(4):1945-1953.

131.   Anderson MS, Swenson CA. 1985. Experimental equations of state for cesium and lithium metals to 20 kbar and the high-pressure behavior of the alkali metals. *Physical Review B.* **31**:668-680.

132.   Anderson MS, Swenson CA. 1975. Experimental equations of state for the rare gas solids. *J. Phys. Chem. Solids.* **36**:145-162.

133.   Ashcroft NW, Mermin ND. 1976. Solid state physics. *Saunders.*

134.   http://www.engineeringtoolbox.com/hydrogen-d_976.html.   Last   accessed 06/23/2008.

135.	Bérubé V, Chen G, Dresselhaus MS. 2008. Temperature dependence of the enthalpy of formation of metal hydrides characterized by an excess volume. *International Journal of Hydrogen Energy*. In press.

136.	Christian JW. 1965. The theory of transformation in metals and alloys. Oxford: *Pergamon Press*.

137.	Gscheidner KA Jr. 1957. Solid state physics, edited by Seitz F and Turnbull D. New York: *Academic*.

138.	Barron THK, Collins JG and White GK. 1980. Thermal expansion of solids at low temperatures. *Adv. Phys.* **29**(4):609-730.

139.	Korn D, Morsch A, Birringer R, Arnold W and Gleiter H. 1988. Interface science & engineering. Edited by Raj RR and Sass SL. *J. Phys. (Paris);Colloq.* **49**:C5-769.

140.	Yu R and Lam PK. 1988. Electronic and structural properties of MgH_2. *Phys. Rev. B.* 37(15):8730-8738.

141.	Mehta S, Price GD and Alfè D. 2006. Ab initio thermodynamics and phase diagram of solid magnesium: A comparison of the LDA and GGA. *J. Chem. Phys.* **125**: 194507.

142.	Frost HJ and Ashby MF, Editors. 1982. Deformation-mechanism maps, the plasticity and creep of metals and ceramics. New York: *Pergamon Press*. 43-45.

143.	Lasave J, Dominguez F, Koval1 S, Stachiotti MG and Migoni RL. 2005. Shell-model description of lattice dynamical properties of MgH_2. *J. Phys. Condens. Matter.* **17**:7133-7141.

144.	http://en.wikipedia.org/wiki/Raman_spectroscopy. Last accessed 09/07/2008.

145.	Lu G, An H, Chen Y, Huang J, Zhang H, Xiang B, Zhao Q, Yu D and Du W. 2005. Temperature dependence of Raman scattering of ZnSe nanoparticle grown through vapor phase. *J. of Crystal Growth*. 274(3-4):530-535.

146.	Santisteban JR, Cuello GJ, Dawidowski J, Fainstein A, Peretti HA, Ivanov A and Bermejo FJ. 2000. Vibrational spectrum of magnesium hydride. *Phys. Rev. B.* 62(1):37-40.

147.	"National	Hydrogen	Energy	Roadmap" http://www1.eere.energy.gov/hydrogenandfuelcells/pdfs/national_h2_roadmap.pdf. (visited on 11/20/07).